Fluorophilicity in Biologically Relevant Systems Studied with Fluorinated Rhodamines

Dissertation

zur Erlangung des Doktorgrades der Naturwissenschaften
(Dr.-rer.nat.)

der

Naturwissenschaftlichen Fakultät II
Chemie, Physik und Mathematik

der Martin-Luther-Universität
Halle-Wittenberg

vorgelegt von

Herrn M.Sc. Mark Jbeily
geboren am 24.08.1986 in Freetown, Sierra Leone

Gutachter:
1. Prof. Dr. J. Kreßler
2. Prof. Dr. A. Laschewsky

Tag der Verteidigung: 21.04.2017

"I've been through a lot and I realize the future can't be controlled. I'm not worried. You can always learn to overcome difficulties."

Andreas Nikolaus "Niki" Lauda

Table of contents

List of abbreviations

2D	two dimensional
3D	three dimensional
5:3 acid	C_5F_{11}-C_2H_4-COOH
CLSM	confocal laser scanning microscopy
CMC	critical micelle concentration
DMPS	1,2-dimyristoyl-*sn*-glycero-3-phospho-L-serine
DOPC	1,2-dioleoyl-*sn*-glycero-3-phosphocholine
DPPC	1,2-dipalmitoyl-*sn*-glycero-3-phosphocholine
DSC	differential scanning calorimetry
Erα	estrogen receptor α
ESI-ToF	electrospray ionization-time of flight
ESR	electron spin resonance
F-oct	perfluoro-*n*-octane
F-SPE	fluorous solid phase extraction
F6H2OH	1H,1H,2H,2H-perfluoro-1-octanol
F8H2OH	1H,1H,2H,2H-perfluoro-1-decanol
FC18	perfluorostearic acid
FCS	fluorescence correlation spectroscopy
FRET	Förster resonance energy transfer
GUV	giant unilamellar vesicle
HOMO	highest occupied molecular orbital
L_α	liquid-crystalline phase
$L_{\beta'}$	tilted gel phase
LC	liquid condensed
LE	liquid expanded
LUMO	lowest unoccupied molecular orbital
LUV	large unilamellar vesicle
MAS	magic angle spinning
MLV	multilamellar vesicle
NBD	7-nitro-2-1,3-benzoxadiazol-4-yl

NMR	nuclear magnetic resonance
NOAEL	no observed adverse effect level
O	1-octanol
oct	*n*-octane
PFBS	perfluorobutanesulfonic acid
PFHpA	perfluoroheptanoic acid
PFHx	perfluorohexanoate
PFHxA	perfluorohexanoic acid
PFMC	perfluoromethylcyclohexane
PFOA	perfluorooctanoic acid
PFOS	perfluorooctanesulfonic acid
PFPeA	perfluoropentanoic acid
PFSA	perfluorostearic acid
Rh	rhodamine
SA	stearic acid
SUV	small unilamellar vesicle
TFE	2,2,2-trifluoroethanol
Tol	toluene
W	water

1 Introduction

1.1 Phospholipids and fluorotelomers

1.1.1 Phospholipids and their most common physical characterization methods

The majority of lipids in eukaryotic cell membranes are phospholipids, which account for almost 50 % of the plasma membrane's mass [1]. They are amphiphilic, having a polar (hydrophilic) and a non-polar (hydrophobic) part [1]. In eukaryotic cell membranes, the most abundant structural lipids are the glycerophospholipids having different polar headgroups such as phosphatidylcholine, phosphatidylethanolamine, phosphatidylserine, phosphatidylinositol, and phosphatidic acid. A diacylglycerol moiety forms their hydrophobic portion containing saturated or *cis*-unsaturated fatty acyl chains of different lengths [2]. The phosphatidylcholine headgroup accounts for more than 50 % of the phospholipids in eukaryotic cells, most of them having one *cis*-unsaturated fatty acyl chain which renders them fluid at room temperature [2]. Two examples of zwitterionic phospholipids: 1,2-dioleoyl-*sn*-glycero-3-phosphocholine (DOPC) and 1,2-dipalmitoyl-*sn*-glycero-3-phosphocholine (DPPC) structures are shown in Fig. 1.1 where *sn* stands for stereospecific numbering of the glycerol carbon atoms [3]. They will be used later in bilayer experiments as simplified model cell membranes. Anionic and cationic phospholipids, i.e. phospholipids having anionic or cationic headgroups also exist but will not be discussed here. Fig. 1.2 illustrates the phase diagram of DPPC bilayers.
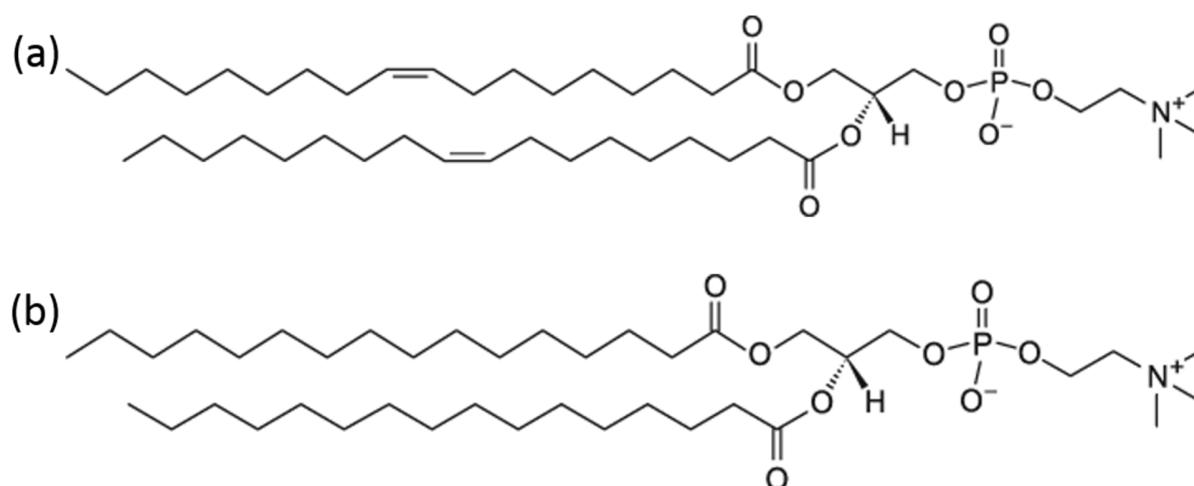
Fig. 1.1. (a) 1,2-dioleoyl-*sn*-glycero-3-phosphocholine (DOPC). (b) 1,2-dipalmitoyl-*sn*-glycero-3-phosphocholine (DPPC).
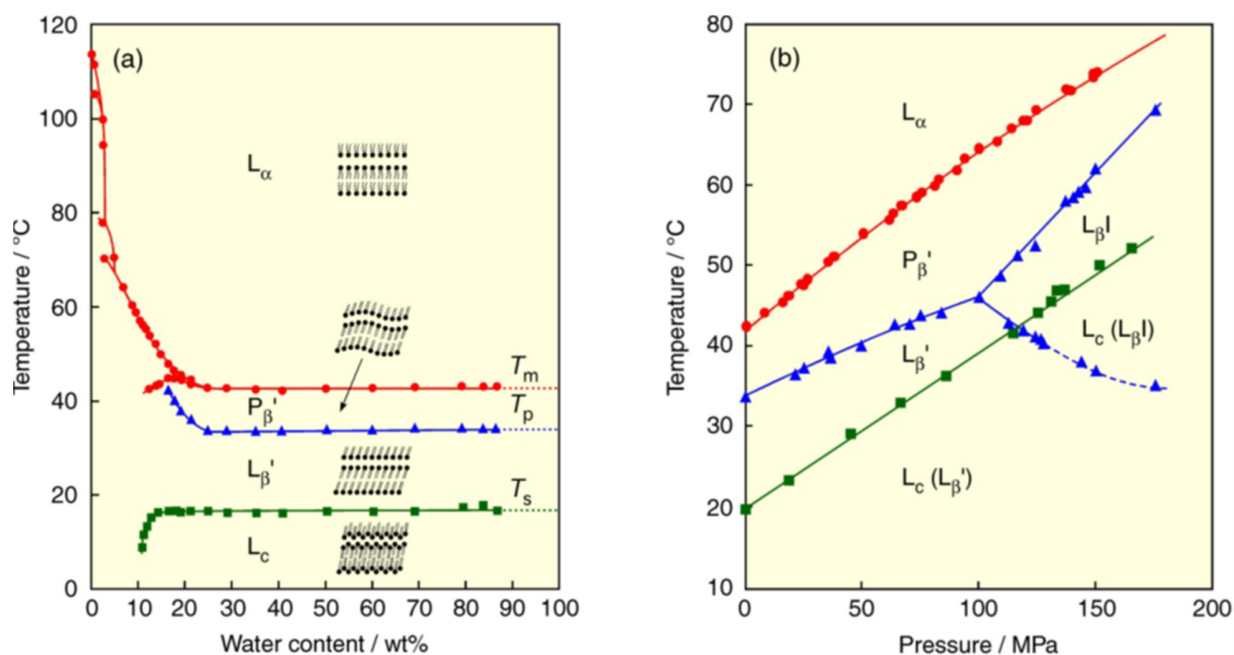
Fig. 1.2. (a) Effect of water content on phase-transition temperatures of DPPC bilayers. (b) Temperature-pressure phase diagrams of DPPC bilayer. Phase transitions: (green) subtransition, (blue) pretransition and transitions between gel phases, (red) main transition. Dashed line indicates the transition between metastable gel phases [4].

More information regarding the physical properties of phospholipids including their headgroups, fatty acyl chain composition, pK_a values, crystal structures, phase diagrams, calorimetric data, transition temperatures, critical micelle concentrations, etc. can be found in the Phospholipids Handbook [5]. However biological membranes are not made only from phospholipids, cholesterol and membrane proteins are also essential components of biological cell membranes. However, the discussion will be limited to phospholipids and for the reader seeking more information, an excellent updated review from Nicolson on the fluid-mosaic model of membranes as a starting point is highly recommended [6]. The modified Fluid-Mosaic Membrane is shown in Fig. 1.3.
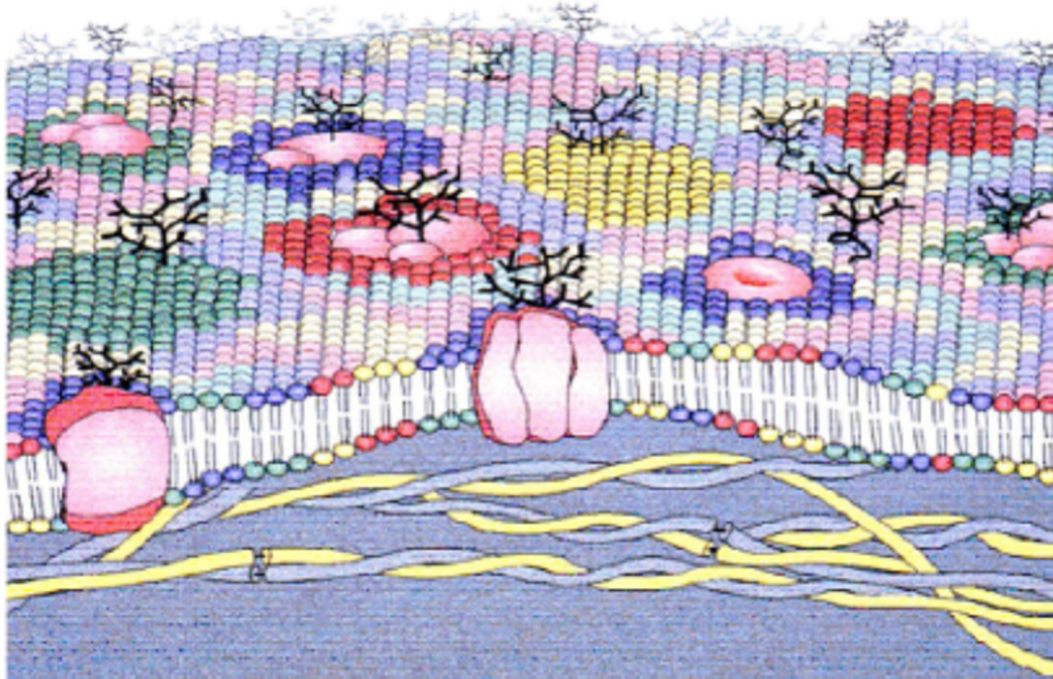
Fig. 1.3. A modification to the Fluid-Mosaic Membrane, by Escribá et al. showing lipid membrane asymmetry, lipid rafts, and membrane proteins [7].

Phospholipids are even more ubiquitous in nature since they are also present in the membranes of microorganisms, algae, plants, protozoa, insects, gastropods, amphibians, and various marine organisms such as jellyfish, crabs, and fish [5]. Their abundance in the living world makes them a subject of interest for research. The physical characterization of phospholipids is achieved by several techniques; mainly diffraction, spectroscopic, and calorimetric techniques [5]. X-ray diffraction is the principle technique for phospholipid single crystal studies and their hydrated structures. Neutron diffraction has some advantages due to the ability of contrast variation, hydrogen atoms position detection, and dynamic studies by quasi-elastic or inelastic neutron scattering [8]. X-rays are a part of the electromagnetic spectrum having wavelengths in the range of a few Å. They are mainly scattered by the electrons in a sample, thus the scattering power of a given atom increases with the number of electrons, i.e. the atomic number Z. Light scattering and optical diffraction is a useful experimental tool but not for single phospholipid molecules due to the long wavelengths of visible light (400-700 nm). But it is advantageous in the investigation of phospholipid aggregates such as micelles or vesicles in suspension. Elastic (pseudo-Rayleigh) light scattering is often used in light scattering experiments due to the relatively small phospholipid

aggregates size. It is important to mention that the scattered light intensity is proportional to the sixth power of the vesicle radius which makes working under dust free conditions a necessity [5]. Electron spin resonance (ESR) and nuclear magnetic resonance (NMR) spectroscopy are important characterization techniques of phospholipids. ESR spectroscopy is extensively used to study phospholipid-ion interactions such as Cu^{2+} and Fe^{3+} since they are paramagnetic and can be observed directly without the addition of spin probes. But normal phospholipid molecules must be spin labeled with some commercially available stable radicals. The main advantages of ESR spectroscopy are the relatively short time scale, high sensitivity, and the use of highly concentrated or opaque samples is not problematic. ESR spectroscopy's main disadvantage is the bulky spin label which is problematic for highly ordered systems which make studying the systems at different dilutions a routine [9].

NMR spectroscopy investigates the recovery of macroscopic magnetization to equilibrium after a radio-frequency pulse in a static, homogeneous magnetic field by two characteristic relaxation times T_1 and T_2 which are dependent on the spin-lattice and spin-spin interactions, respectively, from which the corresponding correlation times of those interactions can be gained [5]. The hydrated lipid bilayer is anisotropic, therefore its orientation-dependent interactions, including dipolar interactions and chemical shift anisotropy are not averaged leading to broad lines in solid-state NMR spectroscopy. Solid state NMR spectroscopy takes advantage of ^{31}P NMR spectroscopy in phospholipid containing systems since there is one ^{31}P per phospholipid molecule. Fast isotropic reorientations of the ^{31}P nuclei lead to narrow peaks, whereas anisotropic reorientations yield characteristic broad lines. ^{31}P NMR spectroscopy proved useful to study phospholipids phase transitions since the chemical shift of the ^{31}P changes significantly at the main transition. ^{13}C NMR spectroscopy is used similarly to ^{31}P NMR spectroscopy, and by magic angle spinning (MAS), high-resolution lipid spectra can be obtained. ^{2}H NMR spectroscopy can be used to calculate order parameters to describe dynamics and conformations of lipid molecules, but this technique requires the use of deuterated lipids [10,11]. Nowadays, the need for ^{2}H labeled lipids decreased substantially due to the introduction of ^{1}H NMR MAS and ^{1}H-^{13}C 2D NMR spectroscopic techniques enabling NMR spectroscopy with non-deuterated lipids [12-15].

Light spectroscopy includes UV-Vis (absorption) and fluorescence (emission) spectroscopy. UV-Vis is frequently used to quantify the extent of oxidation of phospholipids having unsaturated acyl chains using the Lambert-Beer law [16,17]. Fluorescence spectroscopy is more often used and based on the excitation of an electron from the S_0 (ground state) usually to S_1 (first excited state)

or some higher excitation states upon the absorption of light (femtosecond, 10^{-15} s time scale). The relaxation from the ground vibrational energy level of the S_1 excited state to the S_0 ground state occurs on the nanosecond (10^{-9} s) time scale with a photon emission (fluorescence). Almost all lipids need to be labeled with fluorescence dyes to make fluorescence measurements with visible light feasible. Several fluorescent lipids are nowadays commercially available which cover almost the whole visible spectrum with relatively high quantum yields (ratio of emitted to absorbed photons) [18,19]. They are either headgroup-labeled by a fluorescence dye (usually hydrophilic) or acyl chain labeled mainly with NBD or pyrene fluorescence moieties. An important factor in choosing a certain lipid fluorescence dye is the position of the absorption and emission maxima. Fluorescence quenching is a basic and very useful tool in lipid characterization since the quantum yield is not sensitive to the excitation wavelength but highly sensitive to quenchers, for instance, other light-absorbing molecules. Fluorescence quenching is readily used for the quantification of vesicle encapsulation and leakage rates which is usually achieved with fluorescent dyes exhibiting self-quenching in the mM concentration range. Using a fluorescence quencher (acceptor) having an absorption band that overlaps with the emission band of the blue-shifted fluorescent dye (donor), Förster resonance energy transfer (FRET) [20,21] might occur if the spatial separation between the donor and acceptor molecules is on the order of a few nanometers. The fluorescence intensity decreases with the inverse sixth power of the distance between donor and acceptor which provides an efficient tool for measuring their separation distance. Fluidity and order of lipid membranes can be investigated by static or time-resolved fluorescence anisotropy measurements [22]. Lateral diffusion of lipids can be studied with fluorescence recovery after photobleaching (FRAP) and fluorescence correlation spectroscopy (FCS) techniques which are mainly used to study and calculate diffusion coefficients of lipids and proteins in membranes [23,24]. Solvatochromism is observed with many fluorophores upon changes in the local surrounding environment [25,26]. Usually, polar environments cause a red shift, and nonpolar ones cause a blue shift in the emission spectra of the corresponding fluorescence dyes, but exceptions to this rule are also common. This fact has enabled scientists to assay local environments successfully near lipid headgroups and in the lipid bilayer. Changes in polarity induced by temperature variations can also be investigated with solvatochromism. Fluorescence polarization measurements are readily done to get valuable information about the mobility and order of the fluorophore. Fluorophores attached covalently to the acyl chains of the lipids are embedded in the hydrophobic double layer of the membrane and are excellent probes for dynamic studies and average orientation of the aliphatic chains in this

highly anisotropic system. Thus the fluorescence anisotropy is a measure of the order parameter. The basics of fluorescence will be discussed later in section 1.3. Infrared (vibrational) spectroscopy is also used to study the orientation of acyl chains with several IR techniques such as attenuated total reflection infrared (ATR-IR) spectroscopy to investigate phase transitions and organization in phospholipids [27-29]. Raman spectroscopy also finds several applications in phospholipid characterization methods mainly to monitor conformational organization in the bilayer [30]. One of the main advantages of Raman spectroscopy over IR is that water does not scatter light strongly making it useful for studying lipids or other biologically relevant molecules in aqueous environments [31]. Phospholipid phase transitions between L_α and $L_{\beta'}$ can be monitored with Raman spectroscopy and show increasing order upon cooling which occurs over a temperature range of approximately 10 °C unlike the sharp phase transition seen in calorimetry [31]. Lange et al. used Raman spectroscopy to directly measure the phase coexistence in DPPC/cholesterol mixed vesicles and showed that phase coexistence regions extended from 0 to 25 mol % cholesterol and that the partitioning of cholesterol between cholesterol rich and poor phases follows the lever rule [32]. Lately, Czamara et al. published a review on Raman spectroscopy of lipids where they investigated fatty acids, triacylglycerols, cholesteryl esters, and phospholipids having choline or ethanolamine moieties. They were able to calculate degree of unsaturation of lipids from the ratio of carbon-carbon double-bonds to the CH_2 vibrational bands at 1655 and 1444 cm^{-1}, respectively [33]. Calorimetric techniques, mainly differential scanning calorimetry (DSC) offers a sensitive and robust tool to investigate the phase behavior of phospholipids in model and biological membranes with the absence of extra probes [34]. Gel to liquid-crystalline phase transitions in lipid bilayers and biological membranes are routinely measured by DSC. DSC is a relatively inexpensive method and with commercially available high-sensitivity devices dilute suspensions can be used which leads to a good control of pH value and ionic strength of the aqueous phase. The whole phase transition is observed starting from the onset to the end, and important information can be gained by analyzing it. It does not require exogenous probes such as fluorescence dyes for fluorescence measurements which leads to negligible perturbations to the system under investigation. DSC also provides a direct thermodynamic measurement of lipid phase transitions. One of the disadvantages of DSC is that it does not provide molecular structure and dynamics details, but complementing it with X-ray diffraction or NMR spectroscopy provides an efficient tool to understand phase transitions in lipid membranes at the molecular level. Isothermal titration calorimetry (ITC) is used for the investigation of lipid-peptide interactions [35,36], the

quantification of protein binding to lipid vesicles [37], and critical micelle concentration (CMC) determinations [38]. Temperature modulated DSC (TMDSC) is a powerful addition to DSC that allows the analysis of the frequency dependent heat capacity which allows the study of non-equilibrium thermodynamic processes [39], the separation of several phenomena in semi-crystalline materials such as melting and the change of the heat capacity at the glass transition [40]. With TMDSC, phenomena related to the heat capacity of the sample such as a glass transition are acquired in the reversing heat flow, whereas phenomena involving enthalpic relaxation such as crystallization or decomposition are obtained in the non-reversing heat flow [40]. Currently, TMDSC is a valuable tool to study phase transitions and structural relaxation processes of lipids in multilamellar vesicles as published by Svanberg et al. [41].

1.1.2 Phospholipid vesicles - a brief introduction

Gorter and Grendel [42] followed by Danielli and Davson [43] discovered that phospholipid bilayers are main structural elements of biological membranes. Bear, Palmer, and Schmitt [44,45] later showed for the first time that X-ray diffraction patterns of phospholipid dispersions extracted from myelin sheath are quite similar to the ones of intact nerves. Those pioneering discoveries led to the idea of using phospholipid dispersions as model membranes. Later it was demonstrated by Bangham and his coworkers that phospholipids spontaneously form closed membrane structures in an aqueous environment [46]. Lipid vesicles later became widely used tools in biochemistry, biology, and pharmacy (mainly for drug delivery applications) [47-49]. Phospholipids are amphiphilic molecules formed from hydrophilic and lipophilic parts. Since they are amphiphilic, they are surface active and tend to form aggregates in the dry and fully hydrated states. They show self-assembly into lipid bilayers or vesicles. This is discussed in depth by Israelachvili [50,51]. There are inconsistencies between the swelling of neutral (isoelectric) and negatively charged phospholipids due to the differences in their equilibrium structures present in excess water. Pure phosphatidylcholine (isoelectric) bilayers do not swell indefinitely; rather they show a limit value of approximately $d = 6.5$ nm (lamellar repeating distance) at 40 wt % water. Upon further increase of the water content, two phases are present, fully hydrated phosphatidylcholine and excess water [52,53]. Dimyristoylphosphatidylserine (DMPS) swells continuously with increasing water content both in the crystalline and liquid crystalline state [54]. Continuous swelling is observed up to 70 wt % water. A further increase in the water content is accompanied with the broadening of the X-ray diffraction pattern due to multilayer stacking disorder [52].

LUVs: $\phi = 50\text{-}200$ nm
GUVs: $\phi = 1\text{-}300$ μm
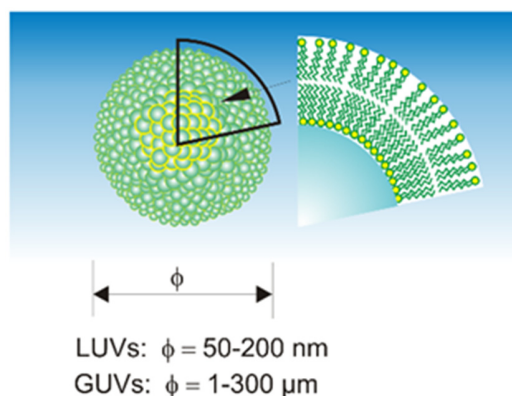
Fig. 1.4. Phospholipid liposomes and GUVs [55].

The presence of electrolytes in the aqueous phase reduces or inhibits the swelling of lipid bilayers. For example, dispersing DMPS in 50 wt % 0.5 M NaCl aqueous solution at room temperature instead of pure water, reduces the lamellar repeating distance d from 13.0 to 6.2 nm [56]. Fully hydrated neutral and isoelectric phospholipids above their crystallization temperatures are predicted to form multilamellar vesicles (MLVs). Whereas acidic phospholipids and lipid mixtures bearing higher surface charge densities (exceeding 2 μC/cm^2) readily form large unilamellar vesicles (LUVs) in excess water [57].

1.1.3 Phospholipid vesicles preparation and characterization

Due to the higher abundance of neutral (isoelectric) phospholipids in comparison to the negatively charged ones, MLVs were firstly prepared and thoroughly studied [58-60]. MLVs preparation is relatively fast and not complicated; phospholipids are deposited on the wall of a round bottom flask from an organic solvent solution which is later evaporated leaving behind a thin film of dried lipid. Adding aqueous solutions followed by swirling (gentle agitation) yields MLVs spontaneously. The MLVs obtained are heterogeneous in size ranging between 0.1 and 10 μm. Exchanging neutral lipids with negatively charged ones while using the same method of gentle hydration yields LUVs with size distribution. However, homogeneous vesicles can be prepared by applying shear forces to the phospholipid dispersions. Sonication [61], extrusion through a needle valve by a hydraulic pump also known as the French press method (high pressures) [62,63], and repeated extrusion through membrane filters of defined pore size (low or medium pressures) [64] are usually the methods of choice to obtain homogeneous lipid vesicles. Other methods use solutions or

dispersions of lipids in organic solvents which include solvent injection and evaporation pioneered by Batzri and Korn [65]. They rapidly injected an ethanol solution of egg lecithin into an aqueous KCl solution. The advantages of the solvent injection method are a low risk of phospholipid degradation and simplicity, but the major disadvantages are low entrapment capacities and poor efficiency due to the presence of ethanol in the solution. Another alternative for the ethanol solution is the injection of lipid dissolved in diethyl ether or chloroform containing minute quantities of methanol into excess water or an aqueous solution kept at 60 °C to achieve a fast evaporation of the organic phase [66,67]. This method yields LUVs with sizes ranging from 0.1 to 0.5 μm. Reverse phase evaporation [67] and double emulsion methods [68] both act on destabilizing water-in-oil microemulsions by solvent evaporation. Heterogeneous LUVs are obtained, but increasing the lipid-to-aqueous solution volume ratio yields MLVs.

Phospholipid vesicles characterization is mainly done by size, shape, and thermodynamic stability. Information about the size of the vesicles is obtained by gel filtration, electron microscopy, dynamic and static light scattering, and ultracentrifugation. Intrinsic viscosity and dynamic light scattering measurements are two good methods to obtain information about the hydrodynamic or Stokes radius R_H of hydrated (solvated) vesicles. MLVs are usually thermodynamically stable given the fact that they form spontaneously upon gentle hydration, but this is not the case for SUVs since they do not form spontaneously upon hydration. The input of external energy is required such as ultrasonication, and this is the main reason for them to be considered thermodynamically unstable. Several observations also show that SUVs are not thermodynamically stable since they tend to aggregate [69,70] and fuse [71-73] with time to yield MLVs.

Giant Unilamellar Vesicles (GUVs) have diameters in the micrometer range which make their examination using light microscopic techniques such as confocal laser scanning microscopy (CLSM) possible. GUVs are usually prepared by electroformation [74-80] and studied with fluorescence microscopy techniques such as CLSM which will be discussed in section 1.5.
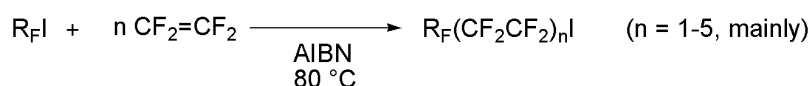
1.1.4 Fluorotelomer alcohols

Fluorotelomer alcohols are fluorinated alcohols bearing a methylene spacer separating the perfluorinated chain from its alcohol moiety (Fig. 1.5) having the general $C_nF_{2n+1}C_mH_{2m}OH$ molecular formula where m is 1 or 2 and n varies between 2 and 10. Even numbers of n (2, 4, 6, 8, and 10) are much more common and commercially available than their odd n integer telomers since

mainly pentafluoroethyl iodide (CF_3CF_2I) is used as the main initiator for the telomerization reaction, which will be discussed further in more detail.
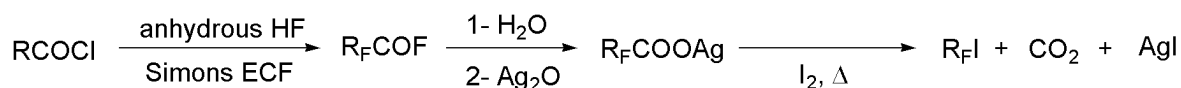
(a)

(b)
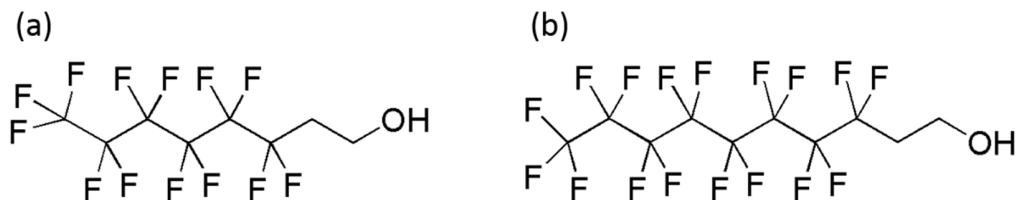
Fig. 1.5. (a) F6H2OH fluorotelomer alcohol; 1H,1H,2H,2H-perfluoro-1-octanol. (b) F8H2OH fluorotelomer alcohol, 1H,1H,2H,2H-perfluoro-1-decanol.

They are named fluorotelomers since they are synthesized by telomerization (Scheme 1.1) which is a radical reaction where the telogen (usually perfluoroethyl iodide) reacts with a certain number of unsaturated molecules named taxogens which are mainly olefins, usually tetrafluoroethylene or ethylene [81].

$$R_FI \ + \ n \ CF_2{=}CF_2 \xrightarrow[\text{80 °C}]{\text{AIBN}} R_F(CF_2CF_2)_nI \quad (n = 1\text{-}5, \text{ mainly})$$
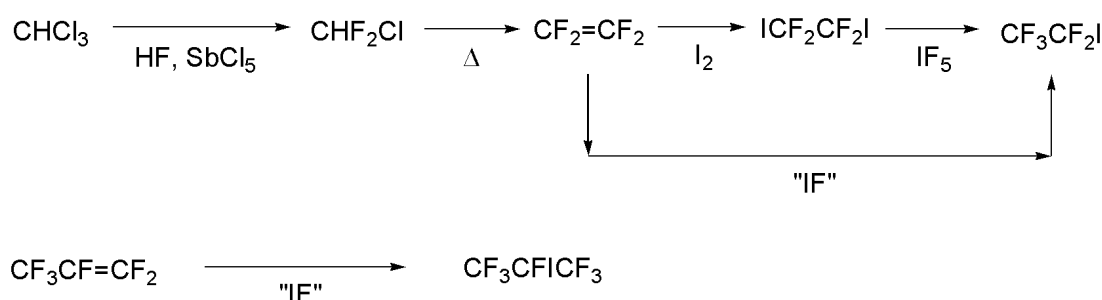
Scheme. 1.1. Perfluoroalkyl iodides synthesis via the industrial telomerization method based on tetrafluoroethylene [82].

Perfluoroalkyl iodides are the main starting materials for the synthesis of fluorotelomer alcohols, and they are synthesized in two main routes. On a laboratory scale, perfluoroalkyl iodides synthesis is mainly achieved by the Simons electrochemical fluorination (ECF) method [83]. Briefly, an activated carboxylic acid, e.g. acyl chloride, is perfluorinated by ECF to yield the perfluorinated product as shown in Scheme 1.2, followed by the reaction of the ECF product with water and silver oxide (Ag_2O) to obtain the silver salt of the corresponding perfluorinated carboxylic acid. In a Hunsdiecker, formerly known as the Borodin reaction [84-86], the silver perfluorocarboxylate is decarboxylated with iodine to give the perfluoroalkyl iodide product with carbon dioxide (CO_2) and silver iodide (AgI) as byproducts.

$$RCOCl \xrightarrow[\text{Simons ECF}]{\text{anhydrous HF}} R_FCOF \xrightarrow[\text{2- Ag}_2O]{\text{1- H}_2O} R_FCOOAg \xrightarrow[\text{I}_2, \, \Delta]{} R_FI \ + \ CO_2 \ + \ AgI$$

Scheme. 1.2. Synthesis of perfluoroalkyl iodides from acyl chlorides via Simons electrochemical fluorination (ECF) followed by the Hunsdieker reaction [82].
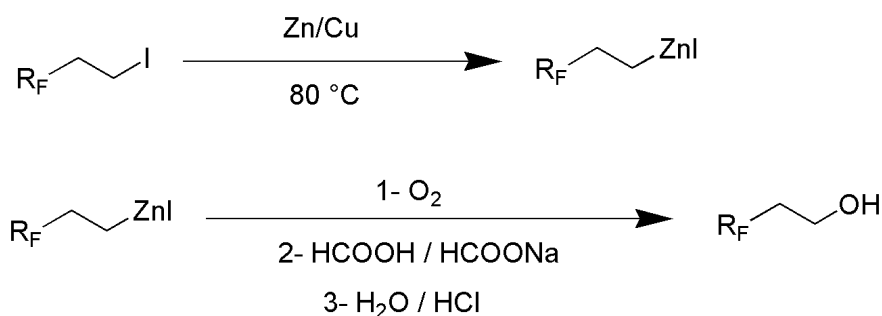
17

The quantitative synthesis of pentafluoroethyl iodide from reacting iodine pentafluoride with 1,2-diiodotetrafluoroethane (synthesized from tetrafluoroethylene) was realized in 1949 by Emeleus and Haszeldine [87]. They also discovered that perfluoroalkyl iodides add in a radical fashion to several olefins yielding telomers at high temperatures [88]. The addition of perfluoroalkyl iodides to olefins proved to be a very important and versatile synthetic method not only for the industrial preparation of fluorotelomers [89] and their corresponding alcohols, but it made the synthesis of partially fluorinated alkanes [90-92] and perfluoroalkyl aromatic compounds [93,94] feasible.

$$CHCl_3 \xrightarrow{HF,\ SbCl_5} CHF_2Cl \xrightarrow{\Delta} CF_2=CF_2 \xrightarrow{I_2} ICF_2CF_2I \xrightarrow{IF_5} CF_3CF_2I$$

$$CF_2=CF_2 \xrightarrow{"IF"} CF_3CF_2I$$

$$CF_3CF=CF_2 \xrightarrow{"IF"} CF_3CFICF_3$$

Scheme. 1.3. Synthesis of pentafluoroiodoethane (*top*) and heptafluoro-2-iodopropane (*bottom*) [82].

On an industrial scale, the telogen is synthesized by reacting tetrafluoroethylene with IF_5 and I_2 to form iodine fluoride (IF) in situ in the presence of Swart's reagent (antimony trifluoride, SbF_3) to yield perfluoroethyl iodide as depicted in Scheme 1.3. Telomerization of tetrafluoroethylene with perfluoroethyl iodide yields a mixture of telomers having an even number of carbon atoms $C_nF_{2n+1}I$. After the desired perfluorinated chain length is achieved, the iodides are reacted in a radical fashion with one equivalent of ethylene to obtain the 1H,1H,2H,2H-perfluoroalkyl iodides. Odd-numbered perfluoroalkyl iodides are possible to prepare by the photochemical initiation of the telomerization reaction with trifluoromethyl iodide [90]. It is obvious that these telomerization reactions are problematic to perform in a laboratory due to the volatility and high vapor pressures of the starting materials and products in addition to difficulties in the purification process [81]. The fluorotelomer alcohol (1H,1H,2H,2H-perfluroalkyl alcohols) can be obtained by reacting the 1H,1H,2H,2H-perfluoroalkyl iodides with metallic zinc-copper in butyl phosphate followed by oxidation in an acidic aqueous environment to obtain the fluorotelomer alcohol as shown in Scheme 1.4 [95]. Another more recent and less common possibility to synthesize fluorotelomer alcohols is the hydroboration of 1H,1H,2H,2H-perfluoro-1-alkenes [96,97]. Substituting the iodine with a

hydroxide, for instance, reacting it with sodium hydroxide (NaOH) to obtain the 1H,1H,2H,2H-perfluroalkyl alcohol is unsuccessful and yields the elimination product. The substitution product is not obtained since the beta-position protons are acidic due to the strong electron withdrawing effect originating from the perfluorinated alkyl chain which favors hydrogen iodide (HI) elimination as illustrated in Scheme 1.5 [98].

$$R_F \diagdown \diagdown I \xrightarrow[\text{80 °C}]{\text{Zn/Cu}} R_F \diagdown \diagdown ZnI$$

$$R_F \diagdown \diagdown ZnI \xrightarrow[\substack{\text{2- HCOOH / HCOONa} \\ \text{3- H}_2\text{O / HCl}}]{\text{1- O}_2} R_F \diagdown \diagdown OH$$

Scheme. 1.4. Fluorotelomer alcohol synthesis from 1H,1H,2H,2H-perfluoroalkyl-iodides [82].
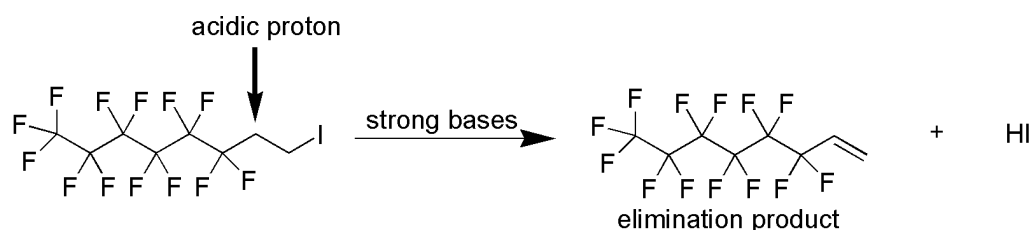
Scheme. 1.5. The elimination product formed by the reaction of strong bases (for example hydroxides) with 1H,1H,2H,2H-perfluoroalkyl iodides hinders the direct fluorotelomer alcohol synthesis via an S_N2 reaction mechanism [82].

Fluorotelomer alcohols are used to synthesize fluorinated nonionic surfactants upon chemically linking it to water-soluble poly(ethylene oxide) (PEO) [99]. The synthesis is achieved by three main strategies. The first method relies on reacting the fluorotelomer alcohol with ethylene oxide in the presence of boron trifluoride (BF3). This method suffers a disadvantage of producing up to 45000 ppm dioxane as a toxic byproduct. Yang et al. managed to decrease the quantity of dioxane produced to 9000 ppm in exchanging BF3 with an aluminum alkoxide and hydrogen fluoride catalyst [99]. Selve and Castro synthesized similar fluorinated surfactants by reacting the fluorotelomer alkoxide with the PEO monooxyphosphonium salt [100]. Fluorotelomer alcohols serve as the starting materials in the synthesis of fluorinated phosphate surfactants and fluorinated

19

carboxylic acids bearing a methylene spacer separating the carboxylic acid group from the perfluorinated chain [99]. They are also used in a variety of applications such in firefighting foams and grease resistant coatings on textiles, carpets, and paper [81]. The superior qualities of fluorotelomer alcohols discussed above do not reveal the whole story. Fluorotelomer alcohols suffer a drawback because their biodegradation products are inert with some exceptions being toxic and accumulate in the environment. They present a biological risk and environmental challenge which are not yet fully understood.

In what follows the discussion will be concentrated on two fluorotelomers used in the experimental part. The first is 1H,1H,2H,2H-perfluoro-1-octanol (F6H2OH) and the second being 1H,1H,2H,2H-perfluoro-1-decanol (F8H2OH). The detection of fluorinated compounds in humans and the environment was the indicator for serious research to achieve a better understanding of possible contamination sources and the biological fate of these environmentally foreign molecules [101-105]. F8H2OH is one of the abundant fluorotelomers and a precursor to perfluorooctanoic acid (PFOA). Liu et al. investigated its solubility in water, water/methanol, water/acetone mixtures, and their sorption by soils in water and water/acetone solutions. They concluded that the F8H2OH solubility increases in the presence of dissolved organic carbon (DOC) in water which may be a concern for places with elevated DOC levels such as landfills [106]. Fasano et al. [107] studied the absorption, distribution, metabolism and elimination of ^{14}C labeled F8H2OH in rats. A 125 mg/kg oral and dermal dose were investigated independently. The oral F8H2OH dose had a peak plasma concentration after 1 h and decreased rapidly with a half-life of 5 h. More than 70 % of the F6H2OH were excreted in the feces, and less than 4 % was excreted in the urine. Glucuronide and glutathione fluorinated conjugates in bile and perfluorohexanoate in the plasma were identified as the metabolites. The presence of perfluorohexanoates in the plasma shows the sequential removal of multiple CF_2 groups. After 7 days, 4-7 % of the given radioactivity was still present in tissues with the highest concentrations in fat, liver, thyroid, and the adrenal glands. After 6 h dermal exposure for a 125 mg/kg dose, 37 % evaporated, 29 % removed by washing and after 7 days radioactivity concentrations were below the limit of detection in most tissues proving that the availability of F8H2OH after dermal exposure is negligible. Ishibashi et al. [108] investigated the effect of F8H2OH and F6H2OH for their *in vivo* estrogenic effects on male medaka (*oryzias latipes*, Japanese rice fish). The fluorotelomer alcohols induced hepatic vitellogenin (VTG) through the activation of Erα in male medaka. Later, Fasano et al. [109] published a detailed study of the kinetics, metabolites, and liver glutathione (GSH) status under daily dosing conditions (prolonged

exposure) of F8H2OH for 45 days in male and female rats. The quantification of several fluorinated compounds including F6H2OH and F8H2OH in the arctic environment was published in a critical review from Butt et al. [110]. The hydrolysis potential of three fluorotelomer esters (8:2 fluorotelomer stearate (FTS), 8:2 fluorotelomer acrylate (FTA), fluorotelomer citrate tri-ester (TBC), and the 2,4-toluenediamine 8:2 fluorotelomer urethane (FTU)) yielding free fluorotelomer alcohol used in the synthesis of polymers for stain resistant textiles [99] was investigated during solvent extraction of soils in different organic solvents. Significant hydrolysis was observed in soils containing microbial enzymes with faster kinetics for polar solvents [111]. The aerobic biodegradation of FTS and TBC was further investigated by Dasu et al. who found that FTS degrades faster than TBC [112]. A detailed review from Post et al. about perfluorooctanoic acid (PFOA), one of the main biodegradation products of F8H2OH, established PFOA as a serious drinking water contamination hazard due to its toxicokinetics and adverse health effects [113]. Recently, the biotransformation of F8H2OH was studied *in vitro* by recombinant human cytochrome P450s, human liver cytosol, and human liver microsomes. The major metabolic pathway was O-glucuronide and O-sulfate conjugation, which gives a reason for the low yield of PFOA in the body from F8H2OH exposure [114]. In short, F8H2OH and its degradation products post a real concern for the environment and health since they were found in human blood [115], affect birth weight and organ growth in children [116,117], and they are presented as residuals in several commercial products [102] from which they are released over time. Fluorotelomer-based surfactants or polymers release with time fluorotelomer alcohols which are usually linked to them via ester or ether bonds. The fluorotelomer alcohols degrade in soil and by soil bacteria to release fluorinated metabolites including PFOA [118]. All of the previously stated drawbacks that apply mainly for perfluorinated chains having a length of eight or more carbons including F8H2OH led to the decline of their industrial production [115,119]. The search for an alternative having similar physical properties as F8H2OH while lacking its toxicity and environmental issues was on. One of the best candidates was F6H2OH, the fluorotelomer alcohol having two perfluorinated methylene groups less than F6H2OH. PFOS and PFOA are quite stable and persistent in human blood since the kidneys can actively transport them back into the blood stream as found by Yang et al. [120].
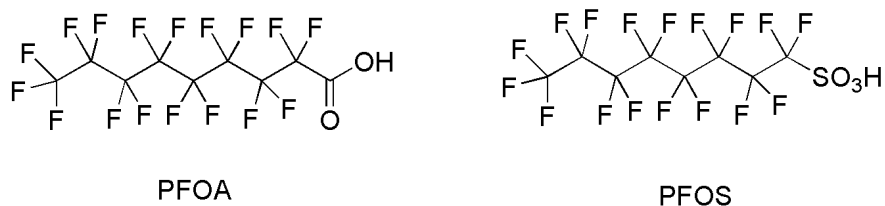
Fig. 1.6. Chemical structures of perfluorooctanoic acid (PFOA) and perfluorooctanesulfonic acid (PFOS).

PFOS and PFOA concentrations are decreasing mainly due to the actions took by the 3M Company to phase out perfluoroalkyl sulfonyl chemistry [121]. A review published by Conder et al. investigated several PFCAs and found out that PFCAs bearing seven or less fluorinated carbons do not bioaccumulate [122]. For instance, a study on the bioaccumulation of PFHx in rainbow trout fish found that it has a very low bioaccumulation potential [123] whereas perfluoroalkyl carboxylates having more than seven perfluorinated carbons have significant bioconcentration factors which increase with the length of the perfluorinated chain [124]. Chengelis et al. compared the toxicology of PFHxA and PFBS and found that PFHxA is eliminated faster than PFBS which suggests PFHxA has a lower tendency to bioaccumulate and the serum concentrations of PFHxA decreased upon repeated oral dosing [125]. The absorption, distribution, metabolism, and excretion of ^{14}C labeled PFHx in rats and mice found that the plasma elimination half-life was 1.5-1.7 h in males in comparison with 0.5-0.7 h in females. The primary elimination route was via the urine, and PFHx was not metabolized in hepatocytes of rats or mice. No other metabolites were detected, and total elimination was realized after 24 h even after the 100 mg/kg dose [126]. The PFHx experiments delivered positive results which opened the door for the F6H2OH as a serious alternative for the more toxic and less biocompatible F8H2OH. The acute, genetic, and subchronic toxicity of F6H2OH was evaluated using *in vitro* and *in vivo* methods. The no-observed-adverse-effect level (NOAEL) was 5 mg/kg/day. The fluorotelomer alcohol proved to be not mutagenic in the mouse lymphoma assay and not clastogenic in a chromosome aberration assay in human lymphocytes [127]. O'Connor et al. investigated the potential development and reproductive toxicity of F6H2OH at doses ranging from 5 to 250 mg/kg/day with no adverse maternal or developmental effects were observed at doses up to 125 mg/kg/day. Up to 25 mg/kg/day doses, no selective reproductive or developmental toxicity was observed so F6H2OH is excluded from the reproductive/developmental toxicity hazard list under the Globally Harmonized System of Classification and Labelling of Chemicals of the United Nations [128]. Russell et al. assessed the

toxicokinetics of F6H2OH and its metabolites in mammals (mice, rats, and human hepatocytes). Four major metabolites (PFBA, PFHxA, PFHpA, and the 5:3 Acid) were determined, and the metabolic pathways in mice, rats, and human hepatocytes all showed similar metabolic pathways. Elimination half-lives of PFHxA, PFHpA and 5:3 acid in humans was estimated from a study done on professional ski wax technicians exposed to fluorinated glide wax and were found to be 32, 70, and 43 days for PFHxA, PFHpA, and 5:3 acid respectively [129]. The chronic toxicity of PFHxA in Sprague-Dawley rats was investigated by Klaunig et al. where they found no effects on body weights, motoric activity, or food consumption after PFHxA exposure. No difference in hematology and serum chemistry was observed at doses up to 100 mg/kg/day [130]. Mukerji et al. studied the effect of systematic repeated-dose of F6H2OH reproductive toxicity in mice and found that the NOAEL for systematic toxicity differs between the two sexes; 5 mg/kg/day for females and 25 mg/kg/day for males [131]. F6H2OH has several advantages over F8H2OH one of which is its lower toxicity. The metabolites resulting from F6H2OH in the human body and mammals are well characterized. The environmental factors of F6H2OH were also considered such as its biodegradation and if possible to find a proper environmentally friendly way of its disposal so that it does not end up having the same problems as F8H2OH. The biodegradation of the F6H2OH was studied by multiple microbial species; three alkane-degrading bacteria (*Mycobacterium vaccae* JOB5, *Pseudomonas oleovorans*, and *Pseudomonas butanovora*) and one fluoroacetate-degrading bacterium (*Pseudomonas fluorescens* DSM 8341). The presence of formate as an external reducing energy source led to the production of perfluorobutanoic acid by *P. fluorescens* DSM 8341 by removing three fluorinated methylene groups. *P. fluorescens* DSM 8341 degraded 5:3 acid to 4:3 acid and perfluoropentanoic acid. *P. oleovorans* produced PFPeA rapidly from F6H2OH in the presence of dicyclopropylketone (alkane hydroxylase inducer) or formate. The addition of lactate to *P. butanovora* led to the slow degradation of F6H2OH and produced several metabolites. This research published by Kim et al. demonstrates that F6H2OH biotransformation mechanisms depend mainly on strain types, enzymes, and inducers [132]. Biodegradation of F6H2OH with wood-rotting fungus, *Phanerochaete chrysosporium*, was tested because fungi are capable of degrading several halogenated compounds including pharmaceuticals [133]. Tseng et al. studied the degradation of F6H2OH by *P. chrysosporium* which transformed the latter to 32-43 mol % polyfluorocarboxylic acid (5:3 acid), 5.9 mol % perfluorocarboxylic acids (PFCAs) including perfluoropentanoic acid (PFPeA) and perfluorohexanoic acid (PFHxA), and transient intermediates including four new F6H2OH conjugates proving the wood-rotting fungus delivers superior

biotransformation qualities than aerobic soil, sludge, and microbial consortia [134]. F6H2OH is currently replacing the former F8H2OH due to its advantages of being less toxic and more environmentally friendly, since the PFHxA produced as its main biodegradation product is less toxic and more biocompatible than PFOA [126].

1.2 Fluorophilicity

Molecules containing one or several carbon-fluorine σ chemical bonds are sometimes called "fluorous" or "fluorophilic" or both which is quite confusing; in what comes next we will try to clarify and solve this problem. In 1994 Horváth and Rábai established the term "fluorous" for compounds partitioning favorably in the perfluoromethylcyclohexane (PFMC) phase of an organic-PFMC biphasic system [135]. Common organic solvents are miscible with PFMC only at elevated temperatures. This thermotropic behavior is used to achieve homogeneous catalysis at high temperatures (one phase). Phase separation into the PFMC phase containing the fluorous catalyst and an organic phase containing the products is achieved by cooling down to ambient temperatures [136]. Juliette et al. successfully achieved to simplify rhodium-catalyzed hydroboration of alkenes and alkyne by running the reactions in fluorous media (PFMC-toluene) [137]. Fluorous catalysis reactions gained popularity due to some advantages over heterogeneous catalysis methods. These advantages include favorable kinetics, simpler separation and less problematic purification steps, chemical stability, solubility tuning with temperature and composition, and the ability to recover fluorous materials after the reaction [138]. Simpler separation methods using fluorous solid-phase extraction (F-SPE) were reviewed extensively by Zhang and Curran [139]. Briefly, the separation and purification of light fluorous [140] molecules is achieved by the preferential adsorption of fluorous molecules on fluorous reverse-phase silica gel. Fluorous solid-phase extraction (F-SPE) purification was used by Matsugi et al. to effectively separate dipeptides tagged with fluorous-FMOC (f-FMOC) bearing C_4F_9 and C_6F_{13} ponytails from non-fluorous by-products [141]. Fluorous Technologies® showed high potential in fields of biocatalysis, microarray, and microfluidic technologies which are highlighted in a feature article by Zhang and Cai [142]. Liquid chromatography applications with fluorocarbon stationary phases proved useful in the reverse phase analysis of polar pharmaceutical and biological samples, and the solvophobicity-fluorophilicity duality of fluorinated stationary phases provides selectivity for organofluorine compounds separation [143]. Lehmler et al. synthesized a series of 1-fluoro-4-

alkylamino-anthraquinones and 1,4-bis-alkylamino-anthraquinones tagged with fluorous ponytails for the development and tailoring of fluorous separations using fluorocarbon functionalized silica since they are easily detected due to their color [144]. Kölmel et al. synthesized rhodamines bearing fluorinated ponytails, bound them to cell penetrating peptoids and managed to simplify their purification process by using F-SPE [145]. The advantages of fluorous synthesis and the relative easiness of the separation methods used such as F-SPE lacked a quantitative understanding of how "heavy" or "light" is the fluorous character of a certain substance. Since most of the reaction systems were based on the PFMC-toluene biphasic system, the natural logarithm of the PFMC-toluene partition coefficient was used to quantify how fluorous a certain substance is [146]. The ln $P_{PFMC/toluene}$ was called a measure of the fluorophilicity. Some statistical and theoretical studies were published that can calculate with high fidelity the PFMC-toluene partition coefficients of several molecules using different methods such as linear free energy relations (LFER) [147], quantitative 3D structure-activity relationships (QSAR) molecular descriptors [146], and molecular surface areas [148]. Hu et al. used 2D and 3D quantitative structure-property relationships (QSPR) models to calculate the fluorophilicity (fluorous scale) with respect to chirality [149]. The ln $P_{PFMC/toluene}$ fluorophilicity scale works fine and is very helpful in organic synthesis. However, biologically relevant molecules bearing organic fluorine are not always fluorous or at best "light-fluorous" (not highly fluorinated) and still having polar functional groups are becoming more common and in use such as fluorinated pharmaceuticals [150] and fluorinated analogs of amino acids [151]. Such molecules usually have polar and aromatic moieties in their structures that drastically decrease their partitioning in the PFMC phase [146] rendering the PFMC-toluene partition coefficient an unsuitable fluorophilicty quantification method for biologically relevant substances. Another rationale is that water is a major component of any biologically relevant system, so a partition coefficient experiment lacking an aqueous phase is most probably irrelevant. The main biphasic system used for biologically relevant systems is the 1-octanol-water partition coefficient which is a well-established quantitative measure of lipophilicity [152-154]. Some fluorinated compounds are still soluble in the 1-octanol phase, so the lipophilicity of these compounds can still be quantified. The problem arises with higher degrees of fluorination when the analyte becomes insoluble in the 1-octanol phase and phase separates into a third fluorophilic phase [155]. In section 5, a biphasic system formed of a fluorotelomer alcohol and water complementary to the 1-octanol / water partition coefficient will be introduced. Organic fluorination, i.e. replacing hydrogen with fluorine atoms has interesting effects on lipophilicity and

acidity. Lipophilicity increases with aromatic fluorination or perfluorination of alkyl chains but decreases with ω-alkyl fluorination (monofluorination) or α-fluorination (trifluoromethyl group) of carbonyl compounds [82,156]. Fluorination also increases hydrogen bond acidity in organic carboxylic acids, aliphatic alcohols, and phenols [156].

1.3 Basics of fluorescence

1.3.1 Absorption and emission of light

Fluorophores are fluorescent chemical compounds that absorb light at certain wavelengths and reemit it at different wavelengths. Since fluorophores play a major role in fluorescence spectroscopy and imaging, a brief introduction into the interactions of light with such compounds becomes a necessity. Simple saturated hydrocarbons having no double or triple bonds absorb light at wavelengths below 160 nm (> 7.8 eV) which is higher than the carbon-carbon single bonds dissociation energy. Light having wavelengths below 200 nm usually ionizes molecules and leads to photochemical decomposition. Single bonds are σ-bonds whereas double and triple bonds bear an extra one or two π-bonds, respectively. Single bonds (σ-electrons) bear rotational symmetry of their wave function with respect to the bond axis whereas the π-electrons have nodes at the nuclei with no rotational symmetry. The π-bonds are weaker than σ-bonds due to their parallel orientation which results in a poor overlap between the component π-orbitals. The π-electrons which are less strongly bound can be excited with lower energy photons and if the chemical structure has two double bonds separated by a single bond, i.e. the two double bonds are conjugated, a red-shift (bathochromic shift) in the absorption is observed which increases with increasing number of conjugated double bonds. When fluorophores are exposed to light having a matching energy for a possible electronic transition within the molecule, some photons are absorbed which leads to the excitation of an electron to a higher energy orbital. A transition between the highest occupied molecular orbital (HOMO) and the lowest unoccupied molecular orbital (LUMO) is usually the energetically favorable transition. The HOMO in a fluorophore is usually the singlet ground state S_0 and the LUMO is the singlet excited state S_1. Light absorbed in the visible spectrum corresponds to transitions having 40-80 kcal/mol gaps between the ground and the excited state, i.e. the band gap between HOMO and LUMO. For example, the LUMO of saturated hydrocarbon lies more than 80 kcal/mol above the HOMO, which explains why such molecules do not absorb light in the visible region i.e. they are colorless. Molecules absorbing light in the visible region have some

weakly bound or delocalized electrons, i.e. their band gaps between HOMO and LUMO lie in the energy range of visible light photons.

1.3.2 Lambert-Beer law and absorption spectroscopy

Absorption of light by liquid solutions, solids, or gases can be expressed in a mathematical way depending on three main parameters: a) concentration or amount of the absorbing material c, b) the optical path length d, and c) the absorption probability of a monochromatic photon called the extinction coefficient ε of the absorbing substance. The absorbance or optical density is defined as the base 10 logarithm of the incident I_0 over transmitted I_t light intensities ratio. The region in which the absorbance is directly proportional to the concentration c and the optical path length d with the extinction coefficient or absorptivity ε as a proportionality constant is described by Lambert-Beer law as given in Eq. 1.1. For non-fluorescent samples, Lambert-Beer law is linear for dilute solutions having an absorbance of less than 1, but for fluorescent samples, the linear regime is valid up to an absorbance of 0.1 after which Lambert-Beer law is not obeyed [157].

$$A = \log\frac{I_0}{I_t} = -\log T = \varepsilon \times c \times d \qquad \textbf{1.1}$$

Because the absorption intensity depends strongly on the wavelength, quantitative UV-Vis measurements are usually done at a specified wavelength.

1.3.3 Fluorescence emission and the Jablonski diagram

Luminescence is the emission of light from electronically excited states from any substance and is divided into two categories: fluorescence and phosphorescence depending on the nature of the excited state. Fluorescence is the rapid relaxation from the ground vibrational state of the excited singlet state which happens on the order of a few nanoseconds (average fluorescence lifetime) accompanied by photon emission. Phosphorescence is the emission of light from a forbidden relaxation from a triplet excited state. It is a rather slow process which occurs on the order of several seconds or minutes. Phosphorescence will not be discussed here, but the discussion will focus on fluorescence. The Jablonski diagram [158] is the starting point in the discussion about light absorption and emission since it illustrates the processes occurring between absorption and emission as shown in Fig. 1.7.
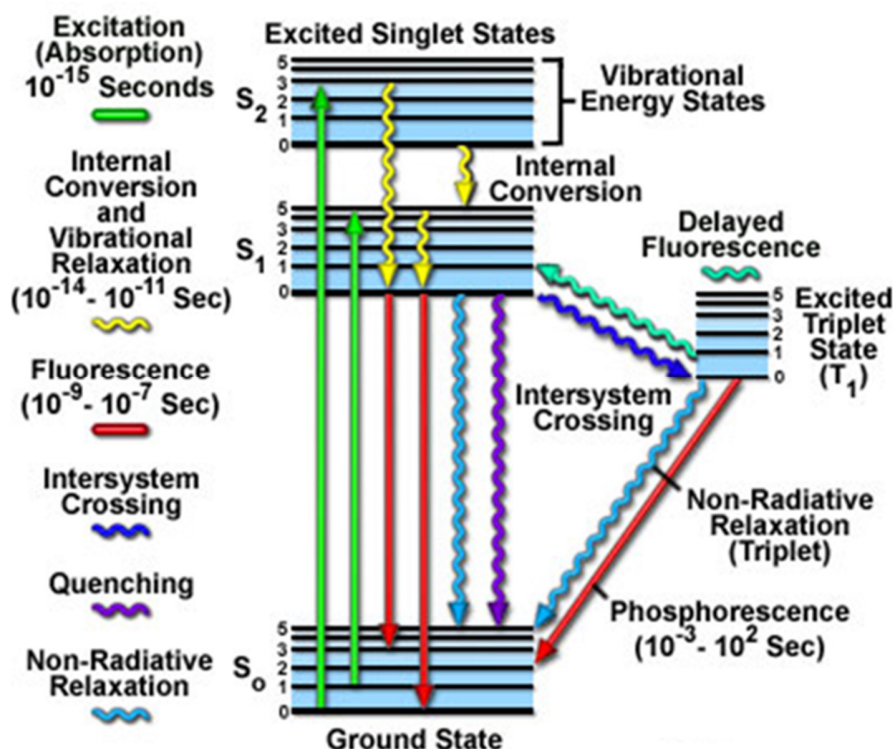
Fig. 1.7. Jablonski energy diagram for typical fluorescence dyes [159].

Light absorption is instantaneous on the order of 10^{-15} s which is a very short time for significant nuclei displacement. Following absorption, a fluorophore is excited to a higher vibrational level of the S_1 or S_2 states. Most molecules in condensed phases rapidly relax to the lowest vibrational level of S_1 i.e. they undergo internal conversion at a time scale of 10^{-12} s. Fluorescence emission occurs from a thermally equilibrated excited S_1 state due to internal conversion taking place on 10^{-12} s time scales (much faster than fluorescence emission bearing typical time scales of 10^{-8} s) which results in complete internal conversion prior to emission. Relaxations from the lowest vibrational state of S_1 typically occur to higher excited vibrational ground states in S_0, which also quickly reaches thermal equilibrium (10^{-12} s). Due to the emission to higher vibrational ground states, the emission and absorption spectra are in many cases mirror images. The mirror image phenomenon also known as the Franck-Condon principle occurs since the electronic excitation does not dramatically alter the nuclear geometry. This results in a similar spacing between the vibrational energy levels of the excited S_1 and the ground S_0 states.

1.3.4 The Franck-Condon principle

The excitation of an electron from the HOMO to the LUMO is realized by a vertical transition as shown in Fig. 1.8.
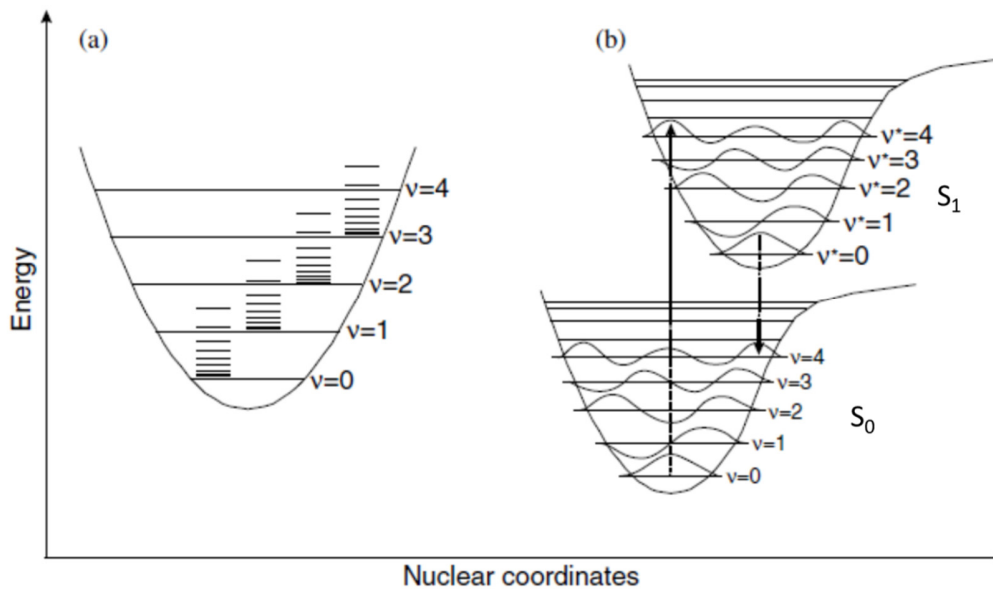
Fig. 1.8. (a) Idealized potential energy curves for a diatomic molecule. In general, polyatomic molecules will have 3N - 6 vibrational modes (v_1, v_2, v_3, etc.) where N is the number of atoms. For each of the 3N – 6 normal vibrations, a potential well exists with a rotational energy ladder. (b) Morse potentials for a molecule in the singlet ground state S_0 and first excited singlet state S_1 to demonstrate the Franck-Condon principle. As electronic transitions are very fast compared with nuclear motions, vibrational levels are favored when they correspond to a minimal change in the nuclear coordinates. The potential wells show transitions between v = 0 and v = 4. In the simplest case of a diatomic molecule, the nuclear coordinate axis refers to the internuclear distance [157].

These vertical transitions are explained by the Born-Oppenheimer approximation based on the fact that the mass of an electron is 1870 times less than the mass of a proton or a neutron which results in electrons moving faster than nuclei. As a result, electronic motions occur as if the nuclei are stationary and fixed in place. Franck and Condon formulated the Frank-Condon principle by applying the Born-Oppenheimer approximation to transitions between electronic energy levels [160-162]. Simply said, the electronic transitions are instantaneous compared with nuclear motions time scales. The Franck–Condon principle is the approximation that an electronic transition is most likely to occur without changes in the positions of the nuclei in the molecular entity and its

environment. The resulting state is called a Franck– Condon state and the transition involved, a vertical transition. The quantum mechanical formulation of this principle is that the intensity of a vibronic transition is proportional to the square of the overlap integral between the vibrational wavefunctions of the two states that are involved in the transition [163]. Upon excitation, the electronic configuration of a molecule changes which sets up a molecular vibration because the nuclei must reorganize to the excited electronic configuration which explains why electronic transitions always occur with vibrational dynamics. Excitation induces a transition to a non-equilibrium state called the Franck-Condon state which undergoes rapid thermal equilibration in liquid solutions at ambient temperatures since fluorophores experience a collision frequency with solvent molecules on the order of 10^{12} collisions per second enabling thermal equilibration on the order of a few picoseconds. Practically the molecules in the electronically excited state S_1 quickly relax to the lowest vibrational level within the S_1 state which is also known as Kasha's rule. The decay to the electronic ground state via photon emission is a statistical phenomenon depending on the quantum yield of the fluorophore. In short, the Franck-Condon principle is applied equally to absorption and emission and Kasha's rule states that the emission will always occur from the lowest vibrational state of the excited singlet state S_1. Both of these principles lead to the mirror symmetry between the absorption and emission spectra of several fluorophores [157]. Exceptions to the mirror-image rule include dyes with a labile proton that can be protonated or deprotonated depending on the pH value or dyes capable of forming excimers, i.e. excited dimers [164].

1.3.5 Temperature effects on absorption and emission spectra

Higher vibrational levels of the ground state are populated with increasing temperature according to the Boltzmann-distribution yielding more transitions from these levels to higher vibrational levels of the excited electronic state which broaden the absorption spectrum. However, lowering the temperature reduces spectral widths and yields more vibrational information. Fluorescence dye solutions capable of forming a clear organic glass when cooled in liquid nitrogen (-196 °C) show well-resolved spectra similar to theoretical calculations. Using a matrix of paraffin at -253 °C, sharp line-like spectra often appear which is termed "Shpolskii effect" [165] since the possibilities for solvation in the paraffin matrix are limited, and each site causes its intrinsic spectral lines in absorption and emission [166].

1.3.6 Stokes shift, solvent relaxation, and solvatochromism

Organic fluorescence dyes consist of some 50-100 atoms each leading to complex vibrational spectra; similarly, an excited fluorophore in the lowest vibrational state of S_1 also has several relaxation possibilities. The solvation shell and other interactions between fluorophores and solvent molecules result in the broadening of vibrational transitions at ambient temperatures. The shift to longer wavelengths of the emission band with respect to the absorption band is called the Stokes shift. Upon excitation, the electron distribution changes and different dipole moments arise forcing solvent molecules to adjust to the new equilibrium configuration in some picoseconds [167-172] at ambient temperatures. The electronic polarization of solvent molecules is instantaneous to the new electron distribution in the molecule after excitation, but this is not the case for the orientational polarization of solvent molecules, and the orientational polarization is not in equilibrium with the excited molecule. The solvent molecules have to undergo dielectric relaxation to reach the equilibrium configuration of the excited state and the same happens upon fluorescence emission, i.e. the orientational polarization of the solvent is conserved during the pseudo-instantaneous optical transition. Consequently, the fluorescence spectrum shows a time-dependent red-shift. Solvent molecules at ambient temperatures undergo dielectric relaxation in less than 10 ps. As a result, at shorter detection wavelengths, fluorescence is controlled by molecules whose solvation shell is incompletely relaxed; whereas at longer wavelengths, the emission is dominated by molecules with completely relaxed solvation shells which explain why the fluorescence lifetimes of blue-shifted fluorophores are always less than the red-shifted ones. Solvatochromism is the effect induced by solvent polarity on the Stokes Shift [173,174]. For a more complete description of solvatochromic effects, the refractive index n and the dielectric constant ε_s of the solvent should be taken into consideration. The change in the dipole moment between the ground μ_g and the excited state μ_e of the fluorophore should also be considered using the Lippert-Mataga equation [175] as shown in Eq. 1.2 which allows the calculation of the Stokes Shift for general solvent effects [157,164].

$$\nu_{abs} - \nu_{em} = \frac{2\left(\mu_e - \mu_g\right)^2}{cha^3}\left[\frac{2(\varepsilon_s-1)}{(2\varepsilon_s+1)} - \frac{2(n^2-1)}{(2n^2+1)}\right] \qquad \textbf{1.2}$$

The Stokes Shift ($\nu_{abs} - \nu_{em}$) in the Lippert-Mataga equation is expressed as a function of the refractive index n and the dielectric constant ε_s of the solvent, dipole moments of the fluorophore in the ground μ_g and excited μ_e states, the speed of light c, the Planck's constant h, and the Onsager radius of the fluorophore a which is approximately 60 % of the longitudinal axis of the fluorophore. Some fluorescence dyes show more solvatochromism than others, for example; coumarin dyes have an increasing Stokes shift with increasing solvent polarity whereas rhodamine dyes do not show strong solvatochromism.

1.3.7 The fluorescence quantum yield

The fluorescence quantum yield denoted as Φ_f for a fluorophore is the ratio of the emitted to absorbed photons as shown in Eq. 1.3 where k_r is the radiative rate constant and k_{nr} the non-radiative constant including internal conversion, intersystem crossing, or other quenching mechanisms [157].

$$\Phi_f = \frac{k_r}{k_r + k_{nr}} \qquad \text{1.3}$$

A quantum yield of unity is impossible to reach, but some general guidelines can be followed to get a high quantum yield fluorescence dye. For instance, fluorescence dyes bearing rigid structures minimize radiationless deactivation due to rotations and vibrations of side groups and avoiding heavy atoms in the fluorophore keeps the intersystem crossing rate constant low. Absolute quantum yield determination of a fluorescence dye can be accurately measured by thermal blooming [176-179] and the integration sphere method [180,181]. Briefly, the thermal blooming method takes advantage of the heat generated in the region of the absorption leading to an increase in the local temperature thus modifying the refractive index and inducing what is called as an optical lens which is negative for most liquids. Within a period of a few tenths of a second which is the time required for the thermal lens to develop, the laser beam is observed as a blooming spot a few meters behind the sample. The quantum yield of the sample is calculated from accurate spot size with time observations. Relative quantum yield calculations are less problematic and can be measured with simple UV-Vis and fluorescence spectrometers by comparing the unknown samples with standard solutions [180,181]. The simplest way to determine the fluorescence quantum yield of a dye is to

use a fluorescence standard bearing a similar absorption to the unknown sample at a certain wavelength. In our case, the appropriate standard filling those prerequisites was fluorescein disodium salt [181].

1.4 Confocal light microscopy

As the thickness of the microscopy specimen increases, light from above and below the focal plane of the microscope reduces the quality of the image dramatically. This loss, in contrast, is due to the light produced from the out-of-focus planes which reduce the signal-to-noise (S/N) ratio. The confocal microscope is designed to remove the obscuring out-of-focus light, tremendously ameliorating axial and lateral resolution [182]. The confocal microscope is credited to Minsky where he described a microscope using a point source focused on a small area of the specimen instead of the classical wide-field illumination [182]. Light from the illuminated area is focused to a small spot on the image plane. In short, a point light source is in conjugate (confocal) at the sample and at the image plane as illustrated in Fig. 1.9.
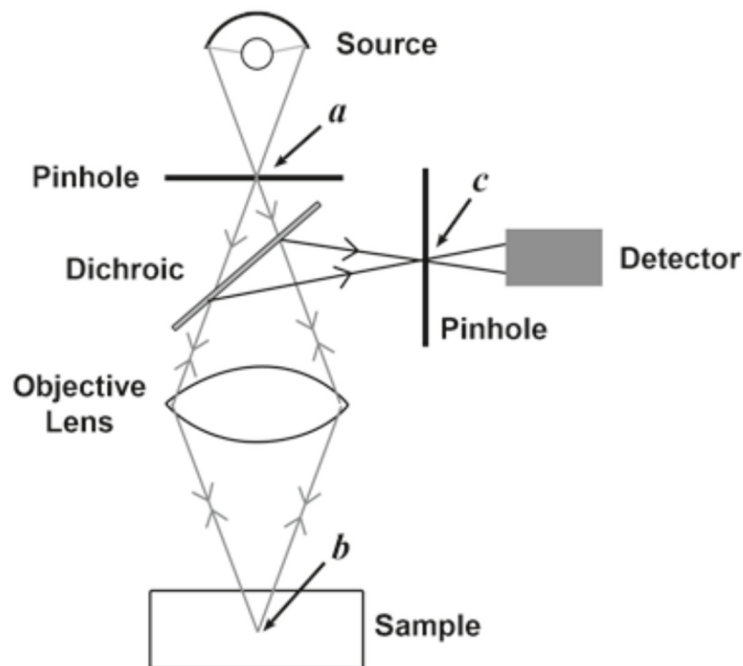
Fig. 1.9. An epi-illumination setup for a confocal microscope. The objective lens acts as the condenser and light emitted from the specimen is reflected by the dichroic mirror and focused on the exit pinhole. Light from above or below the focal point is out of focus which does not reach the detector [182].

Since a single point in a specimen does not provide much information, the spot is scanned across the image. In the original design by Minsky, the sample was laterally moved which was slow and prone to vibrations, but in the late 1980s scanning the sample was achieved by moving the light sources. This new approach achieved faster scanning rates and increased interest in confocal microscopy mainly for biological research [183]. Another kind of confocal microscopes was developed by Petrán, who used a multipoint scan or area scan technique realized by a spinning disk (Nipkow wheel) [184,185].

1.5 Langmuir monolayers

1.5.1 Langmuir trough

The decrease in surface tension of water by olive oil spreading on the water surface was firstly quantified by Lord Rayleigh, and the thickness of the oil film was estimated to be 16 Å [186]. Shortly after, Pockels discovered experimentally that the surface tension of water dropped after spreading a certain amount of oil on the water surface [187,188]. Later, in 1917 Langmuir published a great deal of evidence proving the monomolecular nature of films spread on water with an insight on the orientation of the molecules forming the monolayer [189]. Langmuir was a pioneer in investigating monolayers from pure substances rather than oils, and he developed the Langmuir trough based on the work done previously by Pockels. In 1920, Langmuir was able to transfer monomolecular films onto solid substrates [190] and in 1935, Blodgett was successful in developing a method that deposits 2, 3, or more layers of molecules up to more than 200 layers on glass and various metals [191]. Such deposited monolayers are currently known as Langmuir-Blodgett films. Currently, Langmuir monolayer experiments are conducted in an apparatus called Langmuir trough usually consisting of a PTFE trough with movable barriers as shown in Scheme 1.6.
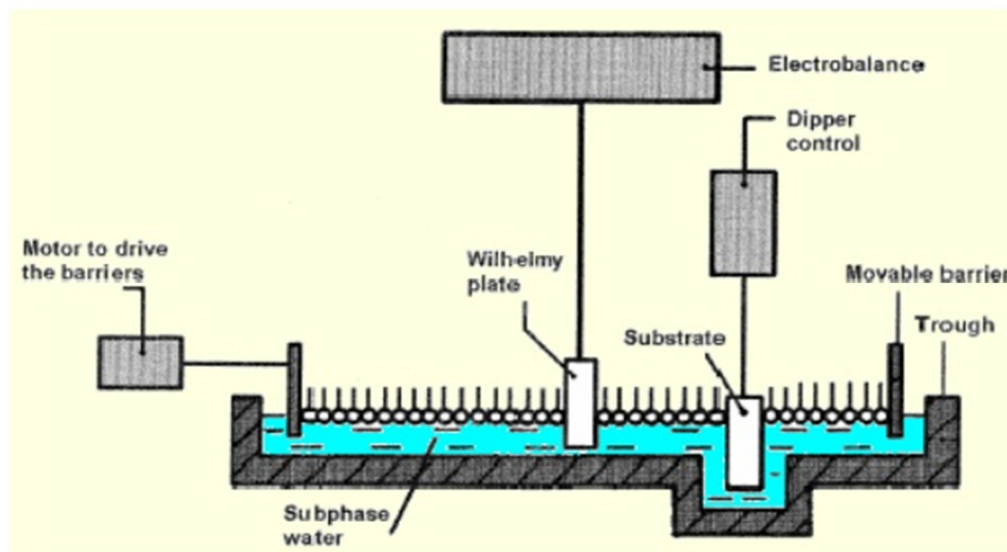
Scheme 1.6. Langmuir trough that contains an electrobalance with a Wilhelmy plate for surface pressure measurements and a dipper control used to transfer Langmuir-Blodgett films onto a substrate [192].

Langmuir monolayer experiments are usually carried out by spreading a known amount of amphiphilic molecules dissolved in a water-immiscible and volatile organic solvent such as chloroform. The organic solvent evaporates fast, and the monolayer is compressed by moving the barriers. Typically surface pressure (π)-area (A) isotherms are obtained. Strict conditions are needed to achieve reproducibility such as a clean and if possible dust-free environment, the use of highest purity solvents for spreading and the highest purity aqueous subphases. The π-A isotherm is a measure of the increase in surface pressure i.e. two-dimensional pressure versus the area available per molecule on the aqueous subphase. Continuous compression of the monolayer with simultaneous surface pressure measurements using the Wilhelmy plate method are a routine. The Wilhelmy plate is made of platinum or filter paper partially immersed in the subphase and connected to a sensitive electrobalance. Information about monolayer phases, molecular area, collapse behavior, compressibility, monolayer stability, and mixing behavior can be obtained from π-A isotherms [192]. Valuable information on phase transitions is gained from the π-A isotherms. Amphiphiles having a hydrophilic headgroup and a long chain aliphatic moiety such as stearic acid (SA) readily form monolayers on the air-water interface and their Langmuir isotherms are extensively studied. A typical π-A isotherm for SA on water showing the different phases of the

35

monolayer is portrayed in Fig. 1.10. SA has a flexible aliphatic chain and therefore has in the π-A isotherm two phase transitions, whereas rigid amphiphiles show a single gas to condensed phase transition such as perfluorinated carboxylic acids [193,194]. The fluorocarbon chains are rigid and form a helix with minimal conformational defects yielding a hexagonally ordered phase at small areas per molecule [193].
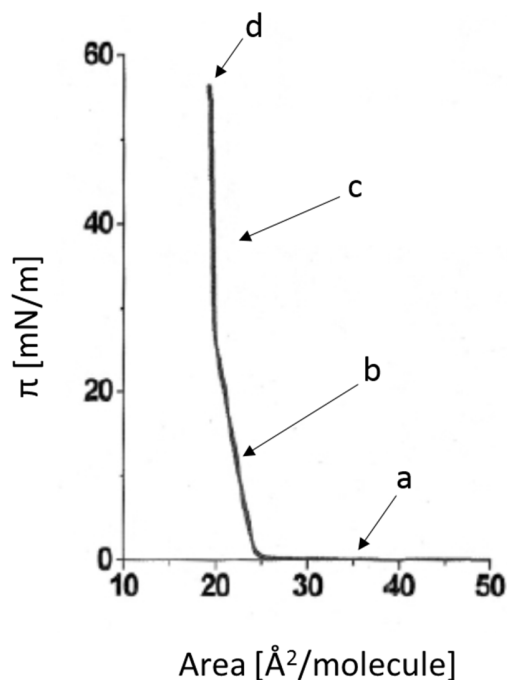
Fig. 1.10. π-A Langmuir isotherm of SA monolayer on water at 20 °C. The different phases of the monolayer are shown, namely the gaseous phase (a), the liquid-condensed (b), the condensed phase (c), and the monolayer collapse (d) [192].

On the other hand, phospholipid monolayers typically undergo a first-order transition from the gas to the fluid (LE) phase and further compression results in another first-order transition to the LC phase. Decreasing the area per molecule further, leads to a second-order phase transition from the LE to the solid phase [195].

1.5.2 Epifluorescence microscopy on the air-water interface

Epifluorescence microscopy permits fluorescence investigations on surfaces and interfaces where transmission microscopy cannot be realized. For instance, adding a minute amount of fluorescence dyes, having a preferential affinity to different phases of the monolayers at the air-water interface

establishes an imaging technique suitable for the direct observations of film morphologies [196-200]. A contrast between bright (dye enriched) and dark (dye depleted) domains appears, which can be used to investigate the affinities of fluorescence dyes towards different phases in immiscible mixed monolayers too which is achieved by systematically changing the composition of the mixed monolayer. A scheme of an epifluorescence microscope is shown in Fig. 1.11. The right choice of fluorescence dye, excitation and emission filters, and the dichroic mirror is very important to ensure good and reliable results. Epifluorescence coupled with π-A isotherms for Langmuir monolayers provide additional information about domain formation, size, and shape [192].
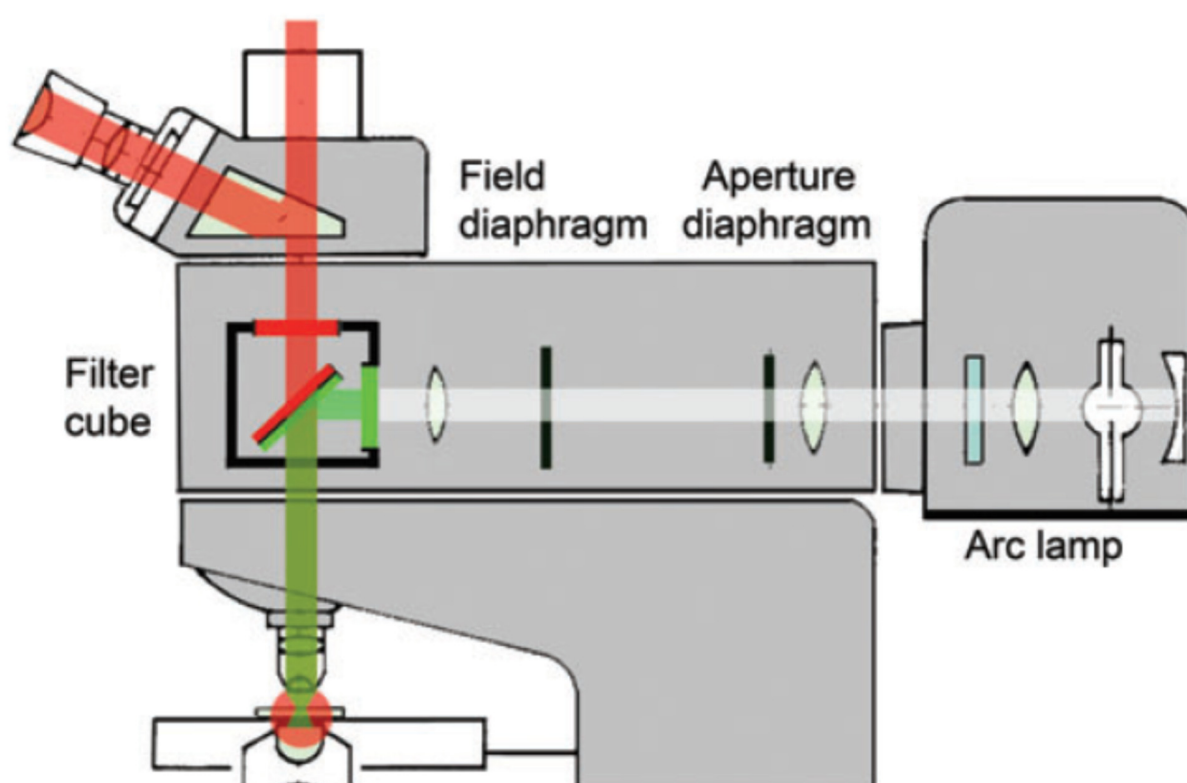
Fig. 1.11. Scheme of an epifluorescence microscope [201].

1.6 Aim of the work

The main aim was to synthesize fluorophilic fluorescence dyes and to quantify their fluorophilicity. Such dyes might be useful for the recognition of fluorophilic domains with well-established fluorescence techniques. Rhodamine (Rh) fluorescence dyes have high quantum yields and are resistant to photobleaching making them important candidates in well-established fluorescence techniques which use lasers for fluorophore excitation such as in CLSM [202]. The work was

initiated with the synthesis of rhodamine-based fluorescence dyes bearing perfluoroalkyl chains linked to the amine groups through an aliphatic spacer consisting of one or two methylene groups. The length of the perfluorinated chain attached to the fluorinated rhodamine dyes (F-rhodamines) was systematically increased in an attempt to get fluorescence dyes with different fluorophilicities. As the length of the perfluorinated chain increases, the affinity of the synthesized F-rhodamines to fluorophilic phases should also increase. It is already published that the functionalization of rhodamine-based fluorescence dyes with perfluorinated alkyl moieties increases their affinity to fluorous stationary phases used in F-SPE columns [145]. The rhodamine core provides a stable fluorescence with high quantum yields, and the attached perfluorinated moieties contribute to its fluorophilic character. A similar approach was chosen for this work and four F-rhodamines were synthesized. The length of the perfluorinated chain and the aliphatic spacer were varied in an attempt to elucidate their effect on fluorophilicity.

The affinity of the F-rhodamines to fluorinated phases was investigated at first qualitatively in immiscible Langmuir monolayers of long-chain perfluorinated and aliphatic carboxylic acids such as perfluorostearic acid (FC18) and stearic acid (SA) which yield phase separated monolayers at room temperature [203]. Epifluorescence microscopy coupled with surface pressure (π)-area (A) isotherm measurements of FC18 and SA mixed monolayers at different mixing ratios was used to qualitatively characterize the fluorophilic/lipophilic character of the synthesized F-rhodamines. The Rh-C_2H_4-$C_{10}F_{21}$ (F-rhodamine bearing the longest perfluorinated chain) and the Rh-CH_2-C_3F_7 (F-rhodamine bearing the shortest perfluorinated chain) were tested with FC18 and SA mixed monolayers changing systematically the FC18/SA molar ratio in an attempt to check the difference in the affinity of the dyes to fluorophilic and lipophilic domains. It is expected that Rh-C_2H_4-$C_{10}F_{21}$ shows a higher affinity to fluorophilic domains compared to the less fluorinated Rh-CH_2-C_3F_7 dye. Afterwards, CLSM investigations of fluorotelomer alcohol-phospholipid mixed GUVs were performed to examine the partitioning behavior of the synthesized F-rhodamines within the lipophilic phospholipid bilayer with a systematic change in the fluorotelomer alcohol content. The F-rhodamines bearing the longest F-ponytails are expected to partition in the fluorotelomer alcohol containing GUVs. The ability of the four synthesized F-rhodamine fluorescence dyes to incorporate into lipid membranes was tested with mixed DOPC/F6H2OH and DPPC/F8H2OH GUVs obtained via electroformation. The GUVs were double stained with ATTO-633-DOPE, bearing two oleoyl acyl chains similar to DOPC, and the F-rhodamines. The ATTO-633-DOPE was used to stain the lipid membrane, and the F-rhodamines were added to test their incorporation into the pure

phospholipid or the mixed GUVs. The affinity of the F-rhodamines to the mixed GUVs is expected to increase with the length of the perfluorinated ponytail. The incorporation of the F-rhodamines bearing longer perfluorinated moieties into mixed GUVs should increase when the fluorotelomer alcohol to phospholipid molar ratio increases. Also, the ability of the F-rhodamines to stain pure phospholipid GUVs was investigated.

Finally, the partition coefficient of the F-rhodamines between fluorinated phases and other immiscible organic or aqueous phases were determined to quantify their fluorophilicity and distinguish it from lipophilicity for biologically relevant systems. 1-Octanol bearing a polar headgroup and a flexible lipophilic tail is amphiphilic in a comparable way to phospholipids and proteins found in cell membranes making the 1-octanol/water partition coefficient a suitable model for partitioning between bio and aqueous phases [154]. Perfluoroalkyl chains and fluorine substituents have several effects on the physicochemical properties of biologically relevant compounds. The fluorine atom has a high electronegativity, small size, and very low polarizability upon which proton substitutions with fluorine lead to several consequences one of which is the increase or decrease of lipophilicity [156]. Upon the increase in the length of perfluorinated chains for perfluorinated surfactants or perfluorocarboxylic acids, the classical 1-octanol/water partition coefficient is confronted with some limitations. Due to the low solubility in the 1-octanol and water phases which leads to a third phase formation, some approximations are used, such as the ratio of their solubility in the pure organic and aqueous phases [204]. Solubility problems even make it increasingly more difficult to predict the partitioning behavior of numerous highly fluorinated compounds such as fluorotelomer alcohols and fluorotelomer olefins and thus rely heavily on modeling and approximations [205]. Another problem with the perfluorinated carboxylic acids is the failure of the 1-octanol/water partition coefficient to explain their lipophilicity due to their very low pK_a values rendering them ionized at environmentally relevant pH which requires more sophisticated and time-consuming methods to evaluate and understand their bioaccumulation [206]. The 1-octanol/water partition coefficient seems to have a limited success for some lightly-fluorinated alcohols and carbohydrates [207]. When dealing with highly fluorinated molecules, a fluorous partition coefficient between PFMC and toluene is normally used and sometimes termed fluorophilicity [149]. The PFMC/toluene partition coefficient became famous after a paper published by Horváth and Rábai in 1994 where they used the PFMC/toluene biphasic system to conduct hydroformylation of olefins by using fluorous cobalt or rhodium catalysts which after the reaction partition favorably into the PFMC phase simplifying the purification process [135]. The

PFMC/toluene partition coefficient is highly relevant to the transition metal catalyzed synthesis due to several advantages including simple purification processes and good catalyst recovery [138]. Additionally, progress was achieved in the ability to calculate the PFMC/toluene partition coefficient with high fidelity using 3D QSAR descriptors and artificial neural networks, linear free energy relation (LFER), and molecular surface areas [146-148]. However, the PFMC/toluene partition coefficient is not biologically relevant mainly due to the absence of an aqueous phase, and compounds partitioning in the PFMC phase need to be highly fluorinated and lack the presence of polar groups, hydrogen bonding capabilities, and π-π interactions [146]. The problems encountered using the 1-octanol/water or PFMC/toluene partition coefficients trigger the need for an extra partition coefficient between a fluorinated phase and water that has biological relevance and can complement the well-established 1-octanol/water partition coefficient. The 1-octanol phase was substituted with the more fluorophilic 1H,1H,2H,2H-perfluoro-1-octanol (F6H2OH) and the partition coefficients for the four F-rhodamines in the F6H2OH/W biphasic system were determined.

2 Synthesis of fluorinated rhodamine (Rh) fluorescence dyes

2.1 Motivation

Rhodamine fluorescence dyes have high quantum yields and are stable and resistant to photobleaching making them important candidates in well-established fluorescence techniques which use lasers for fluorophore excitation such as in CLSM [202]. Functionalizing rhodamine-based fluorescence dyes with perfluorinated alkyl moieties increases their affinity to fluorous stationary phases used in F-SPE columns [145]. The rhodamine cores provide stable fluorescence dyes with high quantum yields, and the attached perfluorinated moieties contribute to their fluorophilic character. Based on those facts, a similar approach was used to synthesize four fluorinated rhodamine-based fluorescence dyes (F-rhodamines). The length of the perfluorinated chain and the aliphatic spacer, between the amine group of the rhodamine core and the perfluoroalkyl ponytail, were systematically changed in an attempt to elucidate their effect on fluorophilicity.

2.2 Materials

m-Anisidine, heptafluorobutyric anhydride, perfluoropalmitic acid (PFPA), and phthalic anhydride were purchased from Alfa Aesar. Triethylamine (TEA), pyridine, anhydrous dichloromethane (DCM), anhydrous tetrahydrofuran (THF), agarose super LM, tert-butyl methyl ether (MTBE), diethyl ether, *n*-hexane, ethanol, and chloroform were purchased from Carl Roth. Lithium aluminum hydride [2 M] THF solution, boron tribromide [1 M] dichloromethane solution, propionic acid, *p*-toluenesulfonic acid monohydrate, pentadecafluorooctanoyl chloride, 3-aminophenol, 1-iodo-1*H*,1*H*,2*H*,2*H*-perfluorodecane, 1-iodo-1*H*,1*H*,2*H*,2*H*-perfluorododecane, anhydrous 1-methyl-2-pyrrolidone (NMP), ethyldiisopropylamine (DIPEA), and nonafluorobutyl methyl ether (HFE-7100) were purchased from Sigma-Aldrich. 1,2-dipalmitoyl-*sn*-glycero-3-phosphocholine (DPPC) was purchased from Avanti Polar Lipids. Rhodamine B 1,2-dihexadecanoyl-*sn*-glycero-3-phosphoethanolamine (Rh-DPPE) was purchased from Thermo Fisher Scientific. Deuterated solvents for solution NMR spectroscopy (CDCl$_3$, CD$_3$OD, DMSO-d_6, and THF-d_8) were purchased from Armar Chemicals. All chemicals were used without further purification.

2.3 Synthetic procedure

Solution NMR spectra were recorded at 27 °C by Agilent Technologies 400 MHz ^{1}H VNMRS spectrometer or Agilent Technologies 500 MHz ^{1}H DD2 spectrometer. Samples were dissolved in deuterated solvents (CDCl$_3$, CD$_3$OD, DMSO-d_6, or THF-d_8). ^{1}H and ^{13}C NMR spectra were reported relative to TMS, ^{19}F spectra relative to CFCl$_3$, and ^{13}C NMR spectra were proton decoupled.

ESI-ToF measurements were performed on a Focus micro ToF by Bruker Daltonics. The samples were dissolved in 2,2,2-trifluoroethanol (TFE) to a final concentration of 30 μM and directly infused (180.00 μL/h, positive mode).
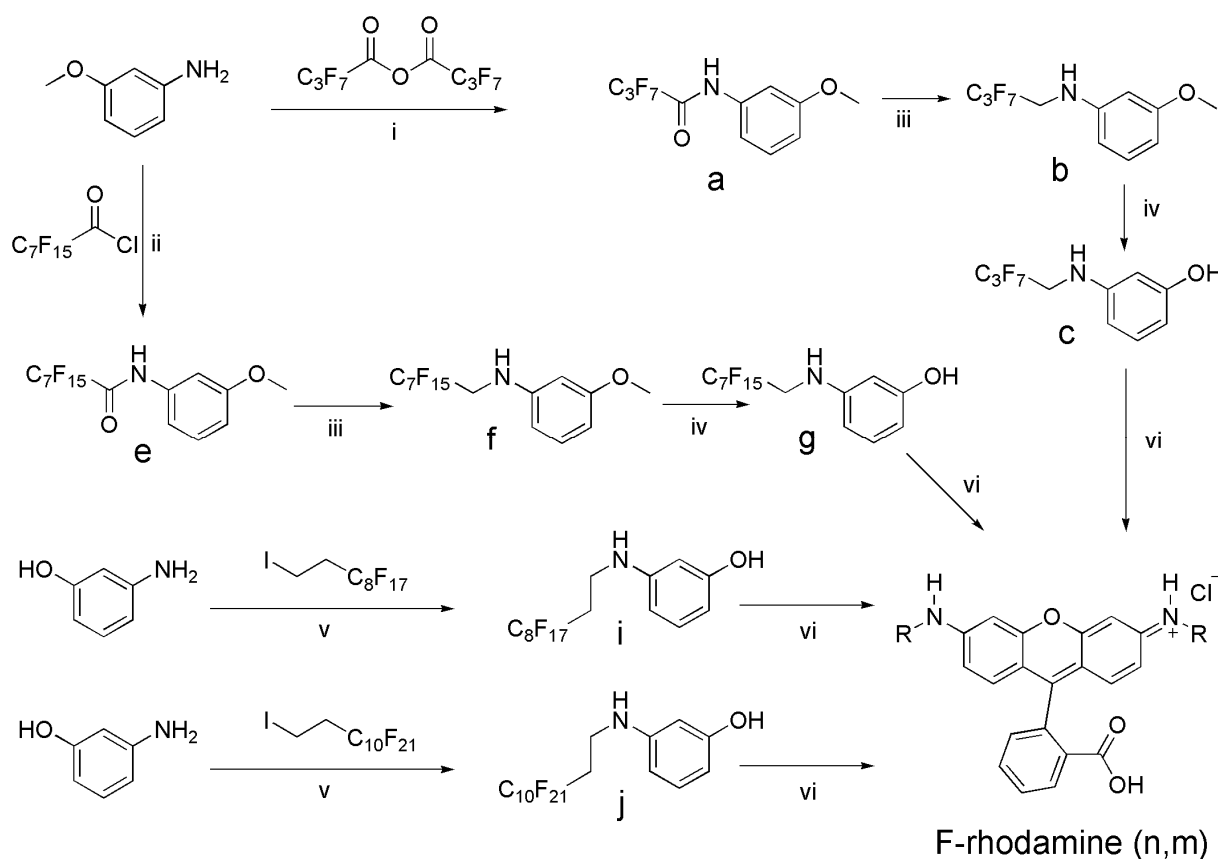
Scheme 2.1. Synthesis of F-rhodamines Rh-C$_n$H$_{2n}$-C$_m$F$_{2m+1}$. i) DCM, TEA, 0 °C to RT, 12 h, ii) DCM, pyridine, 0 °C to RT, 12 h; iii) THF, LiAlH$_4$, reflux, 12 h; iv) DCM, BBr$_3$, reflux, 12 h; v) NMP, DIPEA, 100 °C, 24 h; vi) propionic acid, phthalic anhydride, *p*-toluenesulfonic acid monohydrate, 160 °C, 24 h. The following F-rhodamines (n,m) were synthesized **d**(1,3), **h**(1,7), **k**(2,8), and **l**(2,10).

2.3.1 Rh-CH$_2$-C$_3$F$_7$ synthesis

Secondary amide intermediate (**a**): 5 g (40.6 mmol) *m*-anisidine, 19.98 g (48.72 mmol) heptafluorobutyric anhydride, and 0.493 g (4.872 mmol) triethylamine were added to a Schlenk flask equipped with a magnetic stirrer, containing 50 mL anhydrous DCM maintained at 0 °C in an ice-water bath. The reaction was left under continuous stirring for 1 h in the ice-water bath then removed and left under constant stirring at RT overnight. The reaction was opened to the atmosphere, and the organic phase was further diluted with 100 mL DCM. The DCM phase was washed three times with 5 wt % NaHCO$_3$ aqueous solution, one time with water, three times with 0.01 M HCl aqueous solution, and three times with sodium chloride brine. The DCM phase was dried over sodium sulfate, filtered and concentrated at 30 °C using a rotary evaporator under reduced pressure. 150 mL *n*-hexane were added to the round bottom flask and heated to boiling. The clear warm *n*-hexane phase was decanted into a beaker, and the product was left to crystallize at 4 °C overnight. The product was filtered with a Büchner funnel, washed with portions of cold *n*-hexane and dried under vacuum at RT. Recrystallization from *n*-hexane was repeated a second time to give compound (**a**) as a white solid with 54 % yield. ^{1}H NMR (400 MHz, CDCl$_3$) δ 7.86 (s, 1H), 7.33 – 7.27 (m, 2H), 7.07 – 7.01 (m, 1H), 6.83 – 6.78 (m, 1H), 3.83 (s, 3H). ^{13}C NMR (101 MHz, CDCl$_3$) δ 160.34 (s), 136.17 (s), 130.10 (s), 112.46 (s), 112.36 (s), 106.20 (s), 55.42 (s). ^{19}F NMR (376 MHz, CDCl$_3$) δ -80.51 (t, $J = 8.8$ Hz, 3F), -120.06 – -120.50 (m, 2F), -126.54 – -126.87 (m, 2F).

Secondary amine intermediate (**b**): 2 g (6.27 mmol) C$_3$F$_7$-sec-amide (**a**) were transferred into a two-neck round-bottom flask equipped with a magnetic stirrer, reflux condenser and a drying tube filled with calcium chloride. 40 mL THF were added followed by 7.84 mL (15.68 mmol) of a 2 M lithium aluminum hydride in THF solution. The reaction was refluxed for 12 h, left to cool down slowly to RT, and quenched with 1 mL water. The THF phase was filtered, diluted with 200 mL DCM, and filtered a second time. The organic phase was washed two times with water, twice with 5 wt % NaHCO$_3$ aqueous solution and twice with NaCl brine. The organic phase was dried over sodium sulfate, filtered and evaporated at 30 °C using a rotary evaporator under reduced pressure. The product was purified by silica gel column chromatography with mobile phase composition cyclohexane/ethyl acetate 4:1 (v/v) to obtain compound (**b**) as a slightly yellow viscous liquid with 61 % yield. ^{1}H NMR (400 MHz, CDCl$_3$) δ 7.12 (t, $J = 8.1$ Hz, 1H), 6.37 (dd, $J = 8.2, 2.3$ Hz, 1H), 6.30 (dd, $J = 8.1, 2.1$ Hz, 1H), 6.24 (t, $J = 2.3$ Hz, 1H), 3.92 – 3.79 (m, 3H), 3.78 (s, 3H). ^{13}C NMR

(101 MHz, CDCl$_3$) δ 160.83 (s), 147.76 (s), 130.19 (s), 106.08 (s), 104.12 (s), 99.58 (s), 55.13 (s), 44.18 (t, J = 23.4 Hz). ^{19}F NMR (376 MHz, CDCl$_3$) δ -80.74 (t, J = 9.4 Hz, 3F), -118.89 – -119.22 (m, 2F), -127.54 – -127.73 (m, 2F).

Secondary amino phenol intermediate (**c**): 1 g (3.277 mmol) C$_3$F$_7$-CH$_2$-sec-amine (**b**) was transferred to a two-neck round-bottom flask equipped with a magnetic stirrer, reflux condenser and a drying tube filled with calcium chloride. 20 mL DCM were added followed by 4.92 mL (4.92 mmol) of 1 M boron tribromide solution in DCM. The reaction was refluxed for 12 h, left to cool down slowly to RT, and quenched with 1 mL water. The DCM phase was added to 100 mL 5 wt % NaHCO$_3$ aqueous solution and the pH was checked with pH paper to be around 8. The product was extracted with portions of DCM, and the organic portions were combined and washed three times with NaCl brine, dried over sodium sulfate and filtered. DCM was removed on a rotary evaporator at 30 °C under reduced pressure. The product was purified by silica gel column chromatography with mobile phase composition cyclohexane/ethyl acetate 3:1 (v/v) to obtain compound (**c**) as a brownish waxy solid with 58 % yield. ^{1}H NMR (400 MHz, DMSO-d_6) δ 9.03 (s, 1H), 6.93 – 6.82 (m, 1H), 6.19 – 6.11 (m, 2H), 6.09 – 6.05 (m, 1H), 6.05 – 5.98 (m, 1H), 3.96 – 3.81 (m, 2H). ^{13}C NMR (101 MHz, DMSO-d_6) δ 158.60 (s), 149.46 (s), 129.99 (s), 105.16 (s), 104.21 (s), 100.07 (s), 43.28 (t, J = 22.5 Hz). ^{19}F NMR (376 MHz, DMSO-d_6) δ -80.29 (t, J = 9.4 Hz, 3F), -117.46 – -117.76 (m, 2F), -127.05 – -127.40 (m, 2F).

Rh-CH$_2$-C$_3$F$_7$ (**d**): 246.6 mg (0.8469 mmol) C$_3$F$_7$-CH$_2$-amino-phenol (**c**), 100.4 mg (0.6778 mmol) phthalic anhydride, 564.6 mg (7.621 mmol) propionic acid, and 12.08 mg (0.0635 mmol) *p*-toluenesulfonic acid monohydrate were added to a Schlenk flask equipped with a magnetic stirrer. The reaction was carried out in a 160 °C thermostated oil bath for 24 h under a nitrogen atmosphere and continuous stirring. The reaction was left to cool down, and the Schlenk flask was opened to the atmosphere. The products were dissolved in chloroform/ethanol 10:1 (v/v) mixture, filtered and washed six times with 0.1 M HCl aqueous solution. The organic phase was dried over sodium sulfate and filtered. The product was purified by silica gel column chromatography with a chloroform/methanol 3:1 (v/v) mobile phase and later precipitated from a concentrated acetone solution into excess cold *n*-hexane. The product was filtered using a Büchner funnel and washed with portions of cold *n*-hexane then put under vacuum at RT to yield Rh-CH$_2$-C$_3$F$_7$ (**d**) as an orange solid with 24 % yield. ^{1}H NMR (400 MHz, CD$_3$OD) δ 8.16 (d, J = 7.5 Hz, 1H), 7.79 (td, J = 7.4, 1.2 Hz, 1H), 7.74 (td, J = 7.5, 1.0 Hz, 1H), 7.32 (d, J = 7.3 Hz, 1H), 6.94 – 6.86 (m, 4H), 6.79 –

6.75 (m, 2H), 4.18 (t, J = 15.7 Hz, 4H). ^{19}F NMR (376 MHz, CD$_3$OD) δ -82.33 (t, J = 9.7 Hz, 6F), -119.19 – -119.47 (m, 4F), -128.45 – -129.00 (m, 4F). ESI-ToF, m/z: calculated for $C_{28}H_{17}F_{14}N_2O_3$ 695.101 [M]$^+$; found 695.0288.
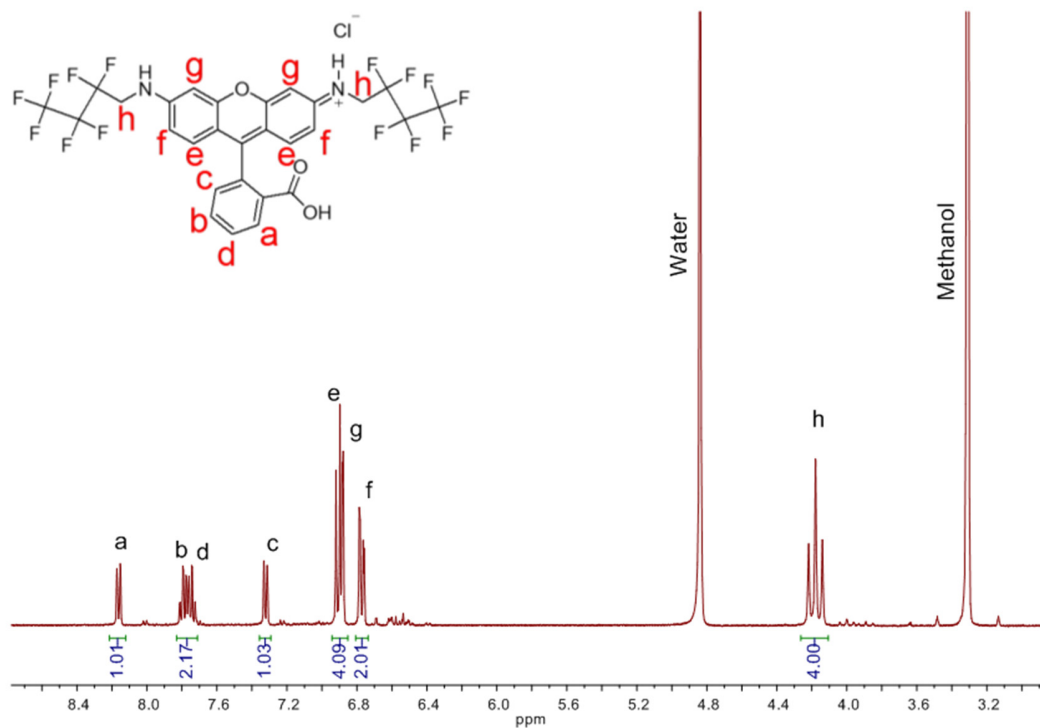
Fig. 2.1. ^{1}H NMR spectrum (400 MHz, CD$_3$OD) of Rh-CH$_2$-C$_3$F$_7$.
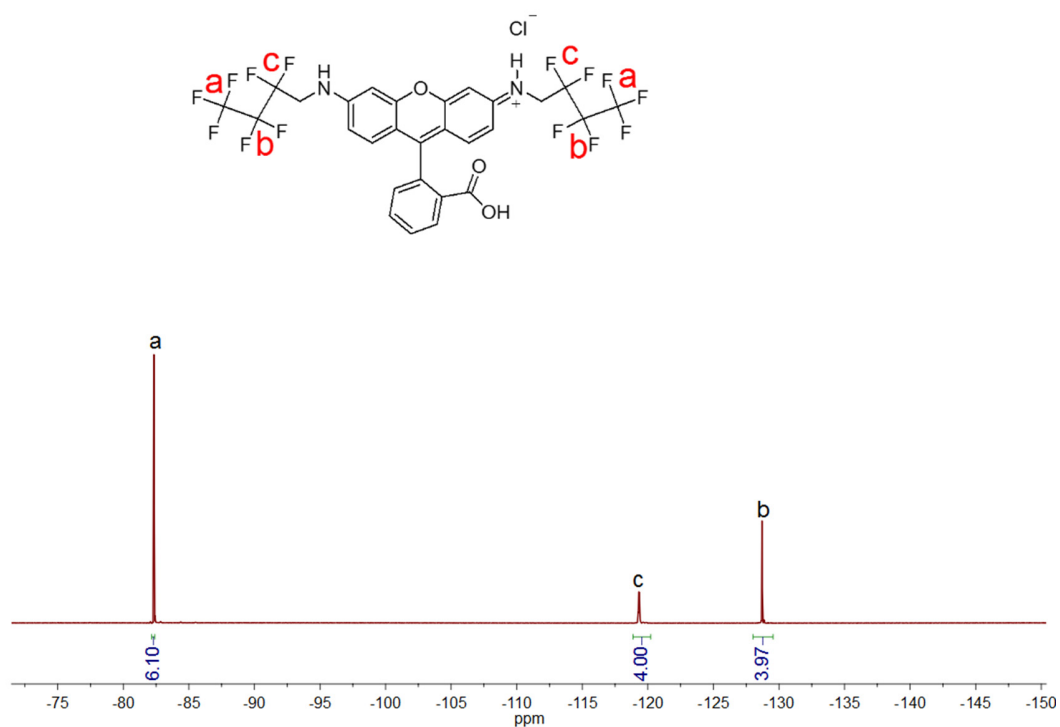
Fig. 2.2. ^{19}F NMR spectrum (376 MHz, CD$_3$OD) of Rh-CH$_2$-C$_3$F$_7$.
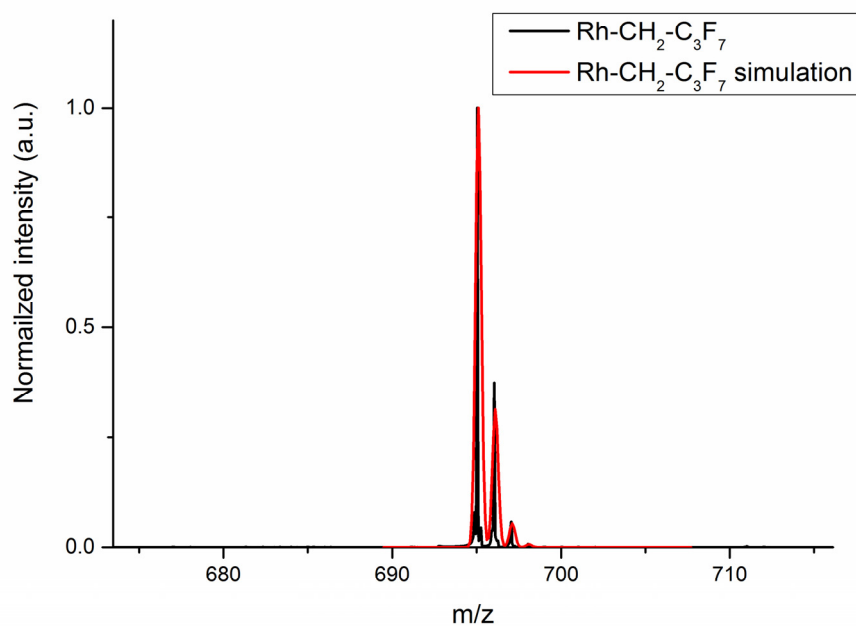
Fig. 2.3. Rh-CH$_2$-C$_3$F$_7$ ESI-ToF spectrum of a 30 µM TFE solution; m/z: 695.0288 [M]$^+$, simulated m/z: 695.101 for C$_{28}$H$_{17}$F$_{14}$N$_2$O$_3$.

2.3.2 Rh-CH$_2$-C$_7$F$_{15}$ synthesis

Secondary amide intermediate (**e**): 5 g (11.56 mmol) pentadecafluorooctanoyl chloride, 1.186 g (9.631 mmol) *m*-anisidine, and 0.9525 g (12.04 mmol) pyridine were added to a Schlenk flask equipped with a magnetic stirrer, containing 50 mL DCM maintained at 0 °C in an ice-water bath. The reaction was left under continuous stirring for one hour in the ice-water bath then at RT overnight. The reaction was opened to the atmosphere, and the organic phase was further diluted with 100 mL DCM and filtered to remove part of the precipitated pyridinium chloride. The DCM phase was washed three times with 0.01 M HCl aqueous solution, one time with water, three times with 5 wt % NaHCO$_3$, three times with NaCl brine, dried over sodium sulfate, and filtered. The DCM phase was concentrated with a rotary evaporator at 30 °C under reduced pressure until the onset of turbidity. Approximately 250 mL *n*-hexane were added to the DCM concentrate and the solution was heated to boiling. The upper clear organic phase was decanted into a beaker and allowed to crystallize at RT overnight to yield the product C$_7$F$_{15}$-secondary amide (**e**) as a white solid with 59 % yield. ^{1}H NMR (500 MHz, CDCl$_3$) δ 7.87 (s, 1H), 7.32 – 7.27 (m, 2H), 7.04 (ddd, J = 8.1, 2.0, 0.6 Hz, 1H), 6.80 (ddd, J = 8.4, 2.4, 0.7 Hz, 1H), 3.82 (s, 3H). ^{13}C NMR (126 MHz, CDCl$_3$) δ 160.35 (s), 136.19 (s), 130.09 (s), 112.47 (s), 112.35 (s), 106.20 (s), 55.41 (s). ^{19}F NMR (470 MHz, CDCl$_3$) δ -80.77 (tt, J = 10.1, 2.4 Hz, 3F), -119.21 – -119.34 (m, 2F), -121.31 – -121.55 (m, 2F), -121.80 – -122.04 (m, 2F), -122.15 – -122.32 (m, 2F), -122.56 – -122.81 (m, 2F), -126.02 – -126.15 (m, 2F).

Secondary amine intermediate (**f**): 1 g (1.926 mmol) C$_7$F$_{15}$-secondary amide (e) was transferred into a two-neck round-bottom flask equipped with a magnetic stirrer, reflux condenser, and a drying tube filled with calcium chloride. 30 mL THF were added followed by 2.4 mL (4.8 mmol) of a 2 M lithium aluminum hydride solution in THF. The reaction was refluxed for 12 hours, left to cool down slowly to RT and quenched with 0.5 mL water. The THF phase was filtered to remove insoluble salts, diluted with 200 mL diethyl ether, and filtered. The organic phase was washed one time with water, twice with 5 wt % NaHCO$_3$ aqueous solution and twice with sodium chloride brine. The organic phase was dried over sodium sulfate and filtered. The organic solvents were evaporated at 30 °C using a rotary evaporator under reduced pressure to obtain compound (**f**) as a yellowish viscous liquid with 68 % yield. No further purification steps were needed. ^{1}H NMR (500 MHz, CDCl$_3$) δ 7.12 (t, J = 8.1 Hz, 1H), 6.39 – 6.36 (m, 1H), 6.32 – 6.29 (m, 1H), 6.25 (t, J = 2.3

Hz, 1H), 3.97 – 3.80 (m, 3H), 3.78 (s, 3H). ^{13}C NMR (126 MHz, CDCl$_3$) δ 160.84 (s), 147.76 (s), 130.18 (s), 106.06 (s), 104.11 (s), 99.56 (s), 55.11 (s), 44.40 (t, J = 23.2 Hz). ^{19}F NMR (470 MHz, CDCl$_3$) δ -80.79 (tt, J = 10.1, 2.4 Hz, 3F), -117.90 – -118.37 (m, 2F), -121.63 – -121.90 (m, 2F), -121.91 – -122.21 (m, 2F), -122.56 – -122.87 (m, 2F), -123.11 – -123.53 (m, 2F), -125.90 – -126.34 (m, 2F).

Secondary amino phenol intermediate (**g**): 0.5 g (0.99 mmol) C$_7$F$_{15}$-CH$_2$-secondary amine (f) was transferred into a two-neck round-bottom flask equipped with a magnetic stirrer, reflux condenser and a drying tube filled with calcium chloride. 20 mL DCM were added followed by 1.5 mL (1.5 mmol) 1 M boron tribromide solution in DCM and refluxed for 12 h. The reaction was left to cool down slowly to RT and quenched with 0.25 mL water. The DCM phase was added to 100 mL 5 wt % NaHCO$_3$ aqueous solution and the pH was checked with pH paper to be around 8. The product was extracted with portions of DCM, and the organic portions were combined and washed three times with NaCl brine, dried over sodium sulfate and filtered. DCM was removed on a rotary evaporator at 30 °C under reduced pressure to obtain compound (**g**) as a brownish waxy solid with 73 % yield. No further purification steps were needed. ^{1}H NMR (500 MHz, CDCl$_3$) δ 7.06 (t, J = 8.1 Hz, 1H), 6.28 (d, J = 2.3 Hz, 1H), 6.27 (d, J = 2.3 Hz, 1H), 6.20 (t, J = 2.3 Hz, 1H), 4.78 (s, 1H), 3.96 – 3.76 (m, 3H). ^{13}C NMR (126 MHz, CDCl$_3$) δ 156.67 (s), 148.03 (s), 130.40 (s), 106.11 (s), 106.07 (s), 100.23 (s), 44.33 (t, J = 23.3 Hz). ^{19}F NMR (470 MHz, CDCl$_3$) δ -80.80 (tt, J = 10.1, 2.4 Hz, 3F), -117.84 – -118.42 (m, 2F), -121.57 – -121.90 (m, 2F), -121.91 – -122.21 (m, 2F), -122.57 – -122.93 (m, 2F), -123.17 – -123.47 (m, 2F), -125.96 – -126.29 (m, 2F).

Rh-CH$_2$-C$_7$F$_{15}$ (**h**): 300 mg (0.6107 mmol) C$_7$F$_{15}$-CH$_2$-phenol (g), 72.39 mg (0.4887 mmol) phthalic anhydride, 407.3 mg (5.498 mmol) propionic acid, and 8.716 mg (0.04582 mmol) *p*-toluenesulfonic acid monohydrate were added to a Schlenk flask equipped with a magnetic stirrer. The reaction was carried out in a 160 °C thermostated oil bath for 24 h under a nitrogen atmosphere and continuous stirring. The reaction was left to cool down, and the Schlenk flask was opened to the atmosphere. The products were dissolved in chloroform/ethanol 10:1 (v/v) mixture, filtered and washed six times with 0.1 M HCl aqueous solution. The organic phase was dried over sodium sulfate and filtered. The product was purified by silica gel column chromatography with a chloroform/methanol 5:1 (v/v) mobile phase and later precipitated from a concentrated acetone solution into excess cold *n*-hexane. The product was filtrated using a Büchner funnel and washed with portions of cold *n*-hexane then put under vacuum at RT to obtain Rh-CH$_2$-C$_7$F$_{15}$ (**h**) as an

orange solid with 19 % yield. ^{1}H NMR (500 MHz, CD$_3$OD) δ 8.02 (d, J = 7.4 Hz, 1H), 7.74 (td, J = 7.5, 1.2 Hz, 1H), 7.68 (td, J = 7.5, 1.0 Hz, 1H), 7.24 (d, J = 7.5 Hz, 1H), 6.72 – 6.68 (m, 4H), 6.61 – 6.57 (m, 2H), 4.08 (t, J = 15.8 Hz, 4H). ^{19}F NMR (470 MHz, CD$_3$OD) δ -82.40 (tt, J = 10.1, 2.4 Hz, 6F), -118.41 – -118.87 (m, 4F), -122.59 – -122.88 (m, 4F), -122.89 – -123.21 (m, 4F), -123.59 – -123.92 (m, 4F), -124.12 – -124.43 (m, 4F), -127.14 – -127.53 (m, 4F). ESI-ToF, m/z: calculated for C$_{36}$H$_{17}$F$_{30}$N$_2$O$_3$ 1095.0755 [M]$^+$; found 1094.9658.
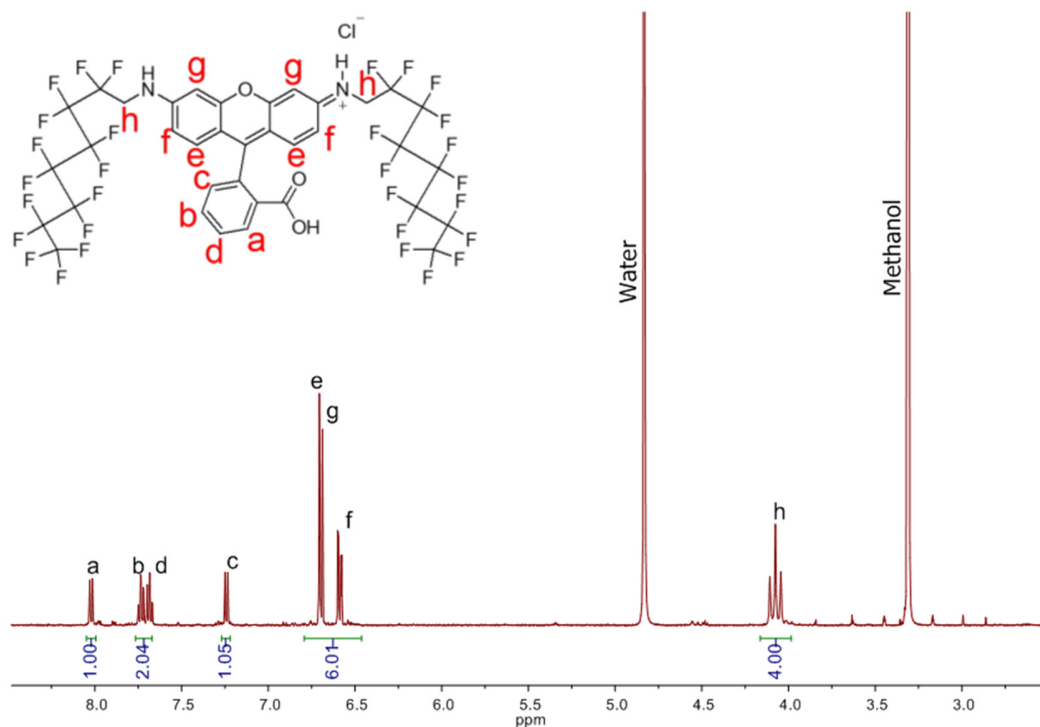
Fig. 2.4. ^{1}H NMR spectrum (500 MHz, CD$_3$OD) of Rh-CH$_2$-C$_7$F$_{15}$.
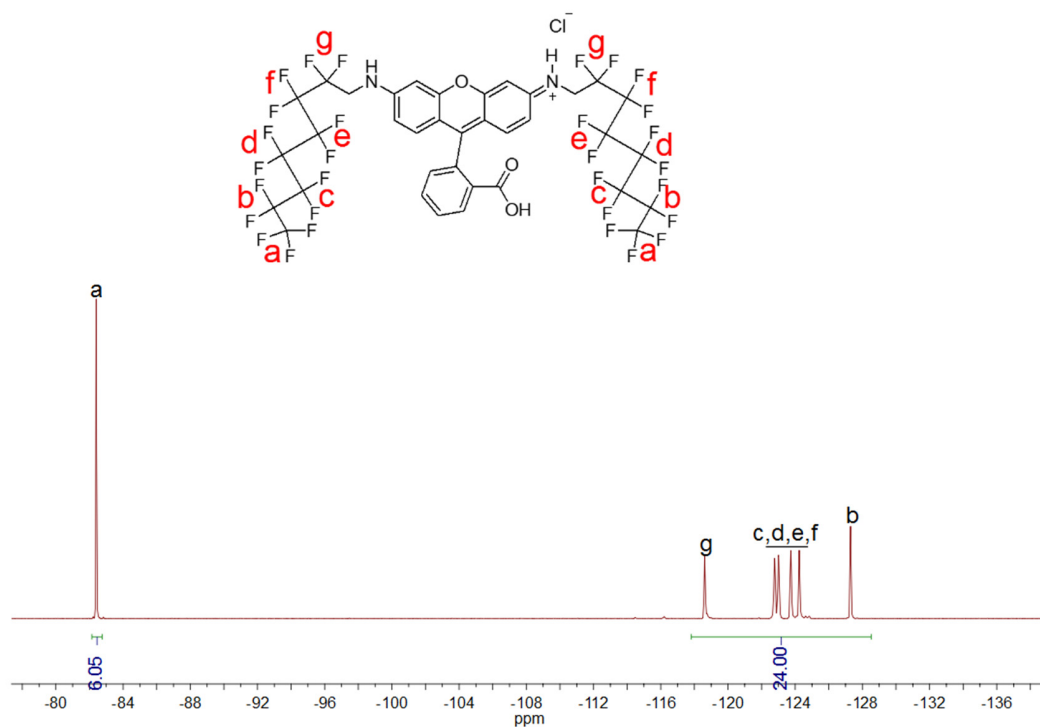
Fig. 2.5. ^{19}F NMR spectrum (470 MHz, CD$_3$OD) of Rh-CH$_2$-C$_7$F$_{15}$.
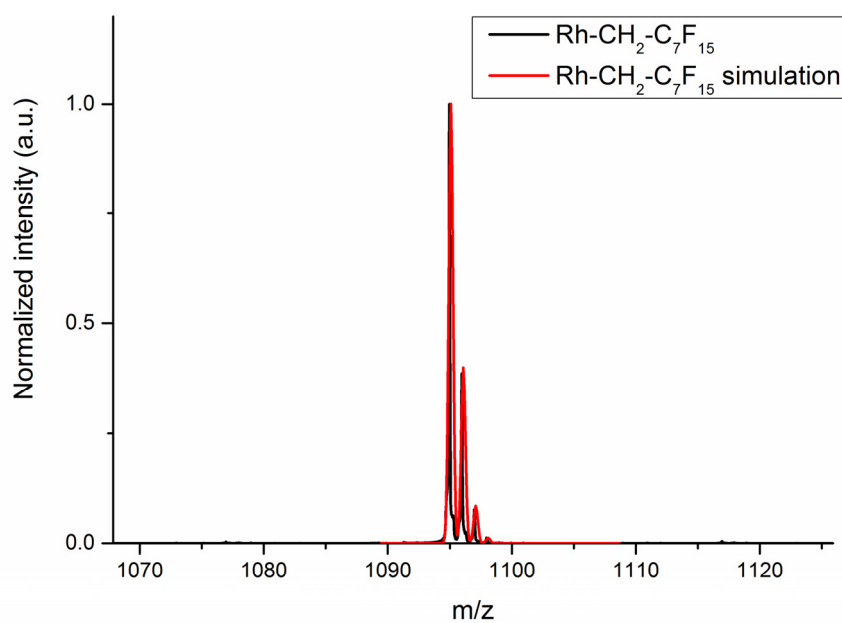
Fig. 2.6. Rh-CH$_2$-C$_7$F$_{15}$ ESI-ToF spectrum of a 30 µM TFE solution; m/z: 1094.9658 [M]$^+$, simulated m/z: 1095.0755 for C$_{36}$H$_{17}$F$_{30}$N$_2$O$_3$.

2.3.3 Rh-C_2H_4-C_8F_{17} synthesis

Secondary amino phenol intermediate (**i**): 861.2 mg (7.892 mmol) 3-aminophenol, 10 g (17.42 mmol) 1-Iodo-1H,1H,2H,2H-perfluorodecane, 20 mL NMP, and 2.559 g (19.80 mmol) DIPEA were transferred into a Schlenk flask equipped with a magnetic stirrer. The reaction mixture was bubbled with nitrogen for 30 min then transferred to a 100 °C thermostated oil bath and kept under stirring for 24 h. The Schlenk flask was removed from the oil bath and left to cool down to RT then opened to the atmosphere. The reaction was diluted with 300 mL MTBE and filtered to remove the precipitated DIPEA.HI salt. The organic phase was washed ten times with a 10 wt % NaCl aqueous solution (w/w), dried over sodium sulfate, and filtered. The MTBE phase was evaporated on a rotary evaporator at 40 °C under reduced pressure, and the product was purified by silica gel column chromatography with an n-hexane/MTBE 1:1 (v/v) mobile phase yielding C_8F_{17}-C_2H_4-phenol (**i**) as an off-white solid with 61 % yield. ^{1}H NMR (400 MHz, CDCl$_3$) δ 7.05 (t, J = 8.0 Hz, 1H), 6.25 – 6.17 (m, 2H), 6.14 – 6.08 (m, 1H), 4.59 (s, 1H), 3.79 (s, 1H), 3.52 (t, J = 7.1 Hz, 2H), 2.53 – 2.26 (m, 2H). ^{19}F NMR (376 MHz, CDCl$_3$) δ -80.76 (t, J = 10.0 Hz, 3F), -113.49 – -114.13 (m, 2F), -121.24 – -122.21 (m, 6F), -122.44 – -122.92 (m, 2F), -123.17 – -123.70 (m, 2F), -125.75 – -126.36 (m, 2F).

Rh-C_2H_4-C_8F_{17} (**k**): 0.6 g (1.081 mmol) C_8F_{17}-C_2H_4-phenol (i), 128.1 mg (0.8648 mmol) phthalic anhydride, 0.721 g (9.73 mmol) propionic acid, and 15.42 mg (81.06 µmol) p-toluenesulfonic acid monohydrate were added to a Schlenk flask equipped with a magnetic stirrer. The reaction was carried out in a 160 °C thermostated oil bath for 24 h under nitrogen atmosphere and continuous stirring. The reaction was left to cool down, and the Schlenk flask was opened to the atmosphere. The products were dissolved in chloroform/THF/ethanol 10:1:1 (v/v/v) mixture, filtered and washed six times with 0.1 M HCl aqueous solution. The organic phase was dried over sodium sulfate and filtered. Organic solvents were evaporated on a rotary evaporator at 45 °C under reduced pressure and silica gel column chromatography with gradient elution starting from diethyl ether/THF 25:1 (v/v) and slowly increasing the THF portion reaching a final mobile phase composition of diethyl ether/THF 1:1 (v/v) was used to obtain the Rh-C_2H_4-C_8F_{17} (**k**) as a red solid. The product was dissolved in a small quantity of acetone and precipitated into excess cold n-hexane, filtered using a Büchner funnel and dried under vacuum at RT to obtain Rh-C_2H_4-C_8F_{17} (**k**) as a red solid with 23 % yield. ^{1}H NMR (500 MHz, THF-d_8) δ 7.91 (d, J = 7.6 Hz, 1H), 7.65

(td, J = 7.5, 1.1 Hz, 1H), 7.59 (td, J = 7.5, 0.7 Hz, 1H), 7.16 (d, J = 7.6 Hz, 1H), 6.48 (d, J = 8.6 Hz, 2H), 6.42 (d, J = 2.3 Hz, 2H), 6.30 (dd, J = 8.7, 2.3 Hz, 2H), 5.55 (t, J = 6.1 Hz, 2H), 3.56 – 3.48 (m, 4H), 2.58 – 2.45 (m, 4H). ^{19}F NMR (376 MHz, THF-d_8) δ -81.81 (-81.81 (t, J = 10.1 Hz, 6F), -114.37 – -114.78 (m, 4F), -121.84 – -122.92 (m, 12F), -123.06 – -123.58 (m, 4F), -123.69 – -124.35 (m, 4F), -126.55 – -127.18 (m, 4F). ESI-ToF, m/z: calculated for $C_{40}H_{21}F_{34}N_2O_3$ 1223.1004 $[M]^+$; found 1222.9859.
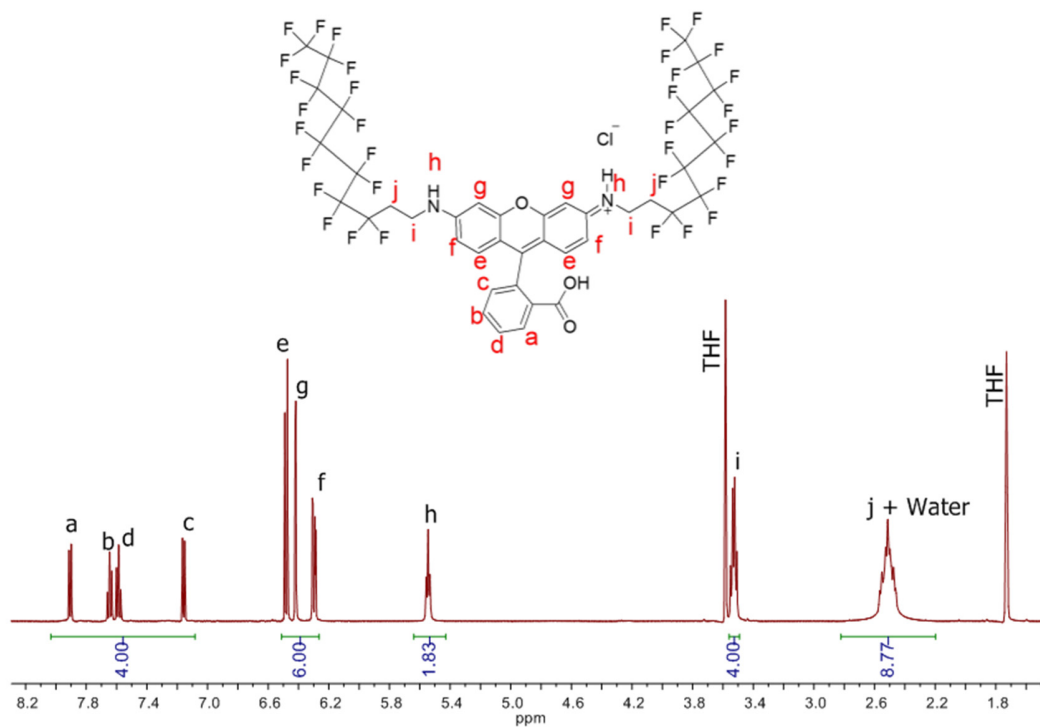
Fig. 2.7. ^{1}H NMR spectrum (500 MHz, THF-d_8) of Rh-C$_2$H$_4$-C$_8$F$_{17}$.
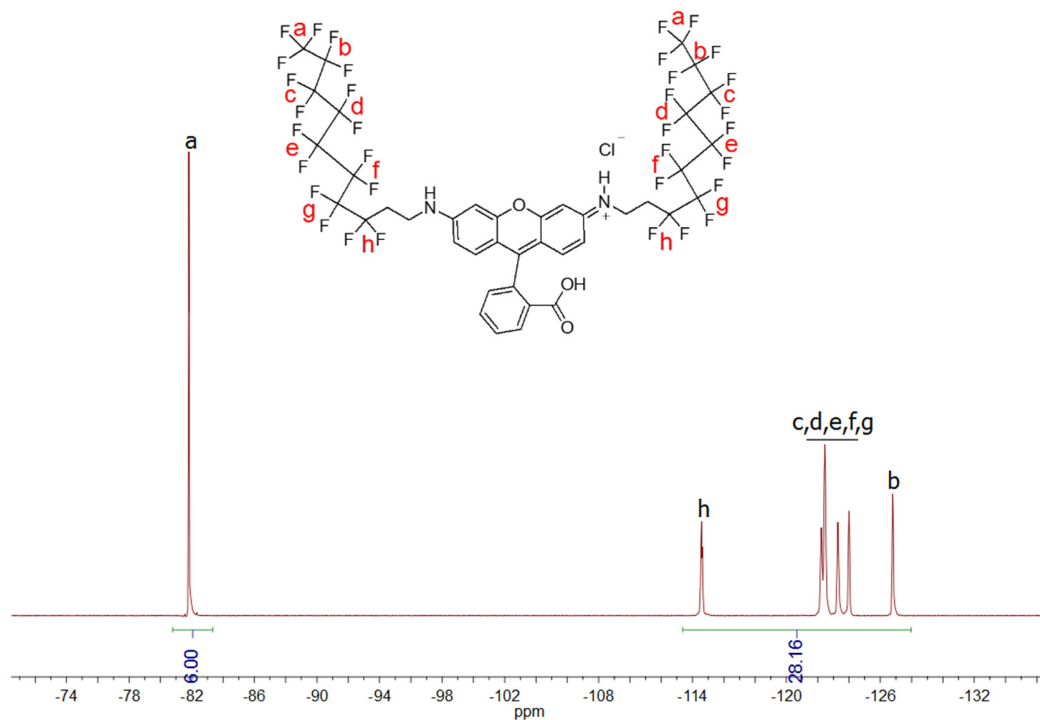
Fig. 2.8. ^{19}F NMR spectrum (376 MHz, THF-d_8) of Rh-C$_2$H$_4$-C$_8$F$_{17}$.
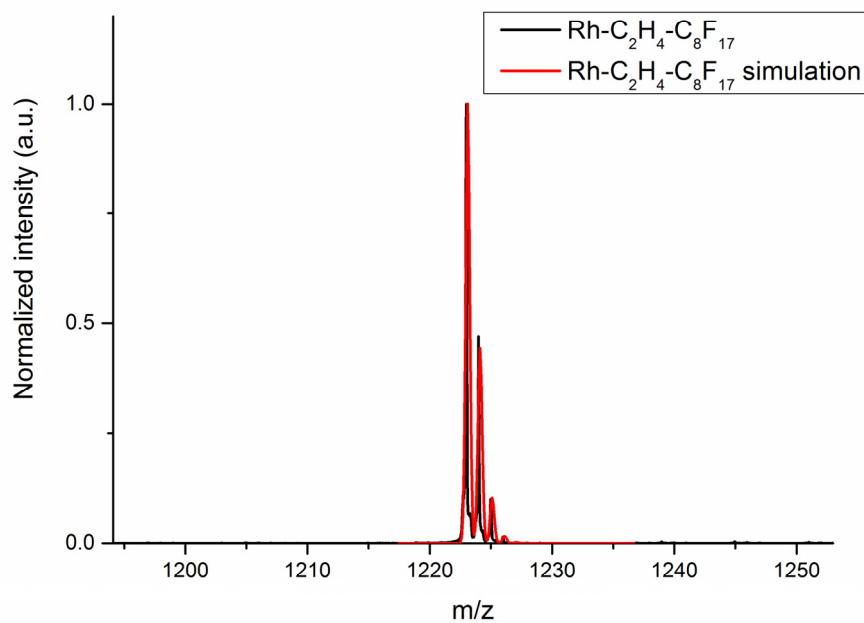
Fig. 2.9. Rh-C$_2$H$_4$-C$_8$F$_{17}$ ESI-ToF spectrum of a 30 µM TFE solution; m/z: 1222.9859 [M]$^+$; simulated m/z: 1223.1004 for C$_{40}$H$_{21}$F$_{34}$N$_2$O$_3$.

2.3.4 Rh-C_2H_4-$C_{10}F_{21}$ synthesis

Secondary amino phenol intermediate (**j**): 184 mg (1.686 mmol) 3-aminophenol, 2.5 g (3.709 mmol) 1-Iodo-1H,1H,2H,2H-perfluorododecane, 15 mL NMP, and 0.545 g (4.217 mmol) DIPEA were transferred into a Schlenk flask equipped with a magnetic stirrer. The reaction mixture was bubbled with nitrogen for 30 min then transferred to a 100 °C thermostated oil bath and kept under stirring for 24 h. The Schlenk flask was removed from the oil bath and left to cool down to RT then opened to the atmosphere. The reaction was diluted with 200 mL MTBE and filtered to remove the precipitated DIPEA.HI salt. The organic phase was washed six times with a 10 wt % NaCl aqueous solution (w/w), dried over sodium sulfate and filtered. The MTBE phase was evaporated on a rotary evaporator at 40 °C under reduced pressure, and the product was crystallized twice from a clear boiling n-hexane solution at RT to yield $C_{10}F_{21}$-C_2H_4-secondary amino phenol (**j**) as an off-white solid with 70 % yield. ^{1}H NMR (500 MHz, CDCl$_3$) δ 7.06 (t, J = 8.0 Hz, 1H), 6.25 (ddd, J = 8.0, 2.3, 0.7 Hz, 1H), 6.21 (ddd, J = 8.1, 2.2, 0.7 Hz, 1H), 6.14 (t, J = 2.3 Hz, 1H), 3.80 (s, 1H), 3.57 – 3.46 (m, 2H), 2.49 – 2.32 (m, 2H). ^{19}F NMR (470 MHz, CDCl$_3$) δ -80.76 (t, J = 10.0 Hz, 3F), -113.65 – -113.98 (m, 2F), -121.23 – -122.11 (m, 10F), -122.49 – -122.86 (m, 2F), -123.20 – -123.73 (m, 2F), -125.82 – -126.34 (m, 2F).

Rh-C_2H_4-$C_{10}F_{21}$ (**l**): 458 mg (0.699 mmol) $C_{10}F_{21}$-C_2H_4-secondary amino phenol (j), 82.83 mg (0.5592 mmol) phthalic anhydride, 466 mg (6.290 mmol) propionic acid and 9.97 mg (52.4 µmol) p-toluenesulfonic acid monohydrate were added to a Schlenk flask equipped with a magnetic stirrer. The reaction was carried out in a 160 °C thermostated oil bath for 24 h under nitrogen atmosphere and continuous stirring. The reaction was left to cool down, and the Schlenk flask was opened to the atmosphere. The products were dissolved in HFE-7100/THF/ethanol 10:2:1 (v/v/v) mixture, filtered and washed six times with 0.1 M HCl aqueous solution. The organic phase was dried over sodium sulfate and filtered. Organic solvents were evaporated on a rotary evaporator at 45 °C under reduced pressure. Silica gel column chromatography with gradient elution starting from MTBE/THF 10:1 (v/v) and slowly decreasing the MTBE portion reaching pure THF was used to obtain Rh-C_2H_4-$C_{10}F_{21}$ (l) as a red solid. The product was dissolved in a small quantity of acetone and precipitated into excess cold n-hexane, filtered using a Büchner funnel and dried under vacuum at RT to obtain Rh-C_2H_4-$C_{10}F_{21}$ (**l**) as a red solid with 20 % yield. ^{1}H NMR (500 MHz, THF-d_8) δ 7.90 (d, J = 7.6 Hz, 1H), 7.64 (td, J = 7.4, 1.1 Hz, 1H), 7.58 (td, J = 7.4, 0.7 Hz, 1H), 7.15 (d, J =

7.6 Hz, 1H), 6.48 (d, J = 8.6 Hz, 2H), 6.42 (d, J = 2.3 Hz, 2H), 6.29 (dd, J = 8.7, 2.3 Hz, 2H), 5.54 (t, J = 6.1 Hz, 2H), 3.56 – 3.49 (m, 4H), 2.64 – 2.35 (m, 4H). ^{19}F NMR (470 MHz, THF-d_8) δ - 79.95 (t, J = 10.0 Hz, 6F), -112.54 – -112.89 (m, 4F), -120.09 – -120.90 (m, 20F), -121.23 – - 121.62 (m, 4F), -121.94 – -122.35 (m, 4F), -124.78 – -125.13 (m, 4F). ESI-ToF, m/z: calculated for $C_{44}H_{21}F_{42}N_2O_3$ 1423.0876 [M]$^+$; found 1422.9367.
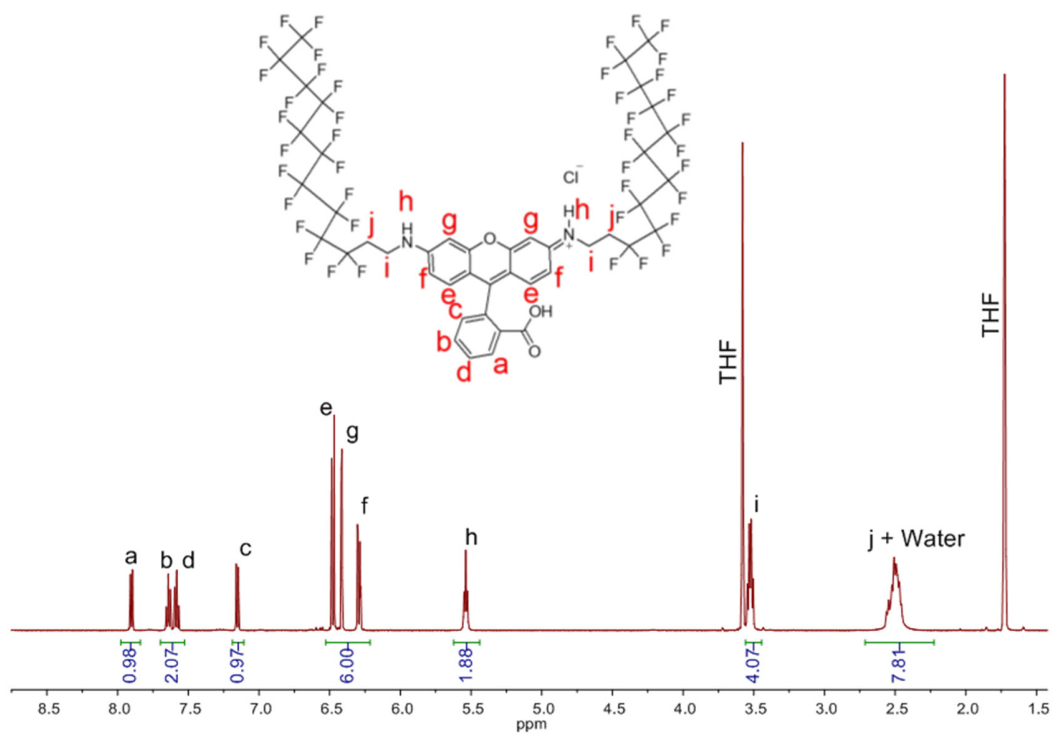
Fig. 2.10. ^{1}H NMR spectrum (500 MHz, THF-d_8) of Rh-C_2H_4-$C_{10}F_{21}$.
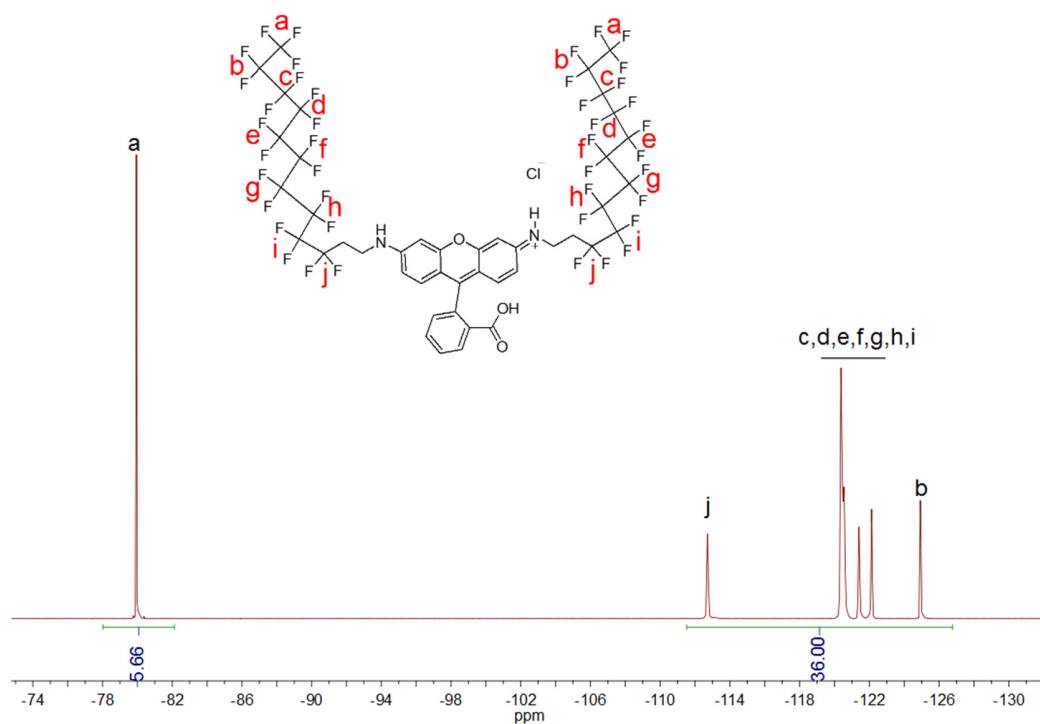
Fig. 2.11. ^{19}F NMR spectrum (470 MHz, THF-d_8) of Rh-C$_2$H$_4$-C$_{10}$F$_{21}$.
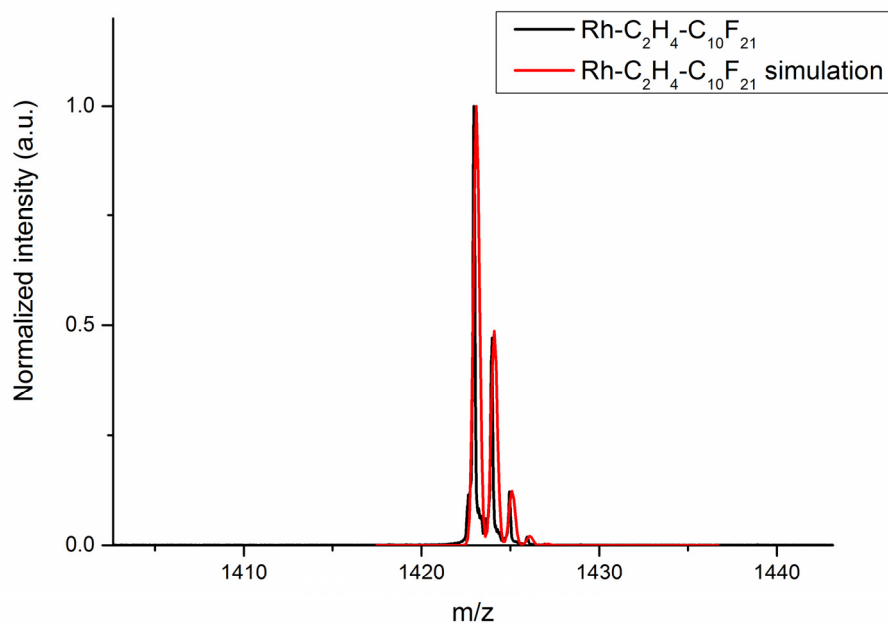
Fig. 2.12. Rh-C$_2$H$_4$-C$_{10}$F$_{21}$ ESI-ToF spectrum of a 30 μM TFE solution; m/z: 1422.9367 [M]$^+$; simulated m/z: 1423.0876 for C$_{44}$H$_{21}$F$_{42}$N$_2$O$_3$.

2.4 UV-Vis spectroscopy, fluorescence spectroscopy, and quantum yield characterization

Varian-Cary 4000 double beam UV-Vis spectrometer was used for UV-Vis measurements. BRAND® UV micro single-use cuvettes (mfr. no. BRAND® 7592 20) with center height 15 mm having a 1 cm path length were filled with 500 µL 2,2,2-trifluoroethanol (TFE) solutions. UV-Vis measurements were done with baseline correction (subtraction) at a temperature of 20 °C. Fluorescence was measured by a FluoroMax 2 spectrometer (Jobin-Yvon). 200 µL solutions were placed in a Hellma SUPRASIL® cuvette (105.250-QS) with center height 15 mm. For fluorescence emission spectra, $\lambda_{abs,max}$ was used to excite the corresponding F-rhodamines. Rh-CH_2-C_3F_7 and Rh-CH_2-C_7F_{15} were excited at 490 and 491 nm, respectively, whereas Rh-C_2H_4-C_8F_{17} and Rh-C_2H_4-$C_{10}F_{21}$ were excited at 504 nm. The calibration of the FluoroMax 2 spectrometer was checked with the water Raman peak at 397 nm before and after the measurement of each sample. All fluorescence measurements were done at 20 °C. Emission spectra were recorded with 0.5 nm increments, 0.1 s integration time, and 2 nm excitation and emission slits. The emission spectra were recorded as counts per second (cps) as a function of the wavelength (nm) using S/R (signal/reference) detection mode to compensate the aging effect of the xenon lamp.

The absorbance *f* of the four dyes was measured as a function of concentration in the dilute regime where the Lambert-Beer law is obeyed (less than 3 µM in 2,2,2-trifluoroethanol (TFE) at an absorbance less than 0.1. Thus, all UV-Vis and fluorescence measurements were done at concentrations less than 2 µM (equivalent to an absorption of less than 0.1) to be safely within the linear regime. Quantum yields of the F-rhodamines Φ_x were calculated relative to a standard (fluorescein in 0.1 M NaOH aqueous solution with a quantum yield of Φ_{st} = 0.89) based on a protocol published by Würth et al. [20]. Absorbance *f* and emission flux *F* were measured at 490 and 491 nm for Rh-CH_2-C_3F_7 and Rh-CH_2-C_7F_{15}, respectively. The quantum yields of Rh-C_2H_4-C_8F_{17} and Rh-C_2H_4-$C_{10}F_{21}$ were determined at 496 nm. Eq. 2.1 was used to calculate the relative quantum yields of the synthesized F-rhodamines.

$$\Phi_x = \Phi_{st} \cdot \frac{F_x}{F_{st}} \cdot \frac{f_{st}}{f_x} \cdot \frac{n_x^2(sodium\ line)}{n_{st}^2(sodium\ line)} \qquad \textbf{2.1}$$

The subscript *x* refers to the values of the F-rhodamines and *st* to the values of the fluorescein standards. The refractive indices of TFE and 0.1 M NaOH aqueous solution were used for the F-rhodamine solutions and the fluorescein standards respectively. The quantum yields of the synthesized F-rhodamines are given in Table 2.1.

2.5 Results and discussion

The absorption spectra of the F-rhodamines in TFE at 20 °C at different concentrations are given in Fig. 2.13 to 2.16. Fig. 2.17 shows the absorbance maxima against different concentrations of the F-rhodamines in TFE at 20 °C and Fig. 2.18 to 2.21 show the emission spectra of the F-rhodamines excited with their corresponding $\lambda_{max,abs}$ in TFE at 20 °C. Fig. 2.22 presents the fluorescence emission area (integral) against different concentrations of the F-rhodamines in TFE at 20 °C and Fig. 2.23 and 2.24 illustrate the normalized absorption and emission spectra of 1 µM solutions of the F-rhodamines in TFE at 20 °C respectively.
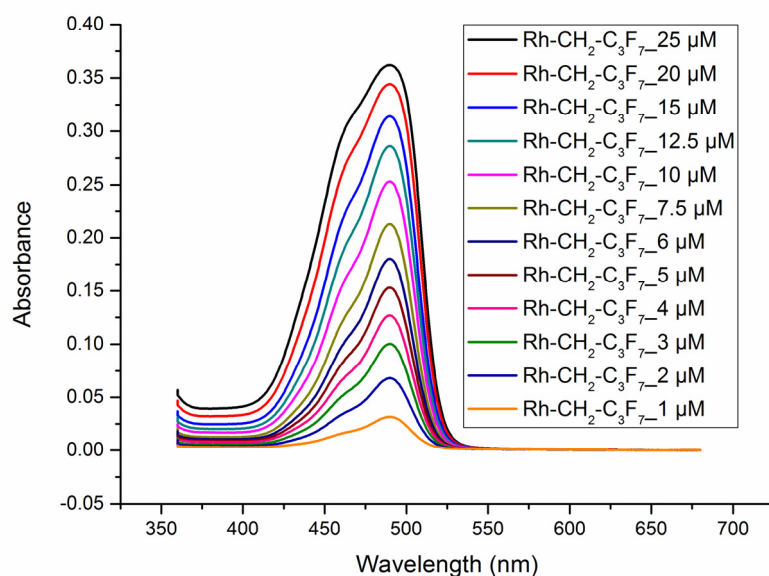
Fig. 2.13. Rh-CH$_2$-C$_3$F$_7$ (**d**) absorption spectra in TFE at 20 °C at different concentrations.
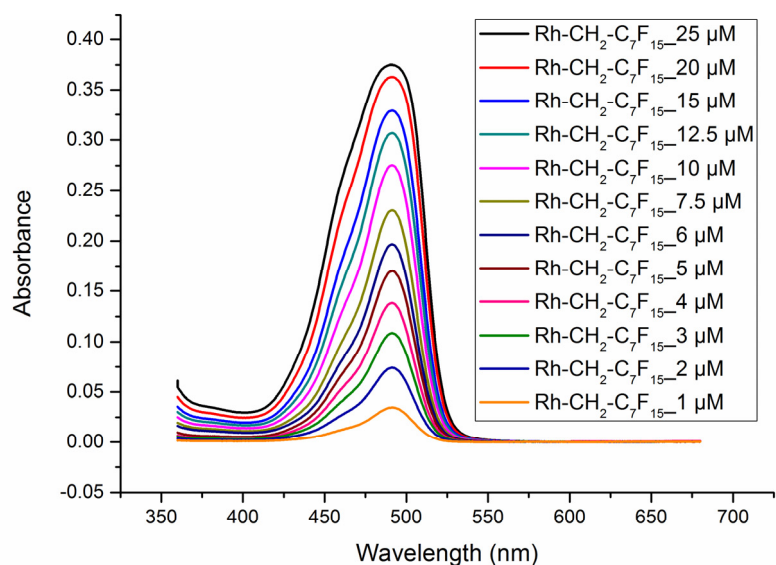
Fig. 2.14. Rh-CH$_2$-C$_7$F$_{15}$ (**h**) absorption spectra in TFE at 20 °C at different concentrations.
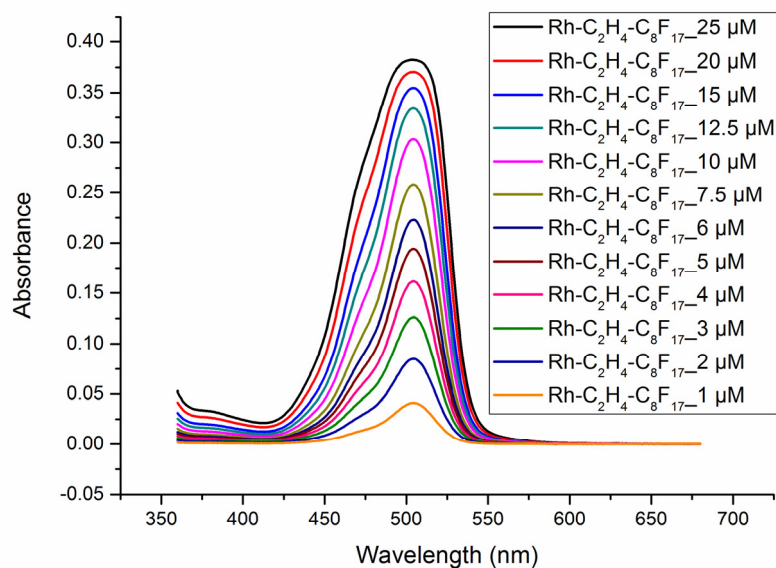
Fig. 2.15. Rh-C$_2$H$_4$-C$_8$F$_{17}$ (**k**) absorption spectra in TFE at 20 °C at different concentrations.
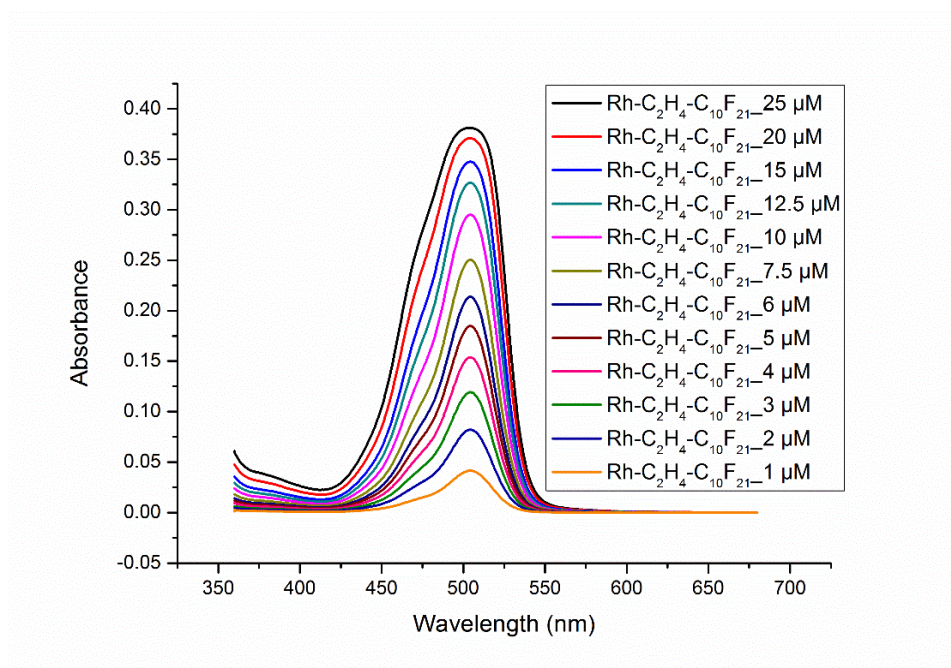
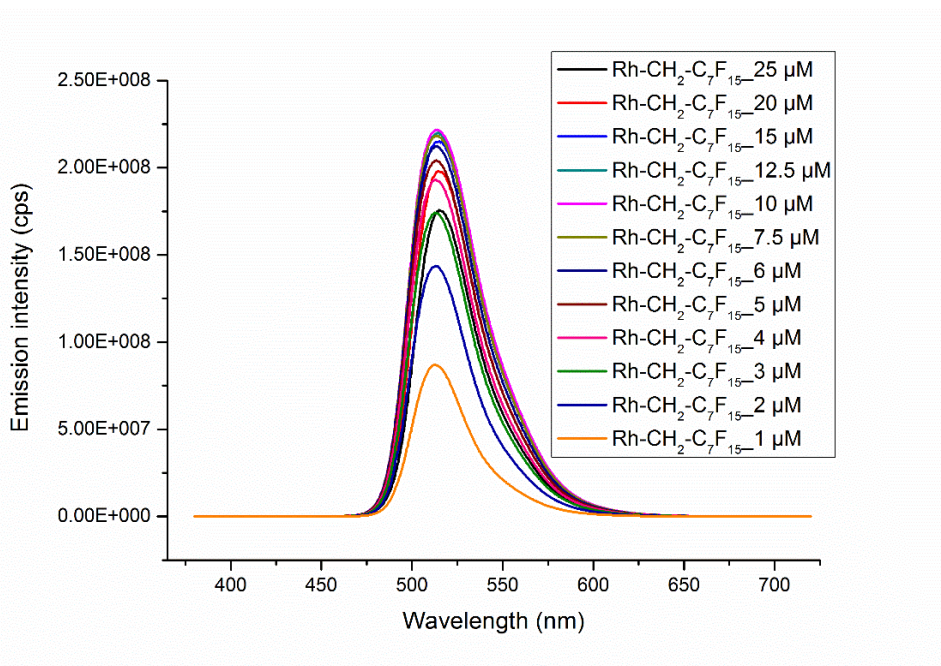**Fig. 2.16.** Rh-C_2H_4-$C_{10}F_{21}$ (**I**) absorption spectra in TFE at 20 °C at different concentrations.
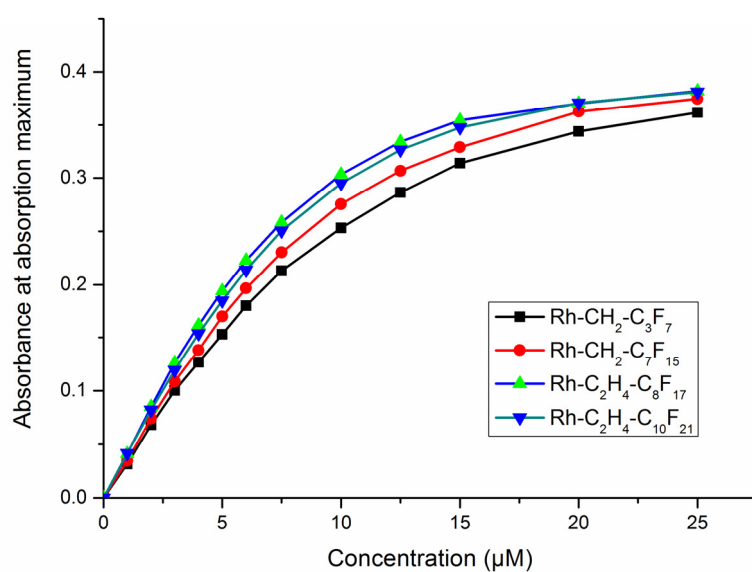
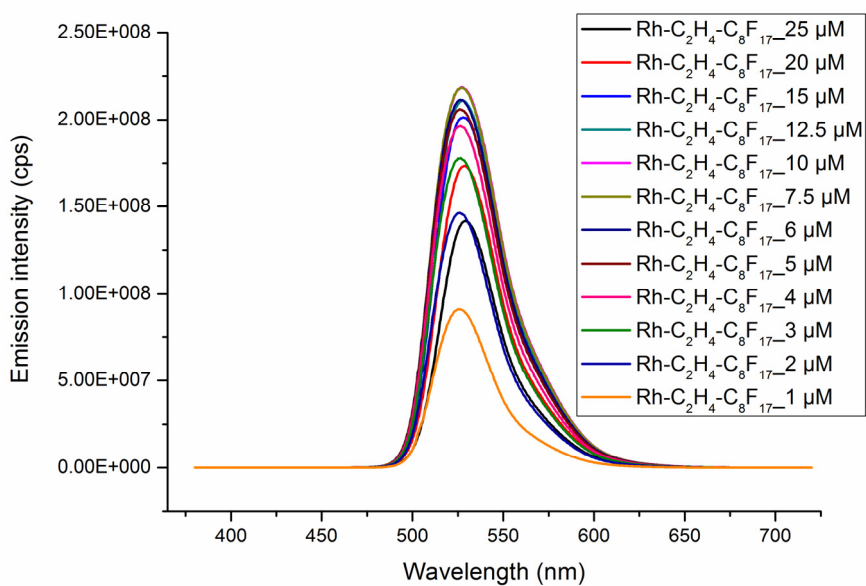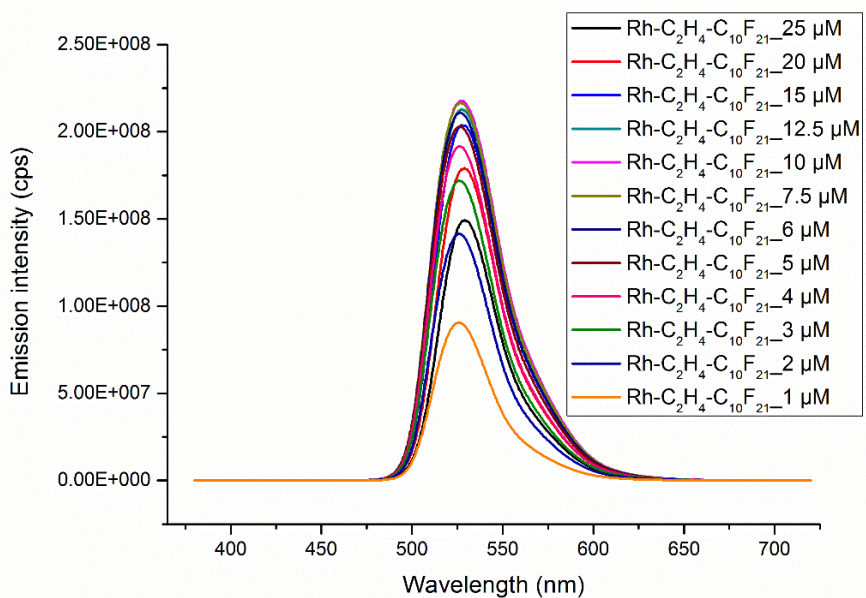**Fig. 2.17.** Absorbance at absorption maxima against concentrations for fluorinated rhodamines in TFE at 20 °C.
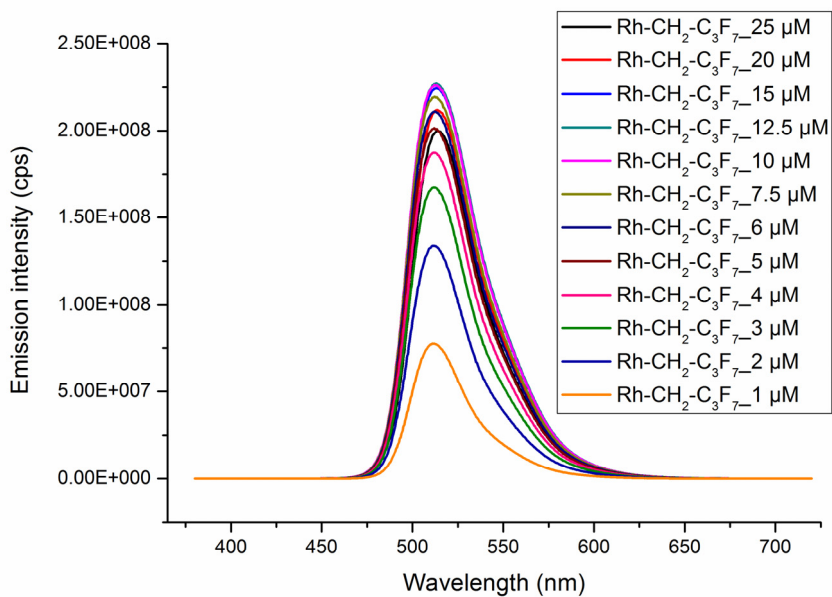
Fig. 2.18. Rh-CH$_2$-C$_3$F$_7$ (**d**) emission spectra in TFE at 20 °C at different concentrations (λ_{ex} = 490 nm).

Fig. 2.19. Rh-CH$_2$-C$_7$F$_{15}$ (**h**) emission spectra in TFE at 20 °C at different concentrations (λ_{ex} = 491 nm).

Fig. 2.20. Rh-C_2H_4-C_8F_{17} (**k**) emission spectra in TFE at 20 °C at different concentrations (λ_{ex} = 504 nm).

Fig. 2.21. Rh-C_2H_4-$C_{10}F_{21}$ (**l**) emission spectra in TFE at 20 °C at different concentrations (λ_{ex} = 504 nm).
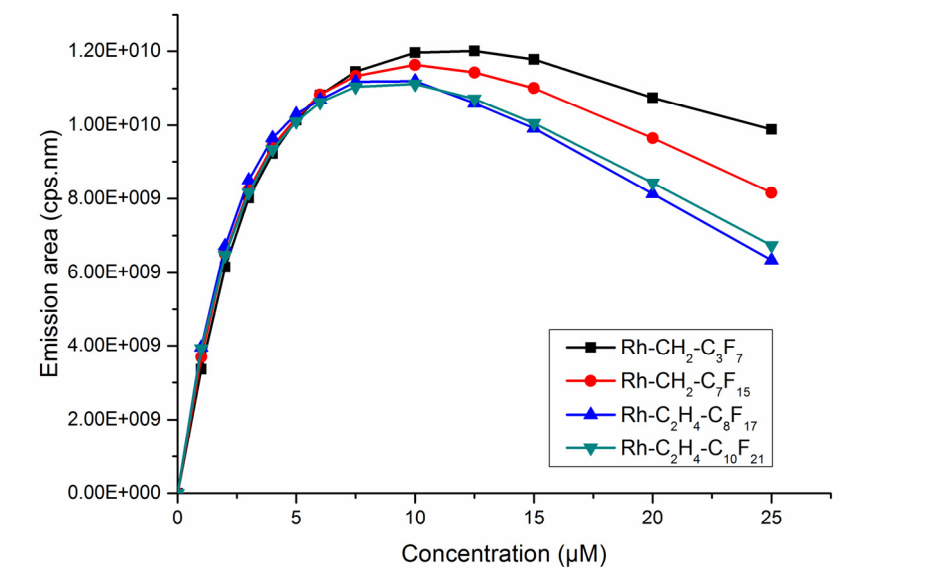
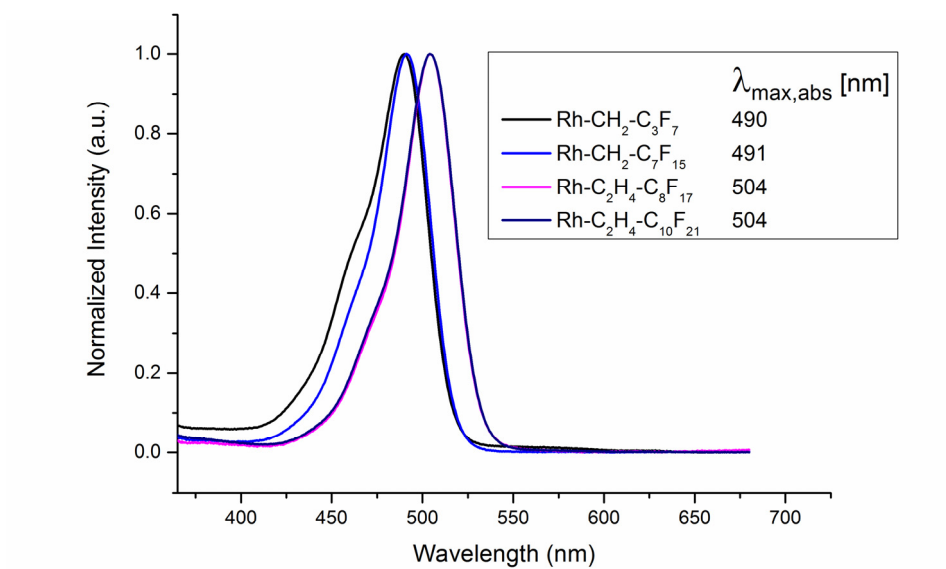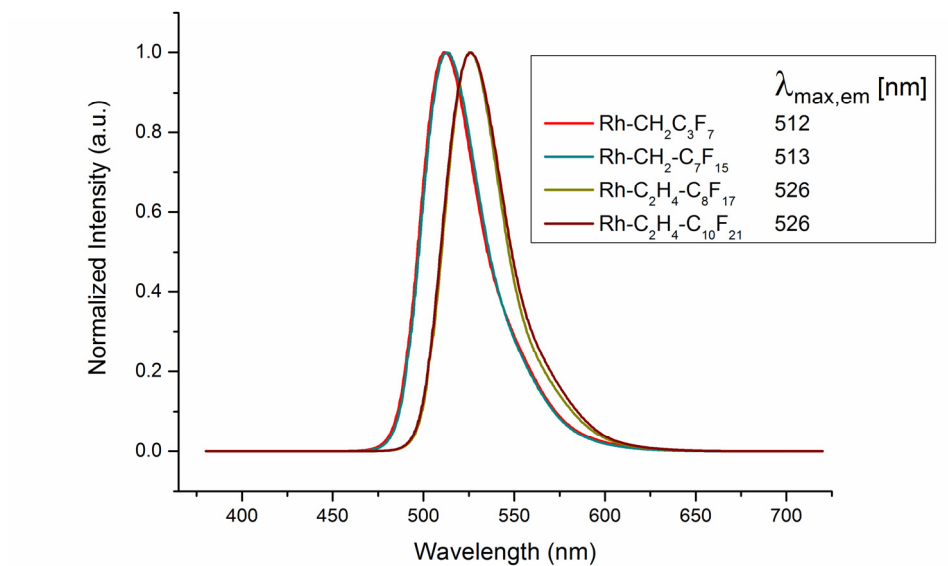**Fig. 2.22.** Emission area (integral) against concentration for fluorinated rhodamines in TFE at 20 °C.
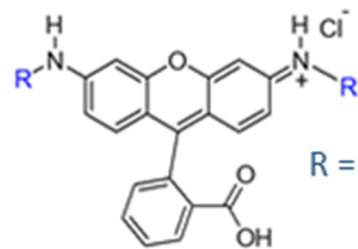

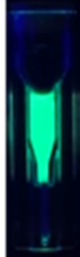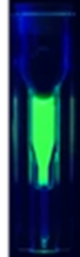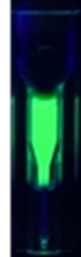**Fig. 2.23.** Normalized absorption spectra of 1 μM F-rhodamines in TFE at 20 °C.

Fig. 2.24. Normalized emission spectra of 1 μM F-rhodamines in TFE at 20 °C.

Table 2.1. Quantum yield (Φ), absorption and emission maxima (λ_{max}(abs) and λ_{max}(em)), molar absorptivity (ε) of the synthesized F-rhodamines.

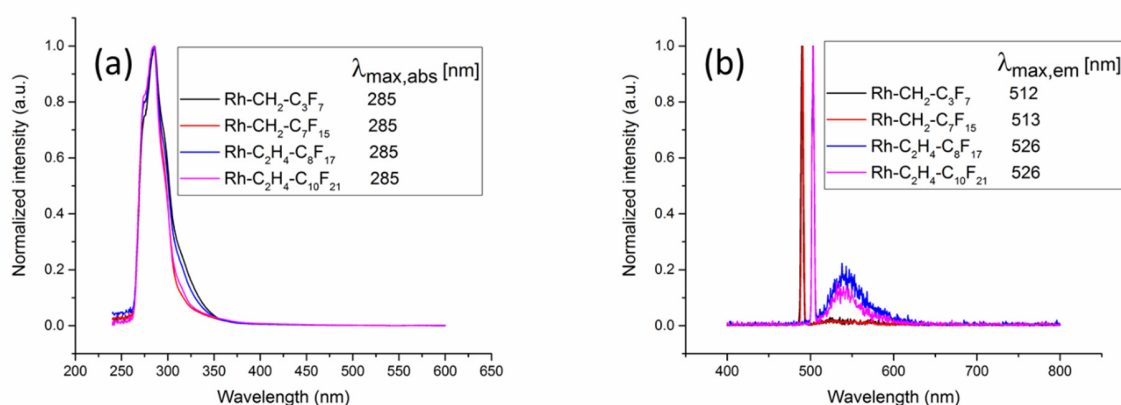|	CH_2-C_3F_7	CH_2-C_7F_{15}	C_2H_4-C_8F_{17}	C_2H_4-$C_{10}F_{21}$
Φ^a	0.91	0.93	0.88	0.87
λ_{max}(abs) [nm]^b	490	491	504	504
λ_{max}(em) [nm]^b	512	513	526	526
ε [M^{-1}cm^{-1}]^c	33450	36340	42130	40250

^{a}Quantum yield measured in 2,2,2-trifluoroethanol (TFE) at 20 °C using 0.1 M NaOH aqueous fluorescein solution as reference. ^{b}Obtained from absorption and emission (fluorescence) spectra in TFE at 20 °C. ^{c}Molar absorptivity calculated in TFE at 20 °C.

Four rhodamine-based fluorescence dyes bearing perfluorinated ponytails on their amine groups were synthesized and characterized by solution NMR spectroscopy and ESI-ToF mass spectrometry. One methylene spacer separates the amine group from the C_3F_7 and C_7F_{15} perfluorinated ponytails for (**d**) and (**h**), whereas two methylene groups separate the amine group from the C_8F_{17} and $C_{10}F_{21}$ perfluorinated ponytails for (**k**) and (**l**) respectively. UV-Vis and fluorescence emission spectroscopy measurements were done in TFE where the corresponding dyes have a bright fluorescence and possess high quantum yields. Quantum yields (Φ), absorption maxima ($\lambda_{max,abs}$), emission maxima ($\lambda_{max,em}$), and the molar extinction coefficients (ε) are summarized in Table 2.1.
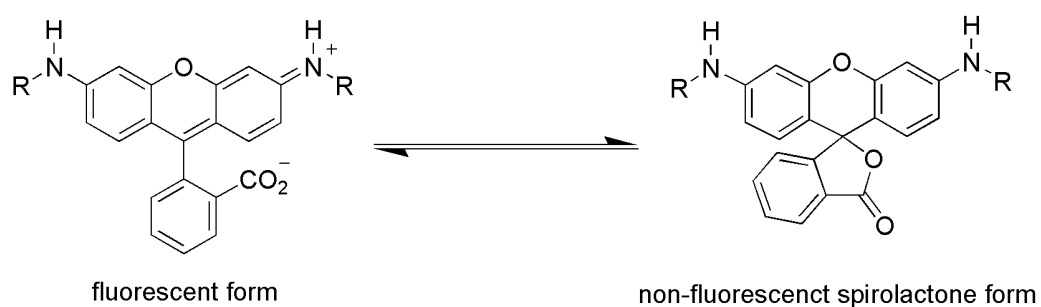
Rhodamine based fluorescence dyes were synthesized since they are photostable and show high resistance to bleaching which makes them useful as fluorescence microscopy probes for instance in CLSM. Rhodamine fluorescence dyes are highly fluorescent in polar protic media such as alcohols, but when dissolved in aprotic solvents such as THF or toluene they yield colorless solutions, the 400-500 nm absorption band present in protic media disappears, and another absorption maximum at approximately 285 nm appears as seen in Fig. 2.25 and 2.26. The fluorescence is practically switched-off in aprotic media as shown in Fig. 2.25b and Fig. 2.26b from the Rayleigh scattering peaks observed at the excitation wavelengths indicating negligible fluorescence emission. The characteristic blue-shift in the absorption band is due to the spirolactone "closed form" conformation adopted by rhodamine dyes in aprotic media as seen in Scheme 2.2 [145,202].

Fig. 2.25. Normalized absorption (a) and emission (b) spectra of 1μM THF solutions of the four synthesized F-rhodamines at 20 °C. Rh-CH$_2$-C$_3$F$_7$ and Rh-CH$_2$-C$_7$F$_{15}$ were excited at 490 and 491 nm respectively; Rh-C$_2$H$_4$-C$_8$F$_{17}$ and Rh-C$_2$H$_4$-C$_{10}$F$_{21}$ were both excited at 504 nm.
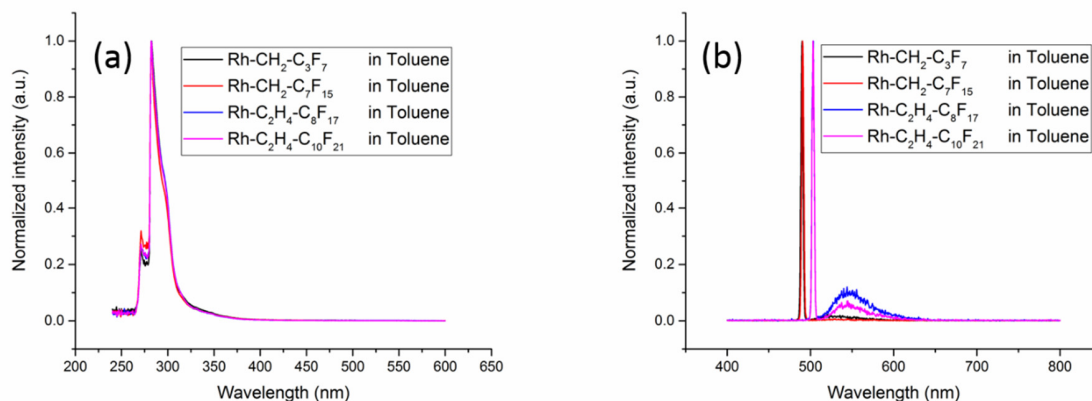
Fig. 2.26. Normalized absorption (a) and emission (b) spectra of 1μM toluene solutions of the four synthesized F-rhodamines at 20 °C. Rh-CH$_2$-C$_3$F$_7$ and Rh-CH$_2$-C$_7$F$_{15}$ were excited at 490 and 491 nm respectively; Rh-C$_2$H$_4$-C$_8$F$_{17}$ and Rh-C$_2$H$_4$-C$_{10}$F$_{21}$ were both excited at 504 nm.

fluorescent form   non-fluorescenct spirolactone form

Scheme 2.2. The equilibrium between the open fluorescent and the closed non-fluorescent "spirolactone" forms of rhodamine-based fluorescence dyes.

After the synthesis and characterization, the F-rhodamine dyes should be investigated to determine if they exhibit some affinity to fluorophilic phases. The fluorophilic character of the F-rhodamines will be discussed in more detail in sections 3, 4, and 5.

3 Langmuir monolayer isotherms coupled with epifluorescence microscopy at the air-water interface

3.1 Motivation

Langmuir monolayer investigations on the air-water interface using surface pressure (π)-area (A) isotherms, i.e. plotting the change in surface pressure as a function of the area available per molecule on an aqueous surface, yield mainly information about monolayer phases, compressibility, and stability. Coupling the π-A isotherms with epifluorescence microscopy on the air-water interface provides extra information about domain formation, shape, and domain coexistence [192]. In epifluorescence microscopy, fluorescence probes are used to give a contrast between dye-enriched "bright" and dye-depleted "dark" domains which is realized by using fluorescent dyes with preferential affinity to one or several domains. As an example, rhodamine-DPPE partitions preferentially into the liquid expanded (LE) domains of DPPC making them look "bright" and is excluded from the liquid condensed (LC) "dark" domains [199,200]. Long-chain perfluorinated and aliphatic carboxylic acids such as perfluorostearic acid (FC18) and stearic acid (SA) form phase separated monolayers at room temperature [203]. The Rh-C_2H_4-$C_{10}F_{21}$ (F-rhodamine bearing the longest perfluorinated chain) and the Rh-CH_2-C_3F_7 (F-rhodamine bearing the shortest perfluorinated chain) were tested with FC18 and SA mixed monolayers changing systematically the FC18 to SA molar ratio in an attempt to check the difference in the affinity of the dyes to fluorophilic and lipophilic domains. It is expected that the Rh-C_2H_4-$C_{10}F_{21}$ shows a higher affinity to fluorophilic domains compared to the less fluorinated Rh-CH_2-C_3F_7 dye.

3.2 Experimental part

As discussed in section 2, four fluorinated rhodamine-based fluorescence dyes were synthesized having different fluorinated ponytail and spacer lengths. To probe the fluorophilic character of the dyes, we used mixed Langmuir monolayers of FC18 and SA which are immiscible. The ratios of the two components were systematically changed from pure FC18 to pure SA. The fluorescence dyes Rh-C_2H_4-$C_{10}F_{21}$ and Rh-CH_2-C_3F_7, having the longest and shortest perfluorinated ponytails respectively, were added with a concentration of 0.1 mol % as probes and the results are discussed in this chapter. The FC18 was dissolved into a premixed diethyl ether/nonafluorobutyl methyl ether 1:1 (v/v) solution, and the SA was dissolved in chloroform. The pure monolayers were realized by

spreading the FC18 or SA solutions on the water surface via a Hamilton micro syringe, whereas the mixed monolayers were prepared by premixing the organic solutions of FC18 and SA in the requested proportions and a homogeneous organic solution containing both components was spread on the water surface.
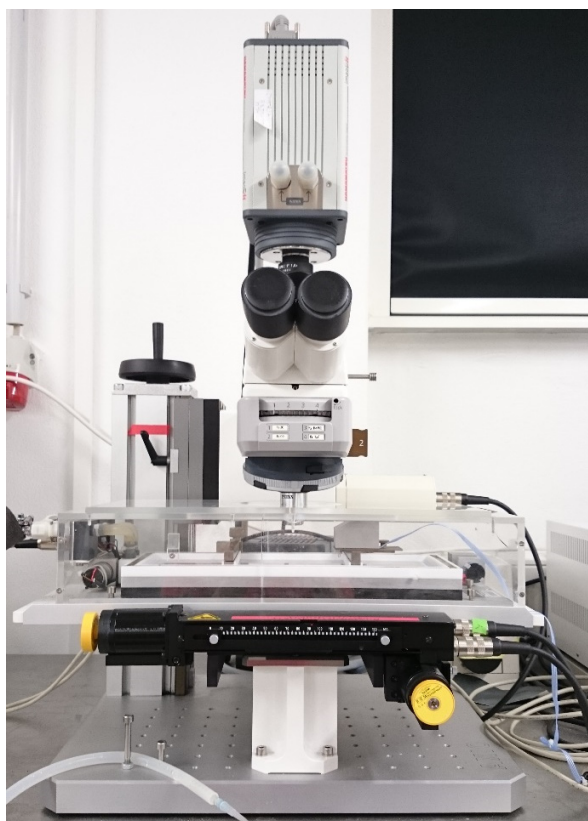

Fig. 3.1. Epifluorescence microscope coupled with a Langmuir trough.

3.3 Results and discussion

Fig. 3.2 displays the chemical structures of both F-rhodamines used in the epifluorescence experiments and Fig. 3.3 shows the π-A isotherms of the five different monolayer compositions ranging from pure FC18 to pure SA with 0.1 mol % Rh-C$_2$H$_4$-C$_{10}$F$_{21}$ dye which are very similar to the π-A isotherms obtained when using 0.1 mol % of Rh-CH$_2$-C$_3$F$_7$ dye as shown in Fig. 3.4, 3.6, 3.8, 3.10, and 3.12. It is clear that the FC18 isotherm shows an increase in surface pressure at higher molecular areas than stearic acid due to the larger cross-sectional area of 27-30 Å^2 for perfluorinated chains in comparison with 18-21 Å^2 for the aliphatic ones [198,208,209]. As the mole fraction of stearic acid increases, the lift-off is shifted systematically to a smaller mean

molecular area (approx. 46 Å^2/molecule for pure FC18 and 23 Å^2/molecule for pure SA) due to the reduced space requirements of the alkyl chains.
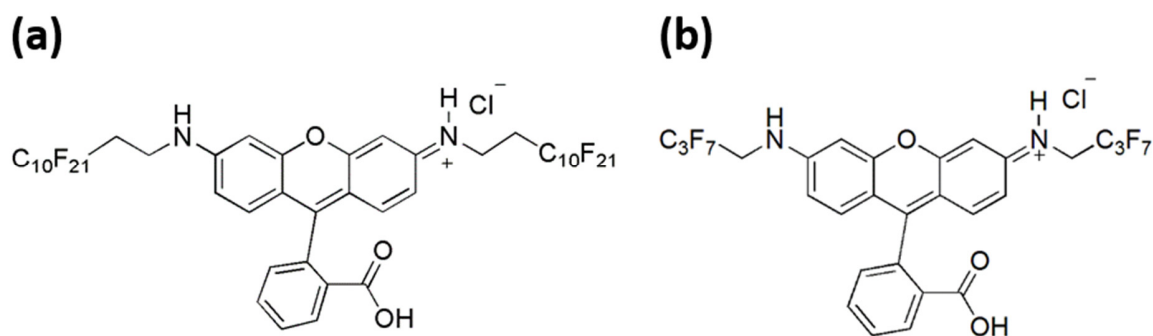
Fig. 3.2. Rh-C$_2$H$_4$-C$_{10}$F$_{21}$ **(a)** and Rh-CH$_2$-C$_3$F$_7$ **(b)** chemical structures.
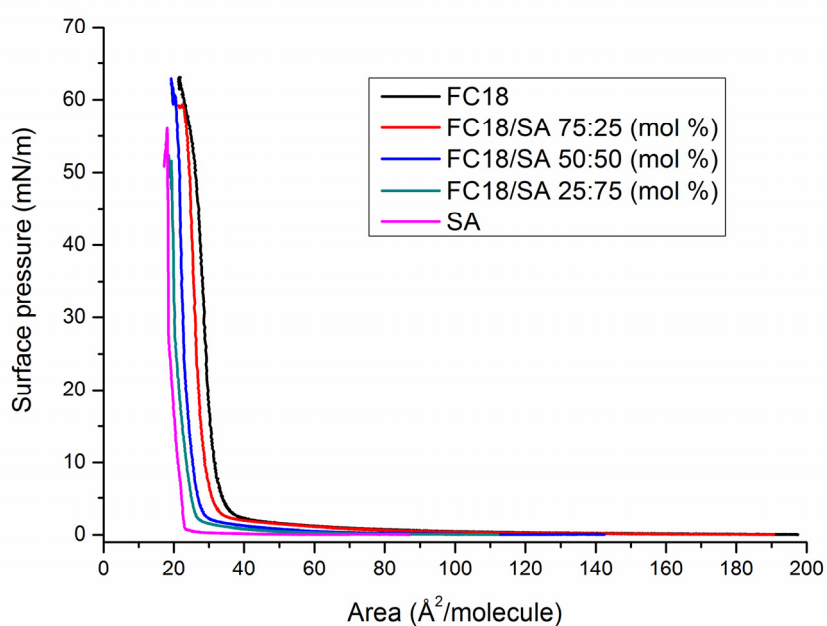
Fig. 3.3. Langmuir isotherms of FC18 and SA mixed monolayers on the water surface at 20 °C with 0.1 mol % Rh-C$_2$H$_4$-C$_{10}$F$_{21}$ dye.
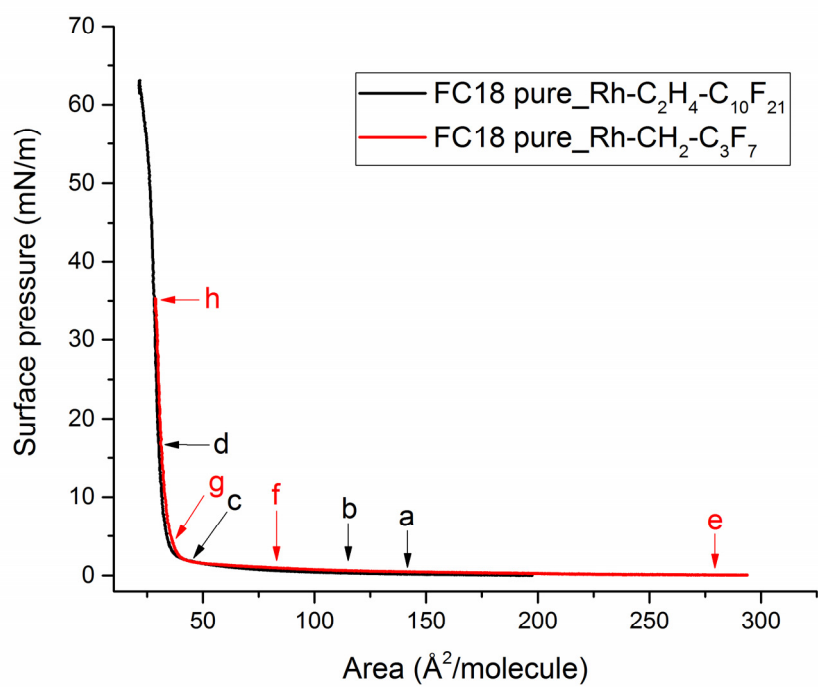
Fig. 3.4. Langmuir isotherm of FC18 monolayer on the water surface at 20 °C with 0.1 mol % Rh-C_2H_4-$C_{10}F_{21}$ (black isotherm) and Rh-CH_2-C_3F_7 (red isotherm).
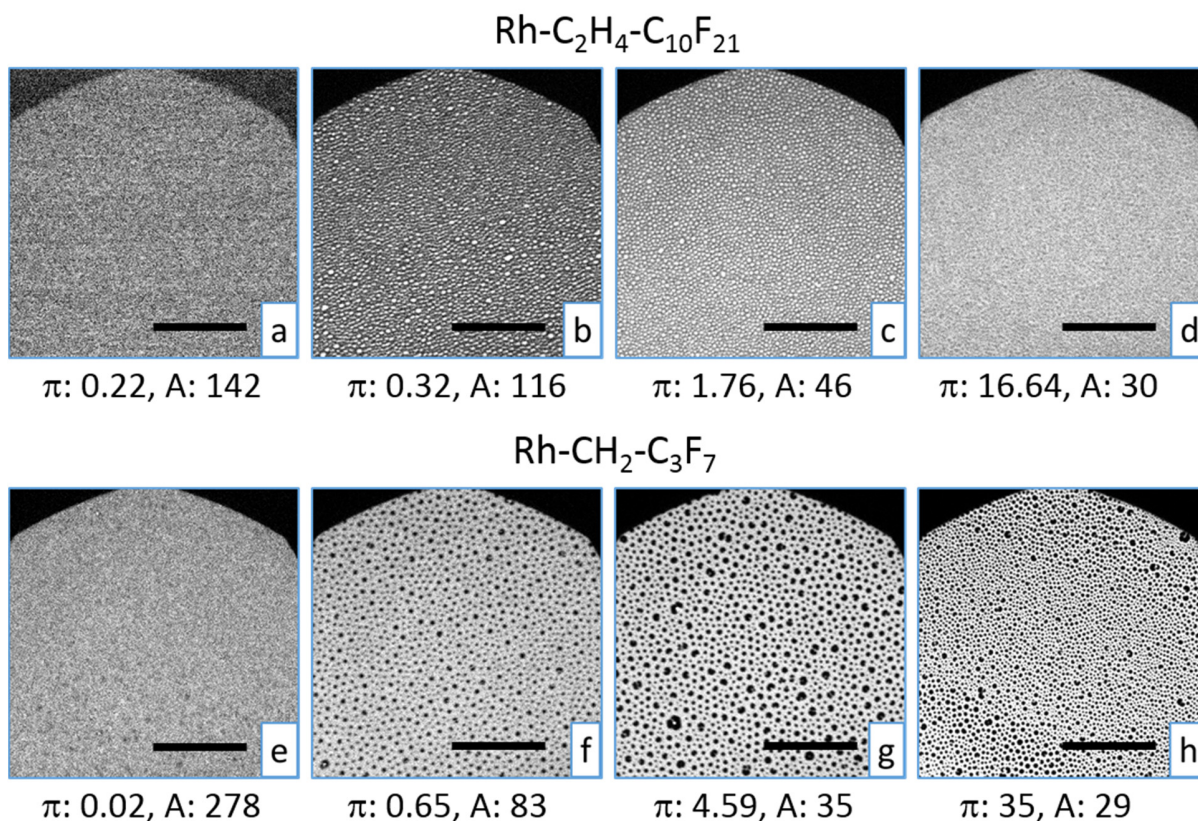
Fig. 3.5. Epifluorescence images of FC18 monolayer with 0.1 mol % Rh-C$_2$H$_4$-C$_{10}$F$_{21}$ dye (a-d) and 0.1 mol % Rh-CH$_2$-C$_3$F$_7$ dye (e-h). Scale bars: 50 μm. [π]: mN/m and [A]: Å^2/molecule.

Firstly, the fluorinated rhodamines bearing the longest (Rh-C$_2$H$_4$-C$_{10}$F$_{21}$) and shortest (Rh-CH$_2$-C$_3$F$_7$) perfluorinated ponytails were investigated with pure FC18 monolayers as seen in Fig. 3.4 and 3.5. Fig. 3.5a shows a homogeneous distribution, within the resolution limit of the epifluorescence microscope, of the Rh-C$_2$H$_4$-C$_{10}$F$_{21}$ dye at large areas and low surface pressures similar to the Rh-CH$_2$-C$_3$F$_7$ dye in Fig. 3.5e. Fig. 3.5b shows bright discontinuous domains dispersed in a darker continuous domain whereas Fig. 3.5f shows the opposite. From the comparison between Fig. 3.5b and f, it is obvious that Rh-C$_2$H$_4$-C$_{10}$F$_{21}$ partitions in the FC18 condensed discontinuous domains as they are being formed, whereas the Rh-CH$_2$-C$_3$F$_7$ is excluded from the FC18 condensed domains. Upon further compression, the Rh-C$_2$H$_4$-C$_{10}$F$_{21}$ is still present in the FC18 condensed discontinuous phase as seen in Fig. 3.5c up to a surface pressure of about 16.5 mN/m. Upon further compression, contrast inversion is observed, and the dye is excluded from the FC18 condensed phase as seen in Fig. 3.5d. On the other hand, the Rh-CH$_2$-C$_3$F$_7$ is

excluded from the FC18 condensed domains formation from the beginning as observed from Fig. 3.5f-h where the discontinuous domains are dark due to the exclusion of the $Rh-CH_2-C_3F_7$ from the beginning. The exclusion of the $Rh-C_2H_4-C_{10}F_{21}$ from the FC18 condensed phase at higher surface pressures as seen in Fig. 3.5d is due to the increase in the packing density and order due to the hexagonal packing of the fluorinated chains leading to the exclusion of the dye [193,194]. The isotherms of pure FC18 monolayers with $Rh-C_2H_4-C_{10}F_{21}$ and $Rh-CH_2-C_3F_7$ dyes look very similar as seen from Fig. 3.4 and show typical isotherms of monolayers formed from rigid rod-like amphiphiles such as FC18 [210,211].
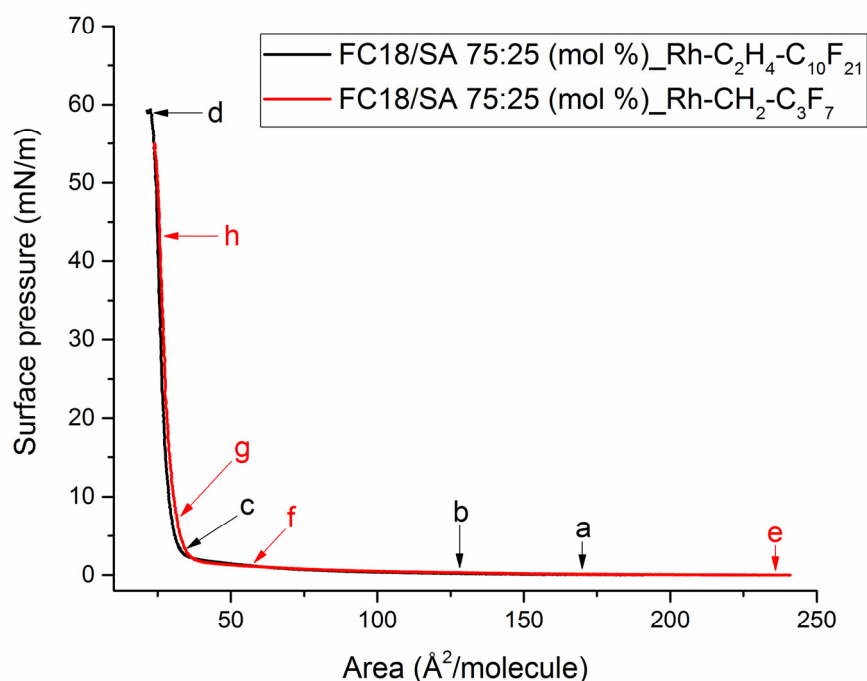
Fig. 3.6. Langmuir isotherm of FC18/SA 75:25 (mol %) mixed monolayer on the water surface at 20 °C with 0.1 mol % $Rh-C_2H_4-C_{10}F_{21}$ (black isotherm) and $Rh-CH_2-C_3F_7$ (red isotherm).
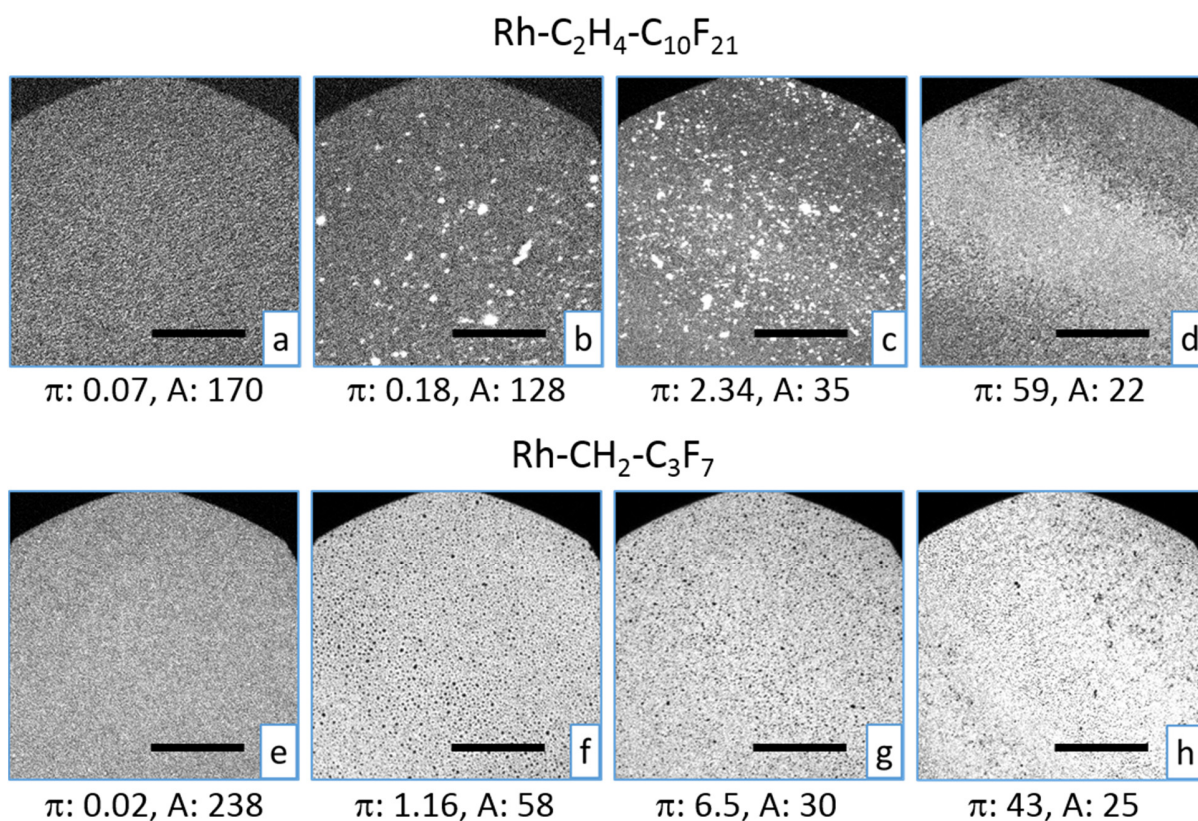
Fig. 3.7. Epifluorescence images of FC18/SA 75:25 (mol %) mixed monolayer with 0.1 mol % $Rh-C_2H_4-C_{10}F_{21}$ dye (a-d) and 0.1 mol % $Rh-CH_2-C_3F_7$ dye (e-h). Scale bars: 50 μm. [π]: mN/m and [A]: $Å^2$/molecule.

Fig. 3.7a shows a non-homogeneous $Rh-C_2H_4-C_{10}F_{21}$ partitioning similar to Fig. 3.7e for the $Rh-CH_2-C_3F_7$ dye for the FC18/SA 75:25 (mol %) mixed monolayer. Upon compression, it becomes clearer that the $Rh-C_2H_4-C_{10}F_{21}$ partitions favorably into discontinuous domains with different geometries as seen in Fig. 3.7b. The $Rh-CH_2-C_3F_7$ shows at least three different domains upon compression as shown in Fig. 3.7f: circular discontinuous dye depleted dark domains, circular discontinuous slightly brighter domains which indicate the presence of minute quantities of fluorescence dye, and a bright continuous phase where the $Rh-CH_2-C_3F_7$ is mostly partitioned. Little change is observed upon further compression for both dyes as seen from Fig. 3.7c and d and Fig. 3.7g and h. Both dyes show different physical properties, but at least for the FC18/SA 75:25 mol % monolayer composition they do not display a good contrast between what seems to be like FC18 rich condensed phases (dark domains in Fig. 3.7f and g) and SA rich condensed phases (slightly brighter domains in Fig. 3.7f and g).
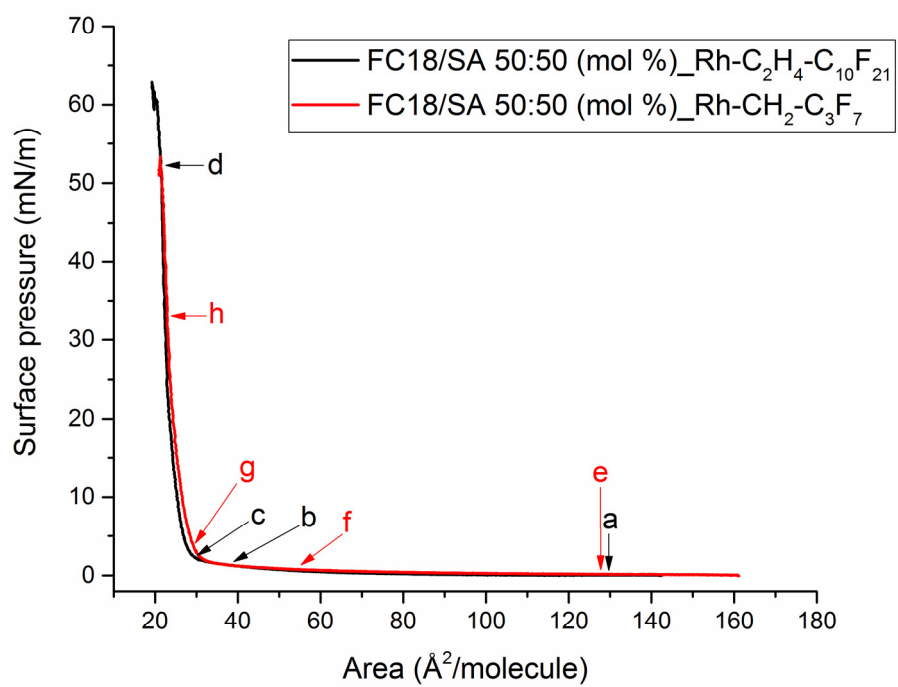
Fig. 3.8. Langmuir isotherm of FC18/SA 50:50 (mol %) mixed monolayer on the water surface at 20 °C with 0.1 mol % Rh-C_2H_4-$C_{10}F_{21}$ (black isotherm) and Rh-CH_2-C_3F_7 (red isotherm).
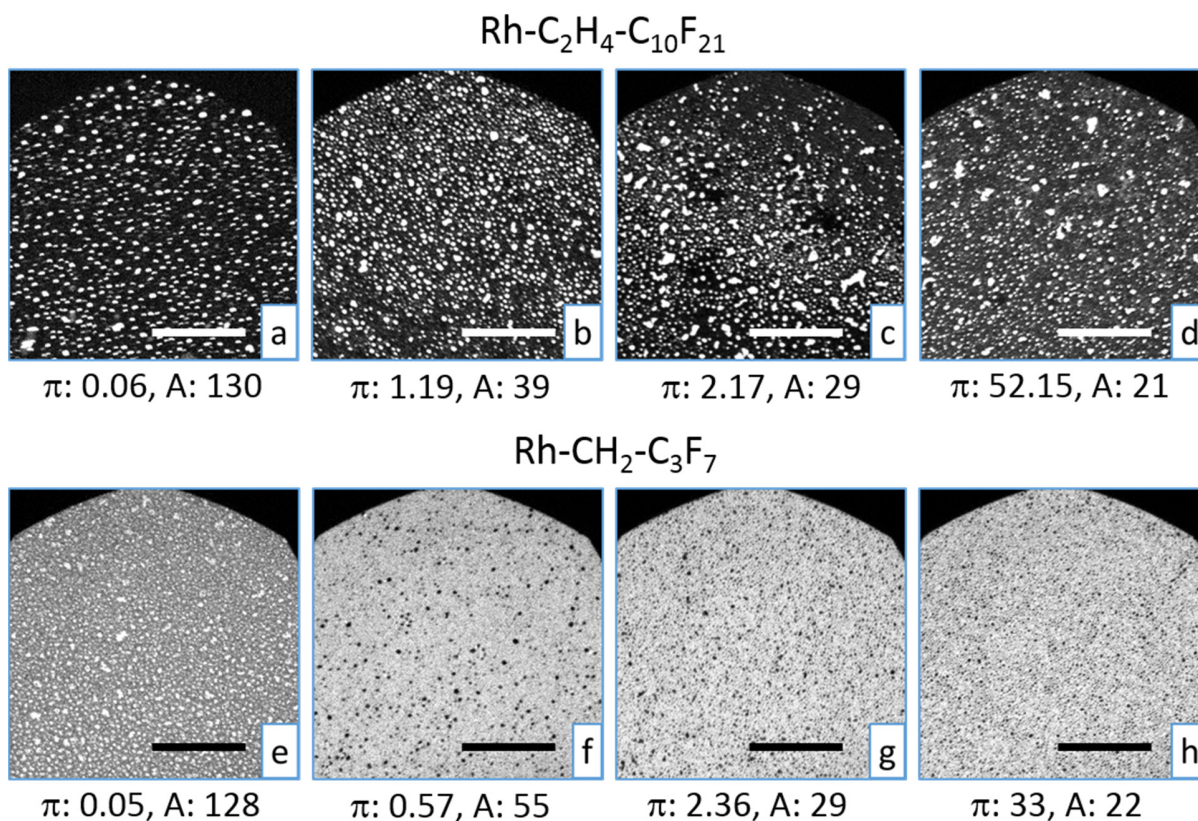
Fig. 3.9. Epifluorescence images of FC18/SA 50:50 (mol %) mixed monolayer with 0.1 mol % $Rh-C_2H_4-C_{10}F_{21}$ dye (a-d) and 0.1 mol % $Rh-CH_2-C_3F_7$ dye (e-h). Scale bars: 50 μm. [π]: mN/m and [A]: Å^2/molecule.

Fluorescence dye rich and poor domains were already visible from the start at low surface pressures and large areas as seen in Fig. 3.9a and e. Both dyes partition at low surface pressures more favorably into discontinuous domains, but the $Rh-C_2H_4-C_{10}F_{21}$ shows a stronger contrast in comparison to the $Rh-CH_2-C_3F_7$ between the discontinuous and continuous domains. Due to the larger cross-sectional area of the perfluorinated chain in comparison to aliphatic chains, the discontinuous condensed domains should be FC18 rich. This rational is favored by the superior contrast for the $Rh-C_2H_4-C_{10}F_{21}$ over the $Rh-CH_2-C_3F_7$ due to the former dye bearing a longer perfluorinated ponytail rendering it more fluorophilic than the latter one. Upon further compression, no big differences are observed for the $Rh-C_2H_4-C_{10}F_{21}$ as seen from Fig. 3.9b-d. $Rh-CH_2-C_3F_7$ shows upon compression a similar behavior to the previous FC18/SA 75:25 mol % experiment with the observation of three different domains as seen from Fig. 3.9f-h.
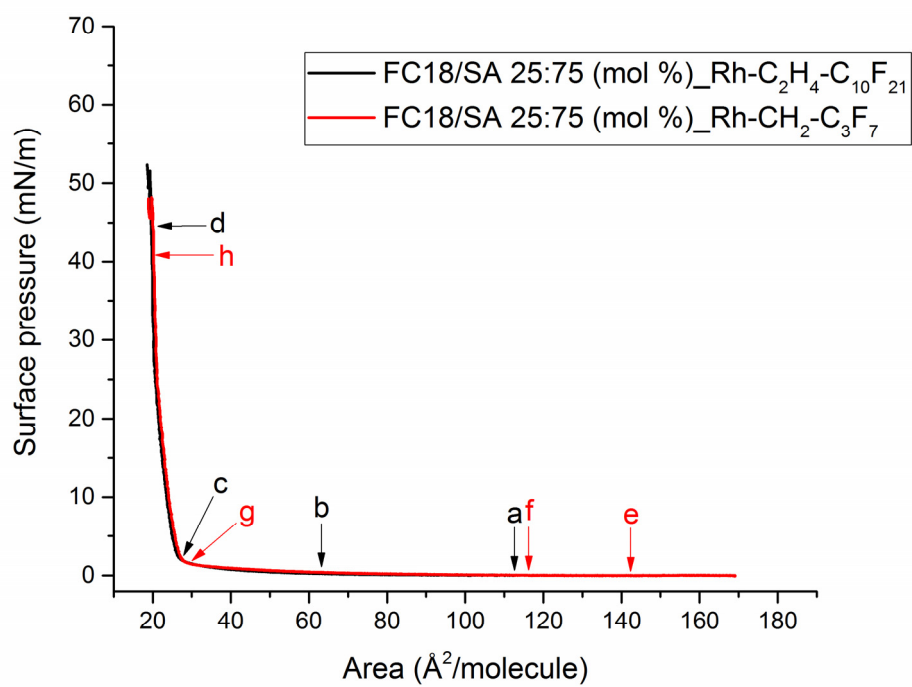
Fig. 3.10. Langmuir isotherm of FC18/SA 25:75 (mol %) mixed monolayer on the water surface at 20 °C with 0.1 mol % Rh-C_2H_4-$C_{10}F_{21}$ (black isotherm) and Rh-CH_2-C_3F_7 (red isotherm).
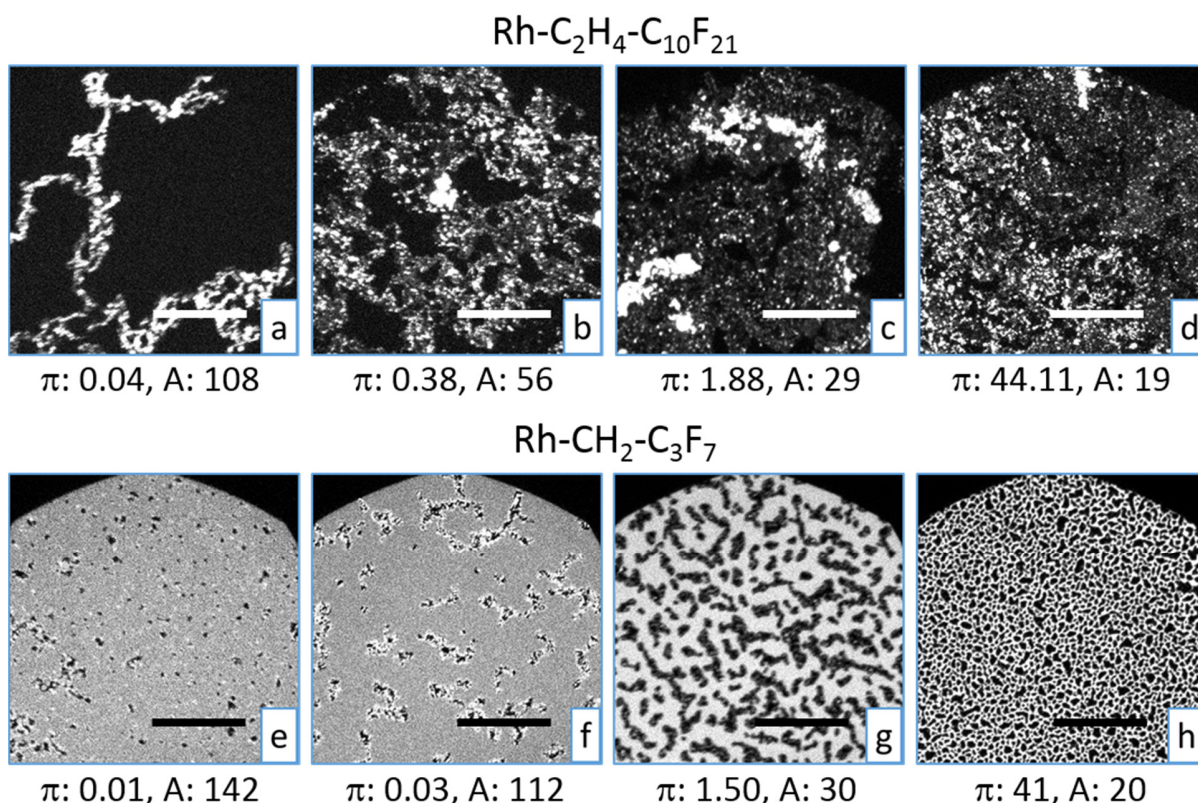
Rh-C$_2$H$_4$-C$_{10}$F$_{21}$

π: 0.04, A: 108	π: 0.38, A: 56	π: 1.88, A: 29	π: 44.11, A: 19

Rh-CH$_2$-C$_3$F$_7$

π: 0.01, A: 142	π: 0.03, A: 112	π: 1.50, A: 30	π: 41, A: 20

Fig. 3.11. Epifluorescence images of FC18/SA 25:75 (mol %) mixed monolayer with 0.1 mol % Rh-C$_2$H$_4$-C$_{10}$F$_{21}$ dye (a-d) and 0.1 mol % Rh-CH$_2$-C$_3$F$_7$ dye (e-h). Scale bars: 50 μm. [π]: mN/m and [A]: Å^2/molecule.

The differences in physical properties between the Rh-C$_2$H$_4$-C$_{10}$F$_{21}$ and Rh-CH$_2$-C$_3$F$_7$ are also evident from the FC18/SA 25:75 mol % monolayer experiments as seen from Fig. 3.11. At low surface pressures, the Rh-C$_2$H$_4$-C$_{10}$F$_{21}$ is enriched in between dark and large domains as evident from Fig. 3.11a and upon further compression large dark islands and two other domains with different levels of brightness are observed from Fig. 3.11b. The three domains with different contrast stay visible upon further compression as seen from Fig. 3.11c and d. The partitioning behavior of Rh-CH$_2$-C$_3$F$_7$ is different where at low surface pressures it tends to concentrate mainly on the interface between dark discontinuous domains and a moderately bright continuous domain. As the surface pressure increases, the Rh-CH$_2$-C$_3$F$_7$ rich interface disappears, and a dark discontinuous phase within a dye rich bright continuous phase is observed as seen from Fig. 3.11g. Further compression leads to the growth of the dark discontinuous domains, and the dye remains partitioned in the continuous phase.
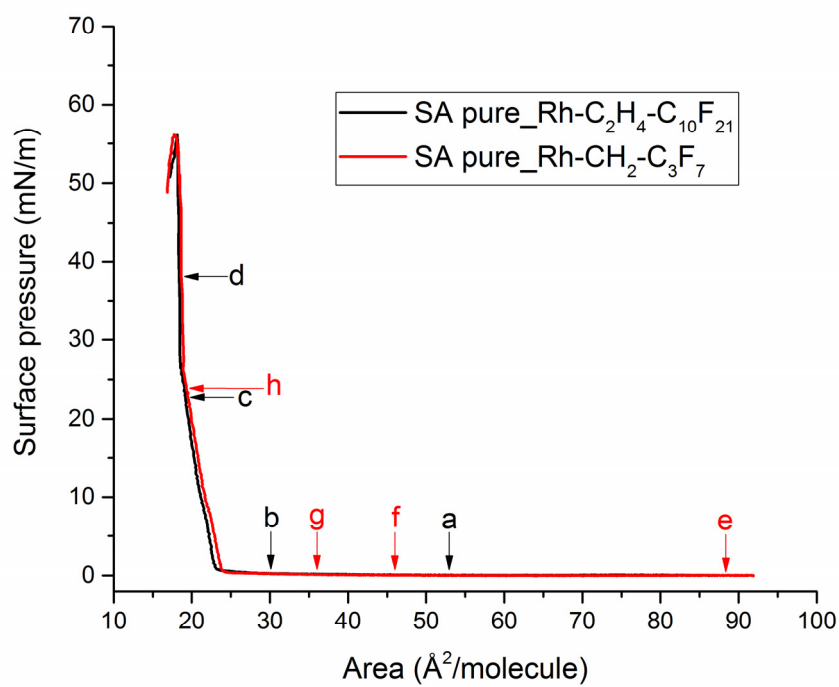
Fig. 3.12. Langmuir isotherm of SA monolayer on the water surface at 20 °C with 0.1 mol % Rh-C_2H_4-$C_{10}F_{21}$ (black isotherm) and Rh-CH_2-C_3F_7 (red isotherm).
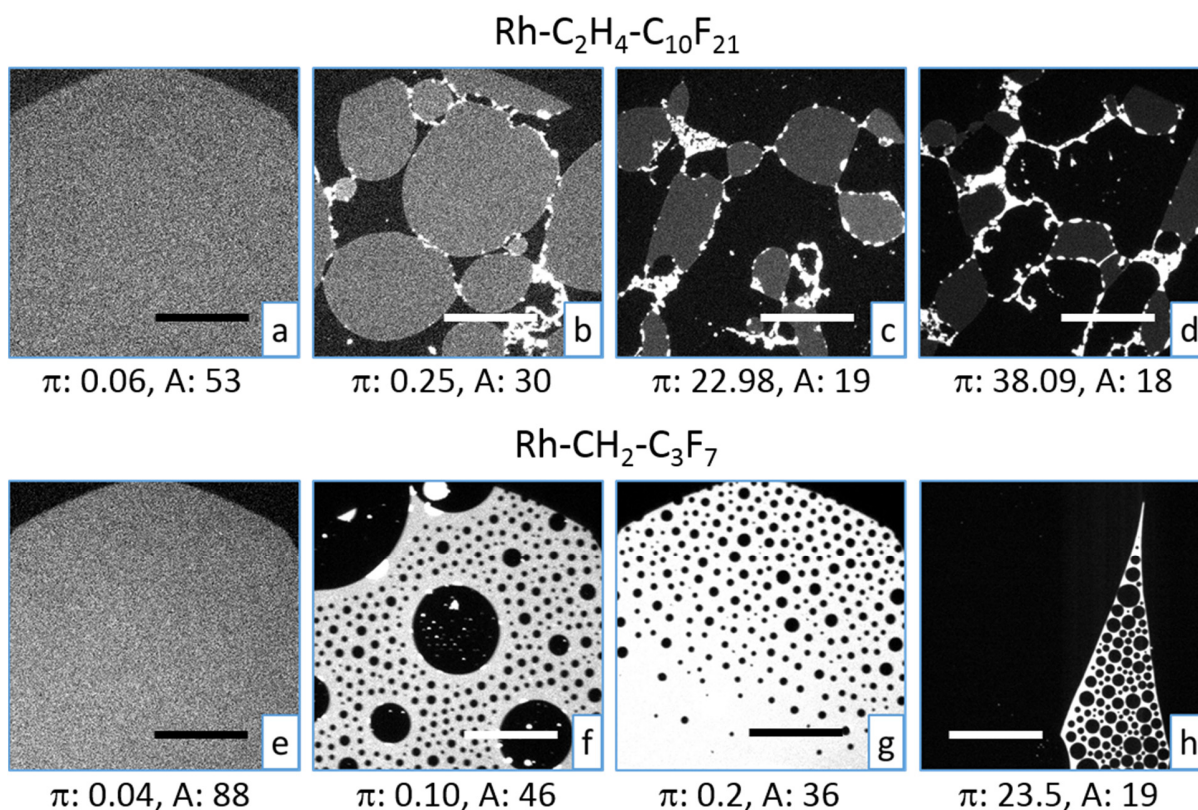
Fig. 3.13. Epifluorescence images (164×164 μm) of SA monolayer with 0.1 mol % Rh-C_2H_4-$C_{10}F_{21}$ dye (a-d) and 0.1 mol % Rh-CH_2-C_3F_7 dye (e-h). Scale bars: 50 μm. [π]: mN/m and [A]: Å^2/molecule.

The pure SA monolayer isotherm displaying the disordered, liquid-expanded, and liquid-condensed states as noticed from Fig. 3.12 is similar to previously reported SA Langmuir isotherms [212,213]. Epifluorescence measurements showed similar behavior to pure FC18 monolayers at low surface pressures in a sense that both dyes are homogeneously distributed throughout the monolayer as seen from Fig. 3.13a and e. Upon further compression, the Rh-C_2H_4-$C_{10}F_{21}$ dye concentrates mainly on the interfaces between the SA condensed phases in which the fluorescence dye partitions to a lesser extent as shown in Fig. 3.13b. Upon further compression, the dye is excluded from the condensed SA domains and remains mostly sandwiched between them. The Rh-CH_2-C_3F_7 was from the onset of SA domains formation excluded from the lipophilic SA domains as seen from Fig. 3.13f and upon further compression, the dark SA condensed domains increased in size as observed from Fig. 3.13h. Pure SA monolayers excluded both dyes from their condensed phases as observed in Fig. 3.13 since both dyes are immiscible with SA or other aliphatic solvents

such as n-hexane. But still, the Rh-C_2H_4-$C_{10}F_{21}$ concentrated at the interfaces between the condensed domains at high surface pressures as observed in Fig. 3.13d whereas Rh-CH_2-C_3F_7 concentrated in continuous domains dispersed between the condensed SA domains as seen in Fig. 3.13h.

A clear difference between the two long and short dyes was mostly observed in the pure FC18 monolayer isotherm experiments. Rh-CH_2-C_3F_7 is neither fluorophilic nor lipophilic enough to partition preferentially in the SA condensed domains. A more in-depth qualitative and quantitative discussion about fluorophilicity and lipophilicity is given in section 5.

The monolayer experiments clearly show a qualitative increase in fluorophilicity upon an increase in the length of the perfluorinated ponytails. The Langmuir monolayer experiments using a two dimensional (2D) fluorophilic-lipophilic phase separated system demonstrated that the F-rhodamine bearing the longest perfluorinated chain (Rh-C_2H_4-$C_{10}F_{21}$) exhibited the highest affinity to 2D fluorophilic phases. It partitions favorably in the condensed phases of FC18 pure monolayers at moderate surface pressures, whereas it is excluded from pure SA monolayers possessing both fluorophilic and lipophobic character. The Rh-CH_2-C_3F_7 is excluded from both fluorophilic (FC18) and lipophilic (SA) monolayers which confirms the fact that the fluorophilic character of the Rh-C_2H_4-$C_{10}F_{21}$ dye is due to its longer perfluorinated ponytails.

4 Confocal laser scanning microscopy (CLSM) GUVs investigations

4.1 Motivation

The ability of the four F-rhodamine fluorescence dyes to incorporate into lipid membranes was tested with mixed DOPC/F6H2OH or DPPC/F8H2OH GUVs obtained via electroformation. The GUVs were double stained with ATTO-633-DOPE, bearing two oleoyl acyl chains similar to DOPC, and the F-rhodamines. The ATTO-633-DOPE was used to stain the lipid membrane, and the F-rhodamines were added to test their incorporation into the pure phospholipid or the mixed GUVs. After electroformation at temperatures above the main phase transition of the lipids, the GUVs obtained were investigated via confocal laser scanning microscopy (CLSM). The affinity of the F-rhodamines to the mixed GUVs is expected to increase with the length of the perfluorinated ponytail. We are also interested to check the ability of the F-rhodamines to stain pure phospholipid GUVs. The incorporation of the F-rhodamines bearing longer perfluorinated moieties into mixed GUVs should escalate when the fluorotelomer alcohol to phospholipid molar ratio increases.

4.2 Experimental part

The preparation of GUVs by electroformation was realized via a similar way to the previously published electroformation protocol by Angelova and Dimitrov in 1986 [74]. A volume of 10 µL of a 10 mg/mL phosphocholine lipid in chloroform solution was spin coated on an ITO covered glass disk purchased from Präzisions Glas & Optik GmbH, Germany (25.2 mm diameter and 0.175 mm thickness) at 2000 rpm for 1 min at room temperature. The 10 µL chloroform drop was added on the ITO coated glass disk while spinning at 2000 rpm. Conducting copper tape (3M® single-sided adhesive, ¼ inch width) was used to connect the ITO-covered glass disk to the low-frequency generator. Rotilabo®-PE tube with inner diameter of 1 mm and the outer diameter of 1.8 mm purchased from Carl Roth GmbH (product number: 9583.1) was used to fill the flow cell with water. Silicon grease was applied to make the flow chamber water-tight. The flow cell was filled with degassed deionized water having a conductivity of 0.055 µS/cm and electroformation was performed with a sinusoidal alternating current having an effective voltage of 1.3 V and a frequency of 10 Hz supplied by a commercially available low-frequency generator (LFG) for 2 hours. Electroformation for DOPC and DOPC mixtures with F6H2OH were done at room temperature due its main transition temperature lying below room temperature (-17 °C) [4] and DPPC (main transition temperature 41 °C) [4] and DPPC mixtures with F8H2OH were heated to 60 °C before

starting electroformation then allowed to cool down slowly to room temperature before observation with the confocal microscope. A Leica TCS SP2 DM IRE2 confocal microscope equipped with an HCX PL APO lbd.BL 63x 1.2 W CORR (water immersion) objective (Leica Microsystems, Wetzlar, Germany) was used. Commercially available ATTO-633-DOPE (0.5 mol %) was used to stain the GUVs (excited with the HeNe laser (633 nm line)) with 655-695 nm detection range. The fluorinated synthesized rhodamines (0.5 mol %) were excited with the Ar-Kr laser (488 nm line) with 510-550 nm detection range. Imaging of GUVs was done at room temperature. Z-stacking was performed from bottom to top. Images were processed with Leica's software.

4.3 Results and discussion

Fluorotelomer alcohols are amphiphilic as discussed in section 1, so most probably they will incorporate into phospholipid GUVs. Firstly, a fluid-phase system at room temperature was used to access the incorporation of F-rhodamines into the lipid membrane with and without the addition of fluorotelomer alcohols. DOPC was used as the phospholipid and F6H2OH was used as the fluorotelomer alcohol. Hydrated DOPC is in the L_α phase at room temperature [4] and F6H2OH is a liquid in bulk at room temperature. Starting the investigation with a fluid-phase system is advantageous and less problematic since crystallization is not involved. GUVs can be relatively easily obtained from electroformation, and the different fluorescent probes can be observed through different channels with the possibility of overlaying the images to gain crucial information about miscibility, phase separation, coexistence, and affinities of the fluorescent probes being tested. GUVs obtained from DOPC/F6H2OH mixtures are illustrated in Fig. 4.1 using 0.5 mol % of both dyes. $Rh-C_2H_4-C_{10}F_{21}$ is observed through the green (left) channel, ATTO-633-DOPE is observed through the red (middle) channel, and the right column shows the overlay of both channels.
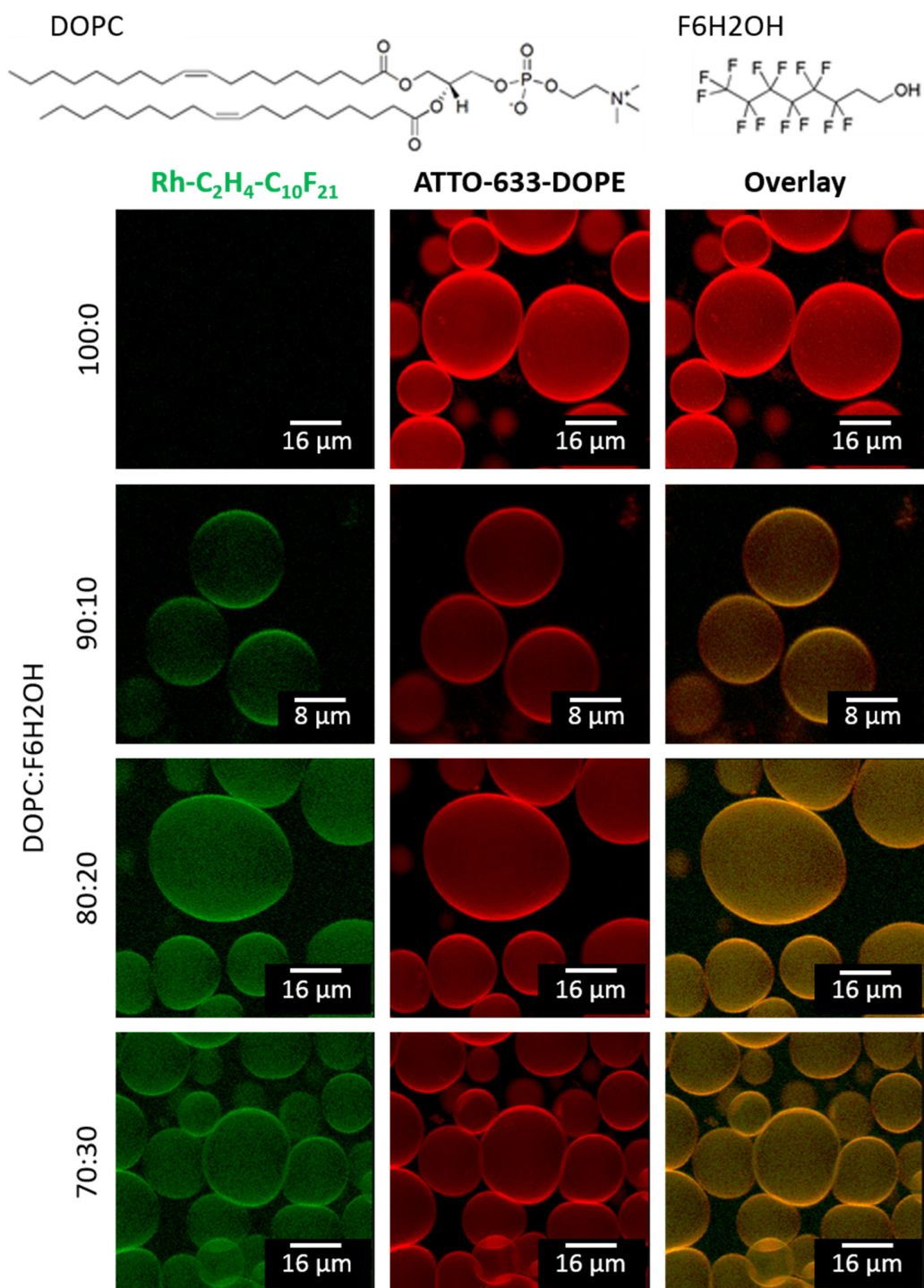
Fig. 4.1. CLSM z-stacking images of GUVs made from DOPC/F6H2OH (mol %) binary mixtures. Rh-C_2H_4-$C_{10}F_{21}$ dye (0.5 mol %) is observed through the green (left) channel, the ATTO-633-DOPE dye (0.5 mol %) is observed through the red (middle) channel and the right images show the overlay of both channels.
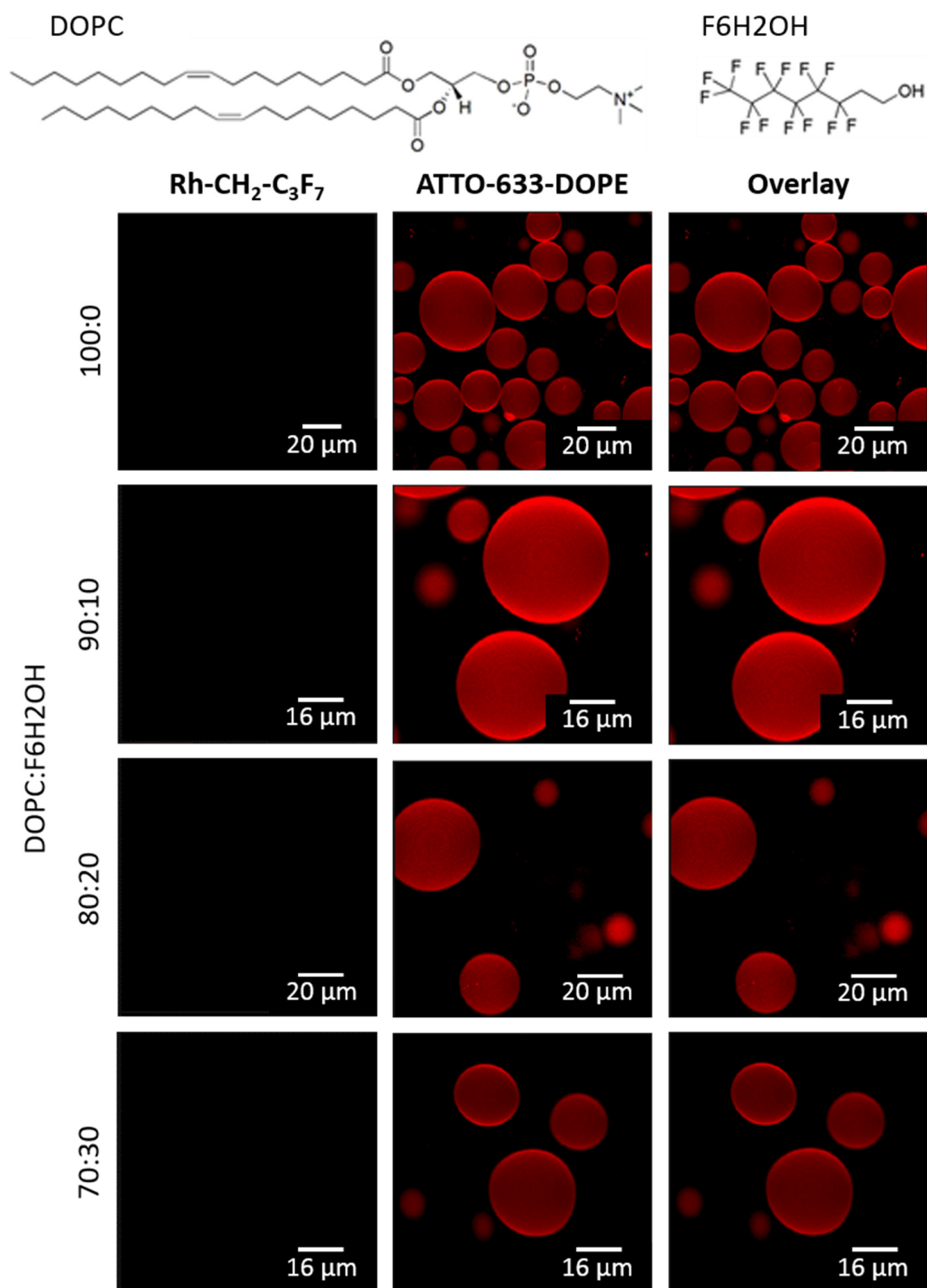
Fig. 4.2. CLSM z-stacking images of GUVs made from DOPC/F6H2OH (mol %) binary mixtures. Rh-CH$_2$-C$_3$F$_7$ dye (0.5 mol %) is observed through the green (left) channel, the ATTO-633-DOPE dye (0.5 mol %) is observed through the red (middle) channel and the right images show the overlay of both channels.

Pure DOPC GUVs exhibit a fluorescence only through the red (ATTO-633-DOPE) channel revealing that the Rh-C_2H_4-$C_{10}F_{21}$ does not partition into the pure DOPC GUVs. Upon the addition of F6H2OH, fluorescence through the green (Rh-C_2H_4-$C_{10}F_{21}$) channel is observed indicating that the corresponding F-rhodamine is incorporated into the phospholipid bilayer upon the addition of F6H2OH. The green color tends to increase upon further addition of F6H2OH since Rh-C_2H_4-$C_{10}F_{21}$ is soluble in the corresponding fluorotelomer alcohol. Similarly, the F-rhodamine fluorescence dye bearing the shortest perfluorinated chain (Rh-CH_2-C_3F_7) was tested with the DOPC/F6H2OH GUVs and it showed very different behavior as illustrated in Fig. 4.2. The Rh-CH_2-C_3F_7 does not incorporate either into the pure DOPC GUVs or the DOPC/F6H2OH mixed vesicles as clearly seen by the absence of fluorescence in the green (Rh-CH_2-C_3F_7) left channel of Fig. 4.2.

The differences in the length of the perfluorinated chains and spacers between the Rh-C_2H_4-$C_{10}F_{21}$ and the Rh-CH_2-C_3F_7 is big taking into consideration that one molecule of F-rhodamine bears two perfluorinated chains and spacers. From the first two experiments, it appears that the longer perfluorinated ponytail is the reason behind the Rh-C_2H_4-$C_{10}F_{21}$ partitioning in the fluorotelomer alcohol containing GUVs and that the Rh-CH_2-C_3F_7 shows no affinity towards DOPC/F6H2OH mixed GUVs.

The fact that both dyes are not partitioning in the lipid bilayer of pure DOPC vesicles suggests that their lipophilicity cannot be the only factor governing their incorporation into lipid membranes. To complement those preliminary findings, it was necessary to test all the synthesized dyes in a trial to check for trends of incorporation into the mixed GUVs that might be present and maybe even correlate with the length of the perfluoroalkyl ponytails. DOPC/F6H2OH 90:10 (mol %) mixtures were additionally tested with Rh-CH_2-C_7F_{15} and Rh-C_2H_4-C_8F_{17} respectively, and the results are displayed in Fig. 4.3. Both dyes (Rh-CH_2-C_7F_{15} and Rh-C_2H_4-C_8F_{17}) show similar behavior in the sense of not incorporating into the pure DOPC GUVs and incorporating in the 90:10 (mol %) mixed DOPC/F6H2OH GUVs as seen from the dark left green (F-rhodamine) channel when pure DOPC vesicles are present. Upon the addition of 10 mol % F6H2OH, fluorescence via the green channel is observed from both dyes indicating their incorporation into the mixed lipid bilayers.

Fig. 4.3. CLSM z-stacking images of GUVs made from DOPC/F6H2OH (mol %) binary mixtures. Rh-CH$_2$-C$_7$F$_{15}$ or Rh-C$_2$H$_4$-C$_8$F$_{17}$ dye (0.5 mol %) is observed through the green (left) channel, the ATTO-633-DOPE dye (0.5 mol %) is observed through the red (middle) channel and the right images show the overlay of both channels.

The green channel and their corresponding overlay pictures in Fig. 4.1 and 4.3 show a non-homogeneous lateral partitioning of the F-rhodamines when incorporated into the lipid/fluorotelomer alcohol mixed membranes which is an indication of microphase separation and the presence of fluorotelomer alcohol rich and poor phases within the mixed GUVs. The same phenomenon is not observed via the red channel since the F6H2OH dissolves the ATTO-633-DOPE dye so via the red channel, the ATTO-633-DOPE dye is homogeneously distributed into the phospholipid bilayer.

To complete the picture, the dyes having the longest (Rh-C_2H_4-$C_{10}F_{21}$) and shortest (Rh-CH_2-C_3F_7) perfluorinated ponytails were tested for their staining abilities with DPPC/F8H2OH mixed GUVs. DPPC vesicles are in an $L_{\beta'}$ gel phase, and the F8H2OH fluorotelomer alcohol is a solid at room temperature. This provides a gel-phase model that complements the previously investigated DOPC/F6H2OH fluid system. The results from using Rh-C_2H_4-$C_{10}F_{21}$ and ATTO-633-DOPE to stain DPPC/F8H2OH mixed GUVs are presented in Fig. 4.4 and 4.5 which obviously show that Rh-C_2H_4-$C_{10}F_{21}$ does not stain pure DPPC GUVs, but incorporates into the bilayer when F8H2OH is present. Pure DPPC GUVs are not homogeneously stained with ATTO-633-DOPE at room temperature because the DPPC vesicles are in the gel phase having ordered domains which exclude ATTO-633-DOPE and the dioleoyl moiety does not fit into the ordered dipalmitoyl gel phase. Nevertheless, less ordered domains in the DPPC vesicles are stained with ATTO-633-DOPE as seen through the middle (red) channel of Fig. 4.4 and 4.5. The DPPC/F8H2OH 90:10 (mol %) mixture shows the partitioning of the Rh-C_2H_4-$C_{10}F_{21}$ dye in the less ordered ATTO-633-DOPE stained domains which is clear from the overlay image in the right column, showing that the F8H2OH partitions preferentially in the less ordered gel phases of DPPC. Increasing the F8H2OH content to 20 mol % shows phase separation into red disconnected domains where the ATTO-633-DOPE dye is concentrated, and an ATTO-633-DOPE depleted dark domain as seen through the red channel of Fig. 4.4 and 4.5. The dark domain has higher order since it is ATTO-633-DOPE free. From the overlay picture, we notice that the Rh-C_2H_4-$C_{10}F_{21}$ is concentrated mostly in the ATTO-633-DOPE rich domains from their orange color, but is not completely excluded from the more ordered continuous domain which confirms the partitioning of F8H2OH in both domains.
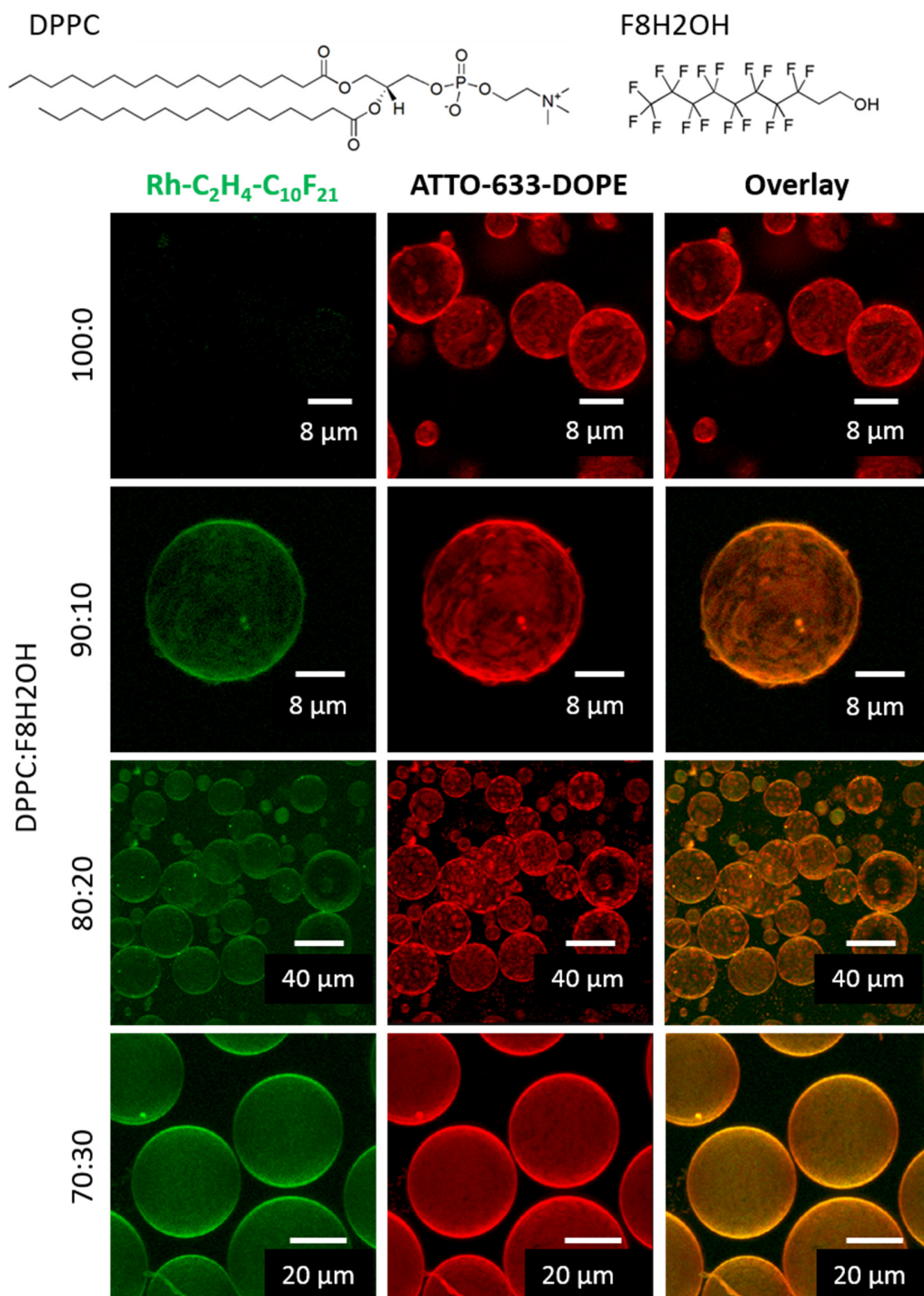
Fig. 4.4. CLSM z-stacking images of GUVs made from DPPC/F8H2OH (mol %) binary mixtures. Rh-C$_2$H$_4$-C$_{10}$F$_{21}$ dye (0.5 mol %) is observed through the green (left) channel, the ATTO-633-DOPE dye (0.5 mol %) is observed through the red (middle) channel and the right images show the overlay of both channels.
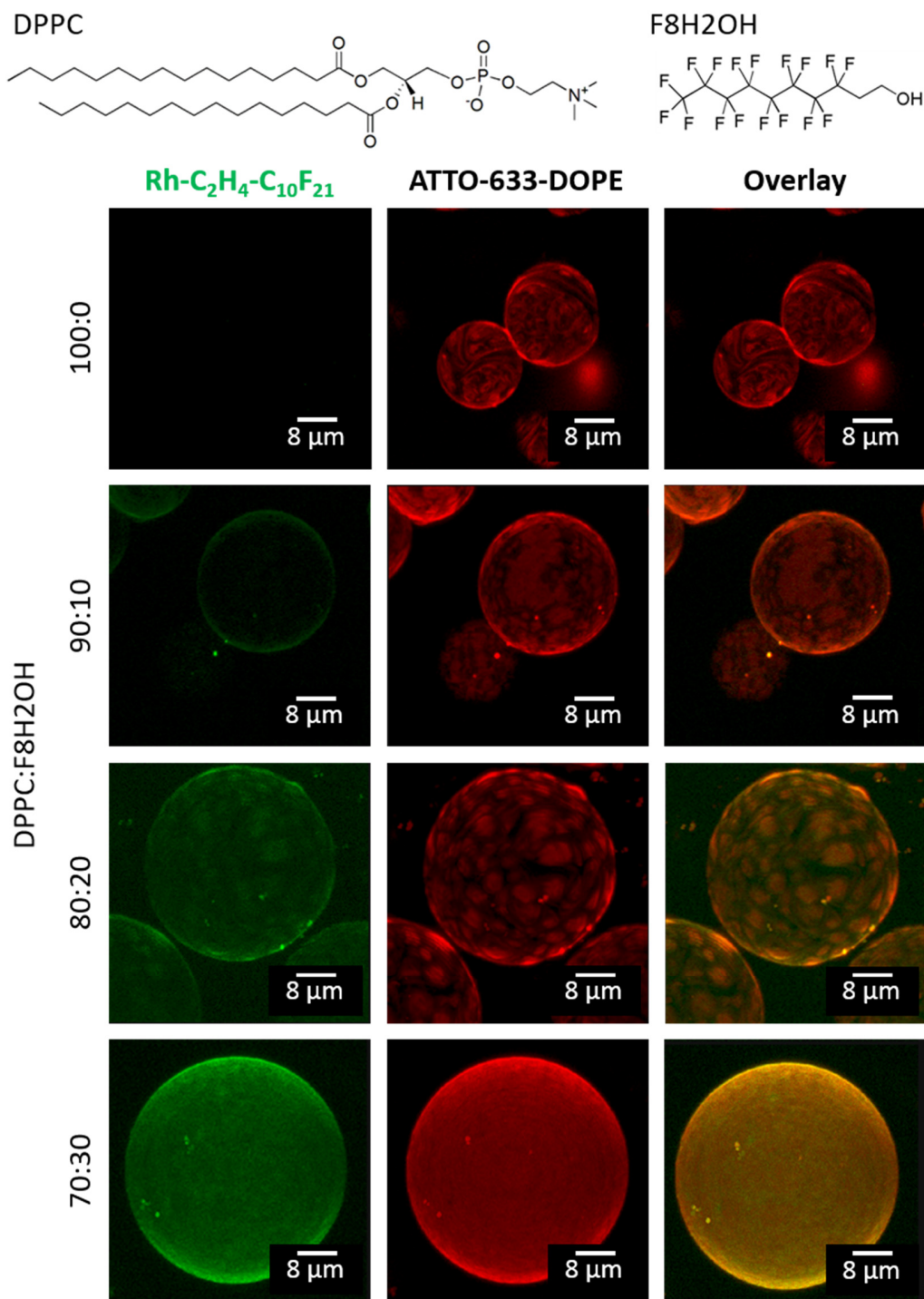
Fig. 4.5. CLSM z-stacking images of GUVs made from DPPC/F8H2OH (mol %) binary mixtures. Rh-C$_2$H$_4$-C$_{10}$F$_{21}$ dye (0.5 mol %) is observed through the green (left) channel, the ATTO-633-DOPE dye (0.5 mol %) is observed through the red (middle) channel and the right images show the overlay of both channels.

The 70:30 mol % mixed GUVs show very small highly ordered domains as black spots in the middle red channel and the green channel displays a non-homogeneous lateral partitioning of the Rh-C_2H_4-$C_{10}F_{21}$ dye. This becomes more evident by looking at the 70:30 mol % overlay pictures of Fig. 4.4 and 4.5.

Finally, the DPPC/F8H2OH mixed GUVs system was used to investigate the staining properties of Rh-CH_2-C_3F_7 dye bearing the shortest perfluorinated ponytails. The results are presented in Fig. 4.6 and at first glance, the green channels of pure DPPC and all its mixtures with F8H2OH are dark indicating the exclusion of Rh-CH_2-C_3F_7 dye from the pure DPPC and DPPC/F8H2OH mixed GUVs. It seems that the Rh-CH_2-C_3F_7 is neither lipophilic enough to incorporate into pure DPPC vesicles nor fluorophilic enough to partition into the DPPC/F8H2OH mixed GUVs. Only the ATTO-633-DOPE dye stained both the pure and mixed DPPC/F8H2OH GUVs which is consistent with the previous experiments. Some differences in the domain shapes are visible between the Rh-C_2H_4-$C_{10}F_{21}$ and the Rh-CH_2-C_3F_7 dye, which might be related to differences in the cooling rates after electroformation (done at 60 °C) or the absence of the fluorinated rhodamine dye. Although differences in domain shapes are found, for instance between the 90:10 mol % mixed GUVs of Fig. 4.4 and 4.6, but the less ordered red discontinuous domains, visible through the middle (red) channel, are still dispersed in a continuous dark more ordered domain. The 70:30 mol % mixture in Fig. 4.6 shows the coexistence of an ordered dark domain and a less ordered red domain as seen through the red (ATTO-633-DOPE) channel. The differences between the domain shapes can be related to two main reasons. The first is the differences in cooling rates after electroformation and the second being the absence of the Rh-CH_2-C_3F_7 in the mixed GUVs.

A qualitative difference between the fluorinated rhodamine bearing the longest (Rh-C_2H_4-$C_{10}F_{21}$) and shortest (Rh-CH_2-C_3F_7) perfluorinated chains was observed. The Rh-C_2H_4-$C_{10}F_{21}$ is obviously more fluorophilic than the Rh-CH_2-C_3F_7 due to its incorporation into the fluorotelomer alcohol mixed GUVs. A more quantitative approach for fluorophilicity, mainly for aliphatic fluorination, will be introduced and discussed in section 5.

Fig. 4.6. CLSM z-stacking images of GUVs made from DPPC/F8H2OH (mol %) binary mixtures. Rh-CH$_2$-C$_3$F$_7$ dye (0.5 mol %) is observed through the green (left) channel, the ATTO-633-DOPE dye (0.5 mol %) is observed through the red (middle) channel and the right images show the overlay of both channels.
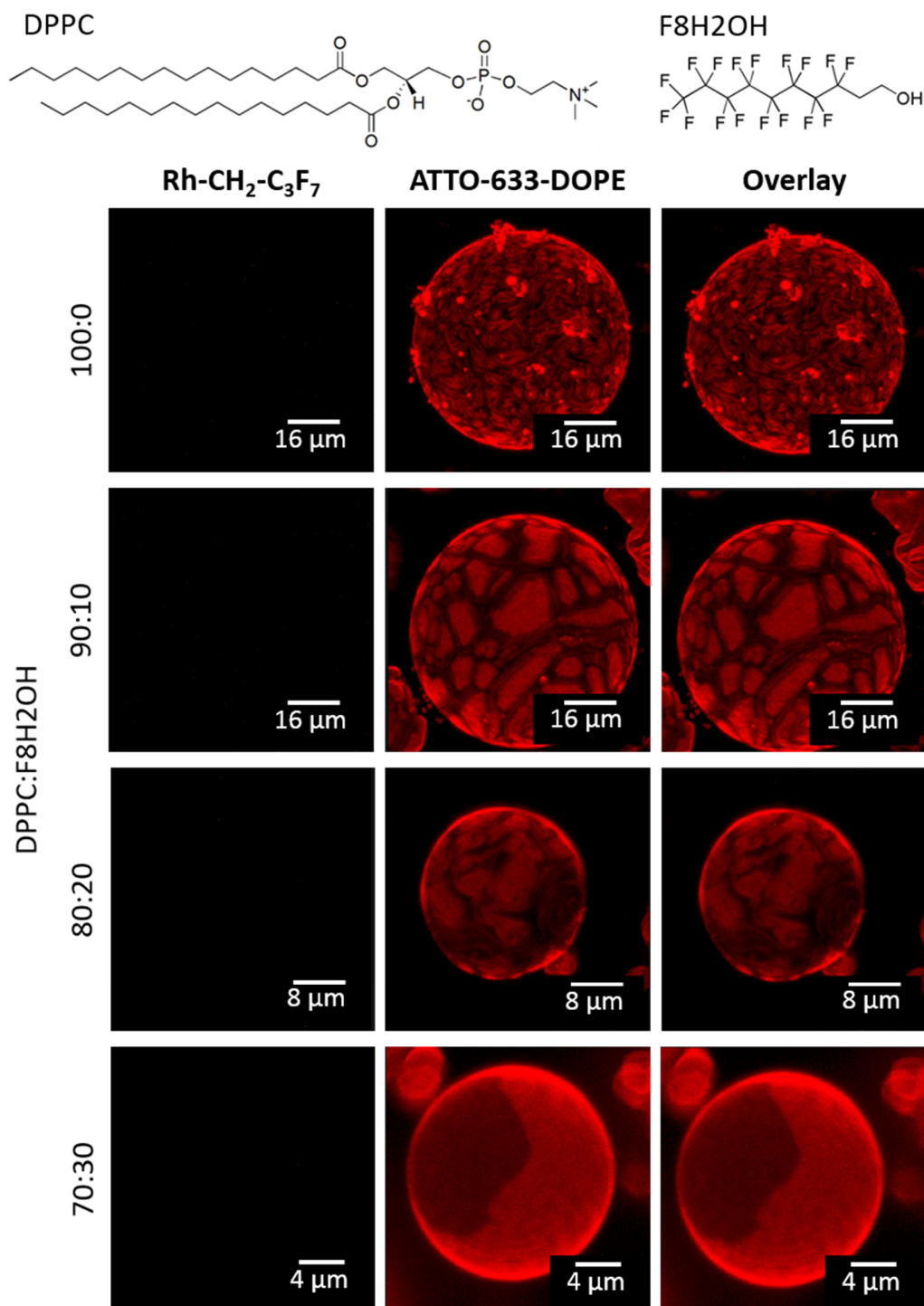
5 Fluorophilicity and lipophilicity quantifications with 1H,1H,2H,2H-perfluoro-1-octanol/water (ln $P_{\text{F6H2OH/W}}$) and 1-octanol/water (ln $P_{\text{O/W}}$) partition coefficients

5.1 Motivation

In an attempt to explain the mode of action of gaseous or volatile anesthetics, it was observed by H. Meyer that anesthetics tend to concentrate in fatty environments such as nerve tissue [214]. C. E. Overton came to similar conclusions, and it was observed that the effect of anesthetic correlated with the olive oil/air partition coefficient which became known as the Meyer-Overton theory of anesthesia [215]. Furthermore, Mullins stressed the importance of the solubility parameter as a major factor in the mechanism of narcosis [216] showing that the Meyer-Overton hypothesis was not complete as reviewed later by Miller [217]. Hansch and Dunn partition coefficients experiments showed an excellent correlation between the biological activity of drugs and their 1-octanol/water partition coefficients superior to the oil/water or alkane/water partition coefficients [218]. Later, Hansch et al. determined 1-octanol/water partition coefficients of 32 gaseous anesthetics and showed that their potency depends on their lipophilicity which they defined by $\log P_{\text{1-octanol/water}}$ and on a polar factor [219]. They established additional polar components also play an important role since the presence of polar hydrogens greatly increased the anesthetic potency, and formulated a structure-activity relationship based on both, lipophilicity and polarity [219]. After defining the 1-octanol/water partition coefficient as a method to quantify lipophilicity in biologically relevant systems, Seydel and Schaper published a quantitative structure-pharmacokinetic relationships (QSPR) method based on quantitative structure-activity relationship (QSAR) methods in an attempt to predict pharmacokinetic and toxic properties before synthesis which can help to increase the efficiency in designing new drugs [220]. The 1-octanol/water partition coefficient of several organic compounds was studied in detail by Sangster from both, the thermodynamic and experimental parts in addition to the partition coefficients of 600 organic compounds including alkanes, aromatics, unsaturated hydrocarbons, ethers, alcohols, ketones, acids, amines, amides and much more [221]. The 1-octanol/water partition is influenced mainly by two main factors which are the solute polarizability, hydrogen-bond basicity, and the size of the solute. Polarizable and hydrogen-bond accepting solutes partition more in the aqueous phase, whereas an increase in the

size of the solute leads to it partitioning favorably in the 1-octanol phase [153]. The 1-octanol bearing a polar headgroup and a flexible lipophilic tail is amphiphilic in a comparable way to phospholipids and proteins found in cell membranes making the 1-octanol/water partition coefficient a suitable model for the partitioning between bio and aqueous phases [154].

Perfluoroalkyl chains and fluorine substituents have several effects on the physicochemical properties of biologically relevant compounds. The fluorine atom has a high electronegativity, small size, and very low polarizability upon which proton substitutions with fluorine lead to several consequences one of which is the increase or decrease of lipophilicity upon fluorination [156]. Upon the increase in length of the perfluorinated chains for instance, perfluorinated surfactants such as perfluorooctane sulfonate (PFOS) or perfluorocarboxylic acids such as perfluorooctanoic acid (PFOA), the classical 1-octanol/water partition coefficient has some limitations mainly with the low solubility of such molecules in the 1-octanol and the water phases where the addition of the PFOS or PFOA leads to a third phase formation. Some approximations are used such as the ratio of their solubility in the pure organic, and aqueous phases. Here, their solubility in pure 1-octanol is usually about 56 mg/mL and in pure water is approximately 520 mg/mL but it significantly drops in salty environments such as natural seawater where the solubility is 12.4 mg/mL at ambient temperature [204]. Solubility problems make it increasingly more difficult to predict the partitioning behavior of numerous highly fluorinated compounds such as fluorotelomer alcohols and fluorotelomer olefins due to their environmental concerns and thus rely mainly on modeling and approximations [205]. Another problem with the perfluorinated carboxylic acids is the failure of the 1-octanol/water partition coefficient to explain their lipophilicity due to their very low pK_a values rendering them ionized at environmentally relevant pH values which requires much more sophisticated and time-consuming methods to evaluate and understand their bioaccumulation [206]. The 1-octanol/water partition coefficient seems to have a limited success for some lightly-fluorinated alcohols and carbohydrates [207]. Molecular dynamic simulations using force fields that investigate local solvation environments around the hydroxyl groups are also in use to evaluate the effect of fluorination on the physical properties of perfluorinated and fluorotelomer alcohols [222]. Due to the solubility problems rendering the 1-octanol/water partition coefficient almost impossible to calculate, Hidalgo and Mora-Diez recently used *ab initio* to calculate the partition coefficients of carboxylic acids, perfluorinated carboxylic acids, and their conjugate bases [223]. In sections 5.2 and 5.3, we will try to introduce a new partition coefficient that has the potential to replace the classical 1-octanol/water system when highly fluorinated species are involved.

When dealing with highly fluorinated molecules, a fluorous partition coefficient between PFMC and toluene is rigorously used and sometimes termed fluorophilicity [149]. The PFMC/toluene partition coefficient became famous after a paper published by Horváth and Rábai in 1994 where they used the PFMC/toluene biphasic system at ambient temperature and pressure to conduct hydroformylation of olefins by using fluorous cobalt or rhodium catalysts which after the reaction partition favorably into the PFMC phase simplifying the purification process [135]. The PFMC-toluene partition coefficient is highly relevant to the transition metal catalyzed syntheses due to several advantages including simple purification processes and good catalyst recovery [138]. Additionally, progress was achieved in the ability to calculate the PFMC/toluene partition coefficient with high fidelity using 3D QSAR descriptors and artificial neural networks, linear free energy relation (LFER), and molecular surface areas [146-148]. However, the PFMC/toluene partition coefficient is not biologically relevant mainly due to the absence of an aqueous phase, and the compound partitioning in the PFMC phase needs to be highly fluorinated and lack the presence of polar groups, hydrogen bonding capabilities, and π-π interactions [146]. The problems encountered using the 1-octanol/water or PFMC/toluene partition coefficients trigger the need for an extra partition coefficient between a fluorinated phase and water which has biological relevance, and can complement the well-established 1-octanol/water biphasic system. The 1-octanol phase was substituted with the more fluorophilic 1H,1H,2H,2H-perfluoro-1-octanol (F6H2OH) and the partition coefficients of the F6H2OH/W biphasic system for the four F-rhodamines were determined. The fluorophilic to lipophilic ration was also quantified using the perfluoro-n-octane (F-oct)/n-octane (oct) partition coefficient and compared with the classical PFMC/toluene system.

5.2 Experimental part

Varian-Cary 4000 double beam UV-Vis spectrometer was used for UV-Vis measurements. BRAND® UV micro single-use cuvettes (mfr. no. BRAND® 7592 20) with center height 15 mm having a 1 cm path length were filled with 500 μL 2,2,2-trifluoroethanol (TFE) solutions. UV-Vis measurements were done with baseline correction (subtraction) at a temperature of 20 °C. Fluorescence was measured by a FluoroMax 2 spectrometer (Jobin-Yvon). 200 μL solutions were placed in a Hellma SUPRASIL® cuvette (105.250-QS) with center height 15 mm. For fluorescence emission spectra, $\lambda_{abs,max}$ was used to excite the corresponding F-rhodamines. Rh-CH$_2$-C$_3$F$_7$ and Rh-CH$_2$-C$_7$F$_{15}$ were excited at 490 and 491 nm, respectively, whereas Rh-C$_2$H$_4$-C$_8$F$_{17}$ and Rh-

C_2H_4-$C_{10}F_{21}$ were excited at 504 nm. The calibration of the FluoroMax 2 spectrometer was checked with the water Raman peak at 397 nm before and after the measurement of each sample. All fluorescence measurements were done at 20 °C. Emission spectra were recorded with 0.5 nm increments, 0.1 s integration time, and 2 nm excitation and emission slits. The emission spectra were recorded as counts per second (cps) as a function of the wavelength (nm) using S/R (signal/reference) detection mode to compensate the aging effect of the xenon lamp. The partition coefficients between 1-octanol and water or F6H2OH and water were calculated using the shake-flask method of mutually saturated solvents as published by Sangster [221]. F-rhodamines were dissolved into 10 mL 1-octanol or F6H2OH saturated with water and diluted stepwise to a final concentration of 1.5 μM (linear regime). 5 mL of both organic solutions were transferred into a centrifuge tube and 5 mL of water saturated with the corresponding organic phase were added. The centrifuge flasks were closed and shaken vigorously for some time and left to phase separate. This procedure was repeated several times, and the systems were allowed to phase separate for 12 h in the dark. Later, the tubes were centrifuged at 4000 rpm for 2 min to achieve a good phase separation. 1 mL of each organic phase was transferred using a 1 mL volumetric pipette before and after the aqueous wash. The organic solvents were evaporated under a nitrogen gas stream to dryness and 1 mL TFE was added to the dried samples. Emission flux was measured before and after the aqueous washing. The partition coefficient was measured indirectly via the loss of analyte from the organic (1-octanol or F6H2OH) to the aqueous phase. The partition coefficient between perfluoro-*n*-octane and *n*-octane were calculated in a similar way also using the shake-flask method. 250 μL of 30 μM acetonitrile standard solutions of the F-rhodamines were transferred into 20 mL centrifuge tubes, and the solvent was evaporated to dryness under a nitrogen stream. 5 mL of perfluoro-*n*-octane and *n*-octane were added, and the centrifuge tubes were closed and transferred into a water bath thermostated at 82 °C slightly above the upper critical solution temperature (UCST) of the biphasic system to mix the two solvents [224]. The flasks were shaken vigorously from time to time, left to cool down slowly overnight, and centrifuged at 4000 rpm for 2 min to get a fine phase separation. 1 mL samples from each phase were taken, dried under a nitrogen stream and dissolved into 1 mL TFE for fluorescence spectroscopy quantitative analysis.

5.3 Results and discussion

The ability of the Rh-CH₂-C₇F₁₅ dye to stain fluorine-containing DOPC GUVs in comparison with the Rh-CH₂-C₃F₇ that cannot stain them as seen in section 4, in addition to the fact that both dyes do not partition into pure DOPC GUVs is compelling. In a quest to seek an explanation for the observed differences between the two dyes, firstly partition coefficients between 1-octanol and water were measured to quantify the lipophilicity of the F-rhodamine dyes and the results are shown in Table 5.1.

Table 5.1. Quantum yield (Φ), absorption and emission maxima (λ_{max}(abs) and λ_{max}(em)), molar absorptivity (ε), and the partition coefficients of the synthesized F-rhodamines in several biphasic systems.

	$CH_2\text{-}C_3F_7$	$CH_2\text{-}C_7F_{15}$	$C_2H_4\text{-}C_8F_{17}$	$C_2H_4\text{-}C_{10}F_{21}$
Φ^a	0.91	0.93	0.88	0.87
λ_{max}(abs) [nm]^b	490	491	504	504
λ_{max}(em) [nm]^b	512	513	526	526
ε [M⁻¹cm⁻¹]^c	33450	36340	42130	40250
ln $P_{O/w}{}^d$	1.29	1.32	3.09	3.40
ln $P_{F6H2OH/w}{}^d$	2.67	4.98	5.11	5.85
ln $P_{F\text{-oct/oct}}{}^e$	-3.54	-1.67	-1.94	-0.77
ln $P_{PFMC/Toluene}{}^e$	-7.09	-4.68	-5.67	-3.32

^{a}Quantum yield measured in 2,2,2-trifluoroethanol (TFE) at 20 °C using 0.1 M NaOH aqueous fluorescein solution as reference. ^{b}Obtained from absorption and emission (fluorescence) spectra in TFE at 20 °C. ^{c}Molar absorptivity calculated in TFE at 20 °C. ^{d}Partition coefficients measured by fluorescence spectroscopy in TFE at 20 °C indirectly by the loss of analyte from the organic phase after the aqueous wash. ^{e}Partition coefficients measured by fluorescence spectroscopy in TFE at 20 °C.

The first striking observation in Table 5.1 is the small difference between the lipophilicities of Rh-CH₂-C₃F₇ and Rh-CH₂-C₇F₁₅ (1.29 and 1.32), respectively. An increase by four fluorinated methylene groups in the length of the perfluorinated chain was not accompanied by a substantial

increase in lipophilicity. At first glance, this is very strange and to make things more interesting, Rh-C$_2$H$_4$-C$_8$F$_{17}$ and Rh-C$_2$H$_4$-C$_{10}$F$_{21}$ show higher lipophilicities than the former F-rhodamines bearing only one methylene spacer between the amine and the perfluorinated chain. A substantial increase in lipophilicity was observed with the elongation of the methylene spacer but not the perfluorinated chain. It seems that the length of the perfluorinated chain has less effect on lipophilicity than the aliphatic one. This can be rationalized for the synthesized F-rhodamines since they possess two amine and one aromatic carboxylic acid polar groups that dominate the interactions between the F-rhodamines and their environments which in this case are the 1-octanol or the water phases. On the other hand, an increase in the length of the aliphatic spacer shifts the equilibrium towards the 1-octanol phase which is reasonable due to more favorable interactions with the organic phase and a decrease in the electron withdrawing effect of the perfluorinated chain on the amine groups due to the better shielding obtained by the two methylene spacers. The classical 1-octanol/water partition coefficient did not deliver satisfactory results, so we replaced 1-octanol with 1H,1H,2H,2H-perfluoro-1-octanol (F6H2OH), a similar compound bearing the same number of carbons, but highly fluorinated. The results are shown in Table 5.1, and it is clearly observed that the F6H2OH/water partition coefficient is sensitive to the perfluorinated chain length since the partition coefficient increased systematically with the increase in the length of the perfluorinated chain. The F6H2OH bears the same polar headgroup as the 1-octanol with a similar acidity thanks to the two methylene spacers shielding the alpha-carbon from the electron withdrawing effect present by the perfluorinated group. Besides, F6H2OH bears a six carbon atom perfluorinated chain which makes it similar to other compounds bearing perfluorinated groups and some other polar functionalities. It works pretty well for our dyes and might also be useful in cases such as perfluorinated carboxylic acids where their limited solubility becomes an issue. The F6H2OH/water partition coefficient is a very good candidate to measure fluorophilicity for fluorinated biologically relevant molecules. The F6H2OH/water partition coefficient proves that the Rh-CH$_2$-C$_7$F$_{15}$ stains the fluorinated DOPC GUVs due to its higher fluorophilicity in comparison with the Rh-CH$_2$-C$_3$F$_7$ dye.

Another partition coefficient between perfluoro-*n*-octane and *n*-octane was measured, and the results are shown in Table 5.1. All the synthesized dyes partition preferentially into the *n*-octane phase but still the Rh-CH$_2$-C$_3$F$_7$ partitions much less in the perfluoro-*n*-octane phase in comparison to Rh-C$_2$H$_4$-C$_{10}$F$_{21}$. An interesting observation is the difference between Rh-CH$_2$-C$_7$F$_{15}$ and Rh-C$_2$H$_4$-C$_8$F$_{17}$ having ln $P_{\text{F-oct/oct}}$ of -1.67 and -1.94 respectively i.e. the partitioning in the

perfluorinated phase decreased upon an increase in the length of the perfluorinated chain. However, this observation is not strange since the aliphatic spacer is also increased in length from one to two methylene groups. The stronger intermolecular dipole-dipole interactions between aliphatic chains in comparison with the weaker dipole-dipole interactions present between perfluorinated chains leads to an overall increase in lipophilicity when both aliphatic and perfluorinated chains are increased by one methylene unit. A similar trend is observed from the classical PFMC-toluene partition coefficients as displayed in Table 5.1 being even more negative than the F-oct/oct partition coefficients. The reason why F-rhodamines are partitioning more in toluene in comparison with the n-octane phase is the π-π interactions between the aromatic core of the F-rhodamines and toluene which drastically increases the partitioning of the fluorescence dyes into the toluene phase [146]. The partition coefficients between 1-octanol and water i.e. the lipophilicity of both Rh-CH$_2$-C$_7$F$_{15}$ and Rh-C$_2$H$_4$-C$_8$F$_{17}$ (1.32 and 3.09 respectively) also show an increase upon the addition of one methylene spacer.
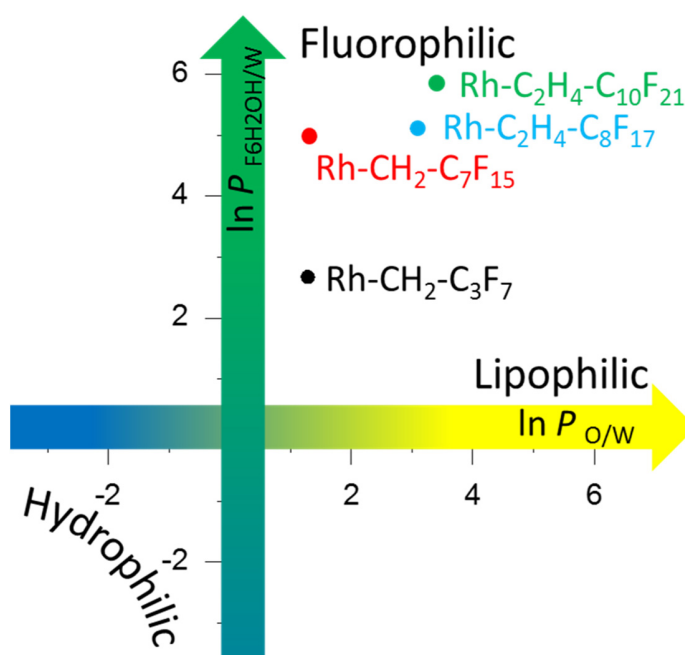
Scheme 5.1. A plot of the ln $P_{O/W}$ vs. ln $P_{F6H2OH/W}$ for the four synthesized F-rhodamines (the numerical values are given in Table 5.1).

A plot of the lipophilic scale (ln $P_{O/W}$) on the abscissa versus the fluorophilic scale (ln $P_{F6H2OH/W}$) on the ordinate in an orthonormal system is shown in Scheme 5.1. The plot makes it clear that compounds having positive ln $P_{O/W}$ and ln $P_{F6H2OH/W}$ belong to the upper-right quadrant in Scheme

5.1 making them lipophilic and fluorophilic. Larger ordinate values imply a higher fluorophilicity, and larger abscissa values suggest a higher lipophilicity. Logically hydrophilic compounds should be located in the lower-left quadrant since they partition preferentially in the aqueous phase yielding negative partition coefficients.

6 Conclusions and outlook

Four fluorinated rhodamine-based fluorescence dyes (F-rhodamines) bearing perfluorinated ponytails with methylene spacers on their amine groups were successfully synthesized and characterized with ^{1}H, ^{19}F NMR spectroscopy, and ESI-ToF mass spectrometry. The Rh-CH$_2$-C$_3$F$_7$ and Rh-CH$_2$-C$_7$F$_{15}$ had one-methylene group (CH$_2$) spacers between the perfluorinated ponytails and the amine groups. The Rh-C$_2$H$_4$-C$_8$F$_{17}$ and the Rh-C$_2$H$_4$-C$_{10}$F$_{21}$ had a two-methylene groups (C$_2$H$_4$) spacers between the perfluorinated ponytails and the amine groups. Rh-C$_2$H$_4$-C$_8$F$_{17}$ and Rh-C$_2$H$_4$-C$_{10}$F$_{21}$ had 13 nm red-shifted UV-Vis absorption and fluorescence emission spectra with respect to Rh-CH$_2$-C$_3$F$_7$ and Rh-CH$_2$-C$_7$F$_{15}$ due to a decrease in the electron withdrawing effect on the amine groups from the two-methylene groups (C$_2$H$_4$) aliphatic spacers. All four synthesized F-rhodamines have a 22 nm Stokes shift and are highly fluorescent in protic media such as TFE and showed similar optical properties to other rhodamine dyes. Another similarity between the F-rhodamines and other rhodamines was the absence of a bright fluorescence in aprotic media such as THF and toluene where the spirolactone structure prevails. The lipophilicity of the four synthesized F-rhodamines was quantified with the 1-octanol/water partition coefficient and found to be correlating mainly with the length of the methylene spacers rather than the one of the perfluorinated chains. Preliminary experiments for the affinity of the F-rhodamines to fluorinated phases were realized with perfluorostearic acid (FC18) and stearic acid (SA) mixed monolayers and studied with epifluorescence microscopy on the Langmuir trough. A clear affinity of the Rh-C$_2$H$_4$-C$_{10}$F$_{21}$ dye to the FC18 domains paralleled by the exclusion of Rh-CH$_2$-C$_3$F$_7$ dye from those domains show a clear difference in the fluorophilicity of both dyes proving that the F-rhodamine bearing the longer perfluorinated ponytail is much more fluorophilic than the one bearing the shorter perfluoroalkyl moiety. Due to the promising mixed monolayer results, the ability of the F-rhodamines to stain phospholipid model membranes was studied with giant unilamellar vesicles (GUVs) obtained by electroformation and inspected by confocal laser scanning microscopy (CLSM). The incorporation of the three F-rhodamines (Rh-CH$_2$-C$_7$F$_{15}$, Rh-C$_2$H$_4$-C$_8$F$_{17}$, and Rh-C$_2$H$_4$-C$_{10}$F$_{21}$) bearing the longer perfluorinated ponytails into GUVs drastically increased upon 1H,1H,2H,2H-perfluoro-1-octanol (F6H2OH) and 1H,1H,2H,2H-perfluoro-1-decanol (F8H2OH) fluorotelomer alcohols incorporation in the liquid crystalline (DOPC) and gel phase (DPPC) vesicles respectively, whereas the Rh-CH$_2$-C$_3$F$_7$ showed extremely low affinity to both pure phospholipid and phospholipid-fluorotelomer alcohol mixed GUVs as shown from the double

staining with ATTO-633-DOPE and F-rhodamine experiments. In double staining experiments, the F-rhodamines did not stain pure phospholipid GUVs, but the $Rh\text{-}CH_2\text{-}C_7F_{15}$ stained the mixed vesicles on the contrary to the $Rh\text{-}CH_2\text{-}C_3F_7$ dye which did not incorporate into the mixed GUVs. Although they differ slightly in their lipophilicity, their incorporation behavior into mixed vesicles was very different which led to the introduction of the F6H2OH/water partition coefficient as a scale for fluorophilicity to explain the differences between both dyes. The partition coefficients between F6H2OH and water for the $Rh\text{-}CH_2\text{-}C_3F_7$ and $Rh\text{-}CH_2\text{-}C_7F_{15}$ dyes are different and correlate with the length of the perfluorinated ponytails. The introduced partition coefficient was sensitive to the amount of fluorination which makes it a complementary candidate for fluorophilicity quantification of highly fluorinated pharmaceuticals, and it might solve some problems related to lipophilicity calculation of highly perfluorinated surfactants due to their limited solubility in the 1-octanol/water biphasic system. The partitioning of the F-rhodamines cannot be completely excluded from pure phospholipid GUVs since they are not water soluble. It might be that the F-rhodamines partition to a minimal extent in the hydrophobic region of the bilayer which will practically switch-off the fluorescence due to the formation of the spirolactone form in hydrophobic and aprotic environments.

In the outlook, it should be suggested that some possible improvements can be made to achieve detection with fluorescence techniques of fluorophilic phases. The fluorotelomer alcohols are simple amphiphiles and different from membrane lipids since they have one polar headgroup and one hydrophobic tail, whereas most lipids have a hydrophilic headgroup and two hydrophobic tails. Those major differences make it only possible for the fluorotelomer alcohol to incorporate into the membrane, but not forming a part of it since their hydrophobic to hydrophilic volume fraction ratios are less than that of the phospholipids. We conclude that to obtain fluorophilic-lipophilic phase separated vesicles; it would be necessary to synthesize highly fluorinated lipids keeping in mind that the perfluorinated ponytails should be short enough to keep the lipid in the liquid crystalline phase at ambient temperatures. This narrows the options down to lipid synthesis for instance from highly fluorinated acids with one or two methylene spacers esterified to L-α-glycerylphosphorylcholine. Highly fluorinated lipid synthesis opens the door for fluorophilic lipids and vesicles which should have thinner membranes due to the shorter perfluoroalkyl chains used. Fluorophilic vesicles should be stable and might work better for drug delivery especially for highly fluorinated drugs or even other pharmaceuticals. The perfluorinated chain should not exceed six

carbon atoms so as a starting candidate the 1H,1H-perfluoro-1-octanoic acid or the 1H,1H,2H,2H-perfluoro-1-nonanoic acid are recommended. Keeping in mind that the latter highly fluorinated carboxylic acid might prove better if long time stability is required due to the lower acidity which makes the lipids less prone to hydrolysis, whereas the former is more advantageous when chemical stability is not needed for long times. Thinner membranes might also have better permeability especially for fluorinated active ingredients, and moreover, these lipids can be headgroup stained by several commercially available hydrophilic fluorescence dyes to be used in fluorescence investigations such as in CLSM.

7 References

[1]   M.S. Bretscher, M.C. Raff, Mammalian plasma membranes, Nature. 258 (1975) 43–49.

[2]   G. van Meer, D.R. Voelker, G.W. Feigenson, Membrane lipids: where they are and how they behave, Nat. Rev. Mol. Cell Biol. 9 (2008) 112–124.

[3]   L. Karnovsky, E. Cohn, B. Keil, C. Likbecq, B. Malmstrom, R. Schwyzer, O. Ridge, E. Baer, IUPAC-IUB Commission on Biochemical Nomenclature (CBN)., Eur. J. Biochem. 2 (1967) 127–131.

[4]   H. Matsuki, M. Goto, K. Tada, N. Tamai, Thermotropic and Barotropic Phase Behavior of Phosphatidylcholine Bilayers, Int. J. Mol. Sci. 14 (2013) 2282–2302.

[5]   G. Cevc, Phospholipids handbook, Marcel Dekker, Inc., New York, 1993.

[6]   G.L. Nicolson, The Fluid—Mosaic Model of Membrane Structure: Still relevant to understanding the structure, function and dynamics of biological membranes after more than 40years, Biochim. Biophys. Acta - Biomembr. 1838 (2014) 1451–1466.

[7]   P. V. Escribá, J.M. González-Ros, F.M. Goñi, P.K.J. Kinnunen, L. Vigh, L. Sánchez-Magraner, A.M. Fernández, X. Busquets, I. Horváth, G. Barceló-Coblijn, Membranes: a meeting point for lipids, proteins and therapies, J. Cell. Mol. Med. 12 (2008) 829–875.

[8]   S.H. White, G.I. King, Molecular packing and area compressibility of lipid bilayers., Proc. Natl. Acad. Sci. 82 (1985) 6532–6536.

[9]   M.A. Hemminga, Interpretation of ESR and saturation transfer ESR spectra of spin labeled lipids and membranes, Chem. Phys. Lipids. 32 (1983) 323–383.

[10]   D. Walz, J. Teissié, G. Milazzo, Bioelectrochemistry of Membranes, pp 61-152, Birkhäuser Verlag, Basel, 2004.

[11]   D. Huster, K. Arnold, K. Gawrisch, Influence of Docosahexaenoic Acid and Cholesterol on Lateral Lipid Organization in Phospholipid Mixtures, Biochemistry. 37 (1998) 17299–17308.

[12]   V. Castro, S. V. Dvinskikh, G. Widmalm, D. Sandström, A. Maliniak, NMR studies of membranes composed of glycolipids and phospholipids, Biochim. Biophys. Acta -

Biomembr. 1768 (2007) 2432–2437.

[13] H.A. Scheidt, D. Huster, The interaction of small molecules with phospholipid membranes studied by 1H NOESY NMR under magic-angle spinning, Acta Pharmacol. Sin. 29 (2008) 35–49.

[14] T.M. Ferreira, B. Medronho, R.W. Martin, D. Topgaard, Segmental order parameters in a nonionic surfactant lamellar phase studied with 1H–13C solid-state NMR, Phys. Chem. Chem. Phys. 10 (2008) 6033.

[15] T.M. Ferreira, O.H.S. Ollila, R. Pigliapochi, A.P. Dabkowska, D. Topgaard, Model-free estimation of the effective correlation time for C–H bond reorientation in amphiphilic bilayers: 1H–13C solid-state NMR and MD simulations, J. Chem. Phys. 142 (2015) 44905.

[16] R.S. Kim, F.S. LaBella, Comparison of analytical methods for monitoring autoxidation profiles of authentic lipids., J. Lipid Res. 28 (1987) 1110–1117.

[17] W. Rawicz, K.C. Olbrich, T. McIntosh, D. Needham, E. Evans, Effect of Chain Length and Unsaturation on Elasticity of Lipid Bilayers, Biophys. J. 79 (2000) 328–339.

[18] https://avantilipids.com/product-category/products/fluorescent-lipids/.

[19] https://www.thermofisher.com/content/dam/LifeTech/global/technical-reference-library/Molecular%20Probes%20Handbook/chapter-pdfs/Ch-13-Lipid-Membrane-Probes.pdf?icid=WE216841.

[20] D.W. Piston, G.-J. Kremers, Fluorescent protein FRET: the good, the bad and the ugly, Trends Biochem. Sci. 32 (2007) 407–414.

[21] R. Roy, S. Hohng, T. Ha, A practical guide to single-molecule FRET, Nat. Methods. 5 (2008) 507–516.

[22] M. Amaro, R. Šachl, P. Jurkiewicz, A. Coutinho, M. Prieto, M. Hof, Time-Resolved Fluorescence in Lipid Bilayers: Selected Applications and Advantages over Steady State, Biophys. J. 107 (2014) 2751–2760.

[23] N. Kahya, P. Schwille, Fluorescence correlation studies of lipid domains in model membranes (Review), Mol. Membr. Biol. 23 (2006) 29–39.

[24] Y. Chen, B.C. Lagerholm, B. Yang, K. Jacobson, Methods to measure the lateral diffusion of membrane lipids and proteins, Methods. 39 (2006) 147–153.

[25] C. Reichardt, Solvatochromic Dyes as Solvent Polarity Indicators, Chem. Rev. 94 (1994) 2319–2358.

[26] A. Marini, A. Muñoz-Losa, A. Biancardi, B. Mennucci, What is Solvatochromism?, J. Phys. Chem. B. 114 (2010) 17128–17135.

[27] Z. Arsov, L. Quaroni, Detection of lipid phase coexistence and lipid interactions in sphingomyelin/cholesterol membranes by ATR-FTIR spectroscopy, Biochim. Biophys. Acta - Biomembr. 1778 (2008) 880–889.

[28] R.N.A.H. Lewis, R.N. McElhaney, Membrane lipid phase transitions and phase organization studied by Fourier transform infrared spectroscopy, Biochim. Biophys. Acta - Biomembr. 1828 (2013) 2347–2358.

[29] M.C. Hull, L.R. Cambrea, J.S. Hovis, Infrared Spectroscopy of Fluid Lipid Bilayers, Anal. Chem. 77 (2005) 6096–6099.

[30] I.W. Levin, E. Mushayakarara, R. Bittman, Vibrational assignment of the sn-1 and sn-2 chain carbonyl stretching modes of membrane phospholipids, J. Raman Spectrosc. 13 (1982) 231–234.

[31] C. Lee, C.D. Bain, Raman spectra of planar supported lipid bilayers, Biochim. Biophys. Acta - Biomembr. 1711 (2005) 59–71.

[32] M.J.L. de Lange, M. Bonn, M. Müller, Direct measurement of phase coexistence in DPPC/cholesterol vesicles using Raman spectroscopy, Chem. Phys. Lipids. 146 (2007) 76–84.

[33] K. Czamara, K. Majzner, M.Z. Pacia, K. Kochan, A. Kaczor, M. Baranska, Raman spectroscopy of lipids: a review, J. Raman Spectrosc. 46 (2015) 4–20.

[34] R.N. McElhaney, The use of differential scanning calorimetry and differential thermal analysis in studies of model and biological membranes, Chem. Phys. Lipids. 30 (1982) 229–259.

[35] J. Seelig, Thermodynamics of lipid–peptide interactions, Biochim. Biophys. Acta - Biomembr. 1666 (2004) 40–50.

[36] S. Perspicace, A.C. Rufer, R. Thoma, F. Mueller, M. Hennig, S. Ceccarelli, T. Schulz-Gasch, J. Seelig, Isothermal titration calorimetry with micelles: Thermodynamics of inhibitor binding to carnitine palmitoyltransferase 2 membrane protein, FEBS Open Bio. 3 (2013) 204–211.

[37] A. Ziegler, X. Li Blatter, A. Seelig, J. Seelig, Protein transduction domains of HIV-1 and SIV TAT interact with charged lipid vesicles. Binding mechanism and thermodynamic analysis, Biochemistry. 42 (2003) 9185–9194.

[38] D. Marsh, Thermodynamics of Phospholipid Self-Assembly, Biophys. J. 102 (2012) 1079–1087.

[39] E. Gmelin, Classical temperature-modulated calorimetry: A review, Thermochim. Acta. 304–305 (1997) 1–26.

[40] E. Verdonck, K. Schaap, L.C. Thomas, A discussion of the principles and applications of Modulated Temperature DSC (MTDSC), Int. J. Pharm. 192 (1999) 3–20.

[41] C. Svanberg, P. Berntsen, A. Johansson, T. Hedlund, E. Axén, J. Swenson, Structural relaxations of phospholipids and water in planar membranes, J. Chem. Phys. 130 (2009) 035101.

[42] E. Gorter, On Bimolecular layers of Lipoids on the Chromocytes of the blood, J. Exp. Med. 41 (1925) 439–443.

[43] J.F. Danielli, H. Davson, A contribution to the theory of permeability of thin films, J. Cell. Comp. Physiol. 5 (1935) 495–508.

[44] R.S. Bear, K.J. Palmer, F.O. Schmitt, X-ray diffraction studies of nerve lipides, J. Cell. Comp. Physiol. 17 (1941) 355–367.

[45] K.J. Palmer, F.O. Schmitt, X-ray diffraction studies of lipide emulsions, J. Cell. Comp. Physiol. 17 (1941) 385–394.

[46] A.D. Bangham, Lipid Bilayers and Biomembranes, Annu. Rev. Biochem. 41 (1972) 753–

776.

[47] F. Szoka, D. Papahadjopoulos, Comparative Properties and Methods of Preparation of Lipid Vesicles (Liposomes), Annu. Rev. Biophys. Bioeng. 9 (1980) 467–508.

[48] T.M. Allen, P.R. Cullis, Liposomal drug delivery systems: From concept to clinical applications, Adv. Drug Deliv. Rev. 65 (2013) 36–48.

[49] B.S. Pattni, V. V. Chupin, V.P. Torchilin, New Developments in Liposomal Drug Delivery, Chem. Rev. 115 (2015) 10938–10966.

[50] J.N. Israelachvili, D.J. Mitchell, B.W. Ninham, Theory of self-assembly of lipid bilayers and vesicles, Biochim. Biophys. Acta - Biomembr. 470 (1977) 185–201.

[51] J. Israelachvili, Intermolecular and Surface Forces, Elsevier Inc., 2011.

[52] M.J. Janiak, D.M. Small, G.G. Shipley, Temperature and compositional dependence of the structure of hydrated dimyristoyl lecithin, J. Biol. Chem. 254 (1979) 6068–6078.

[53] D.M. LeNeveu, R.P. Rand, Measurement and modification of forces between lecithin bilayers, Biophys. J. 18 (1977) 209–230.

[54] H. Hauser, F. Paltauf, G.G. Shipley, Structure and thermotropic behavior of phosphatidylserine bilayer membranes, Biochemistry. 21 (1982) 1061–1067.

[55] E. Amado, J. Kressler, Interactions of amphiphilic block copolymers with lipid model membranes, Curr. Opin. Colloid Interface Sci. 16 (2011) 491–498.

[56] H. Hauser, Some aspects of the phase behaviour of charged lipids, Biochim. Biophys. Acta - Biomembr. 772 (1984) 37–50.

[57] D. Atkinson, H. Hauser, G.G. Shipley, J.M. Stubbs, Structure and morphology of phosphatidylserine dispersions, Biochim. Biophys. Acta - Biomembr. 339 (1974) 10–29.

[58] A.D. Bangham, A Correlation between Surface Charge and Coagulant Action of Phospholipids, Nature. 192 (1961) 1197–1198.

[59] A.D. Bangham, R.W. Horne, Negative staining of phospholipids and their structural modification by surface-active agents as observed in the electron microscope, J. Mol. Biol. 8 (1964) 660–668.

[60]   A.D. Bangham, M.M. Standish, J.C. Watkins, Diffusion of univalent ions across the lamellae of swollen phospholipids, J. Mol. Biol. 13 (1965) 238–252.

[61]   L. Saunders, J. Perrin, D. Gammack, Ultrasonic irradiation of some phospholipid sols, J. Pharm. Pharmacol. 14 (1962) 567–572.

[62]   Y. Barenholzt, S. Amselem, L. D., A new method for preparation of phospholipid vesicles (liposomes) - french press, FEBS Lett. 99 (1979) 210–214.

[63]   R.L. Hamilton, J. Goerke, L.S. Guo, M.C. Williams, R.J. Havel, Unilamellar liposomes made with the French pressure cell: a simple preparative and semiquantitative technique., J. Lipid Res. 21 (1980) 981–992.

[64]   F. Olson, C.A. Hunt, F.C. Szoka, W.J. Vail, D. Papahadjopoulos, Preparation of liposomes of defined size distribution by extrusion through polycarbonate membranes, Biochim. Biophys. Acta - Biomembr. 557 (1979) 9–23.

[65]   S. Batzri, E.D. Korn, Single bilayer liposomes prepared without sonication, Biochim. Biophys. Acta - Biomembr. 298 (1973) 1015–1019.

[66]   D. Deamer, A.D. Bangham, Large volume liposomes by an ether vaporization method, Biochim. Biophys. Acta - Biomembr. 443 (1976) 629–634.

[67]   F. Szoka, D. Papahadjopoulos, Procedure for preparation of liposomes with large internal aqueous space and high capture by reverse-phase evaporation., Proc. Natl. Acad. Sci. 75 (1978) 4194–4198.

[68]   H.C. Shum, D. Lee, I. Yoon, T. Kodger, D.A. Weitz, Double Emulsion Templated Monodisperse Phospholipid Vesicles, Langmuir. 24 (2008) 7651–7653.

[69]   G. Strauss, H. Hauser, Stabilization of lipid bilayer vesicles by sucrose during freezing, Proc. Natl. Acad. Sci. 83 (1986) 2422–2426.

[70]   H. Hauser, G. Strauss, Stabilization of small unilamellar phospholipid vesicles during spray-drying, Biochim. Biophys. Acta - Biomembr. 897 (1987) 331–334.

[71]   A. Alonso, A. Villena, F.M. Goñi, Lysis and reassembly of sonicated lecithin vesicles in the presence of triton X-100, FEBS Lett. 123 (1981) 200–204.

[72] J. Suurkuusk, B.R. Lentz, Y. Barenholz, R.L. Biltonen, T.E. Thompson, A calorimetric and fluorescent probe study of the gel-liquid crystalline phase transition in small, single-lamellar dipalmitoylphosphatidylcholine vesicles, Biochemistry. 15 (1976) 1393–1401.

[73] B. Gruenewald, S. Stankowski, A. Blume, Curvature influence on the cooperativity and the phase transition enthalpy of lecithin vesicles, FEBS Lett. 102 (1979) 227–229.

[74] M.I. Angelova, D.S. Dimitrov, Liposome electroformation, Faraday Discuss. Chem. Soc. 81 (1986) 303–311.

[75] D.J. Estes, M. Mayer, Giant liposomes in physiological buffer using electroformation in a flow chamber, Biochim. Biophys. Acta - Biomembr. 1712 (2005) 152–160.

[76] D.J. Estes, M. Mayer, Electroformation of giant liposomes from spin-coated films of lipids, Colloids Surfaces B Biointerfaces. 42 (2005) 115–123.

[77] T. Pott, H. Bouvrais, P. Méléard, Giant unilamellar vesicle formation under physiologically relevant conditions, Chem. Phys. Lipids. 154 (2008) 115–119.

[78] N.F. Morales-Penningston, J. Wu, E.R. Farkas, S.L. Goh, T.M. Konyakhina, J.Y. Zheng, W.W. Webb, G.W. Feigenson, GUV preparation and imaging: Minimizing artifacts, Biochim. Biophys. Acta - Biomembr. 1798 (2010) 1324–1332.

[79] T.J. Politano, V.E. Froude, B. Jing, Y. Zhu, AC-electric field dependent electroformation of giant lipid vesicles, Colloids Surfaces B Biointerfaces. 79 (2010) 75–82.

[80] C. Herold, G. Chwastek, P. Schwille, E.P. Petrov, Efficient Electroformation of Supergiant Unilamellar Vesicles Containing Cationic Lipids on ITO-Coated Electrodes, Langmuir. 28 (2012) 5518–5521.

[81] H.-J. Lehmler, Synthesis of environmentally relevant fluorinated surfactants—a review, Chemosphere. 58 (2005) 1471–1496.

[82] P. Kirsch, Modern Fluoroorganic Chemistry: Synthesis, Reactivity, Applications, Wiley-VCH, Weinheim, 2013.

[83] J.H. Simons, L.P. Block, Fluorocarbons. The Reaction of Fluorine with Carbon, J. Am. Chem. Soc. 61 (1939) 2962–2966.

[84] A. Borodine, Ueber Bromvaleriansäure und Brombuttersäure, Ann. Der Chemie Und Pharm. 119 (1861) 121–123.

[85] H. Hunsdiecker, C. Hunsdiecker, Über den Abbau der Salze aliphatischer Säuren durch Brom, Berichte Der Deutsch. Chem. Gesellschaft. 75 (1942) 291–297.

[86] R.G. Johnson, R.K. Ingham, The Degradation Of Carboxylic Acid Salts By Means Of Halogen - The Hunsdiecker Reaction, Chem. Rev. 56 (1956) 219–269.

[87] H.J. Emeléus, R.N. Haszeldine, 623. Organometallic fluorine compounds. Part I. The synthesis of trifluoromethyl and pentafluoroethyl mercurials, J. Chem. Soc. (1949) 2948–2952.

[88] R.N. Haszeldine, 603. The reactions of fluorocarbon radicals. Part I. The reaction of iodotrifluoromethane with ethylene and tetrafluoroethylene, J. Chem. Soc. (1949) 2856–2861.

[89] J. Balague, B. Ameduri, B. Boutevin, G. Caporiccio, Synthesis of fluorinated telomers. Part 1. Telomerization of vinylidene fluoride with perfluoroalkyl iodides, J. Fluor. Chem. 70 (1995) 215–223.

[90] R.N. Haszeldine, 769. Reactions of fluorocarbon radicals. Part XII. The synthesis of fluorocarbons and of fully fluorinated iodo-, bromo-, and chloroalkanes, J. Chem. Soc. 1 (1953) 3761–3768.

[91] F. Jeanneaux, M. Le Blanc, A. Cambon, J. Guion, Addition thermique des iodo-1-perfluoroalcanes sur les perfluoroalkylethylenes, J. Fluor. Chem. 4 (1974) 261–270.

[92] Z. Qiu, D.J. Burton, Reaction of Perfluoroalkyl Iodides with Electron-Deficient Olefins under UV Irradiation, J. Org. Chem. 60 (1995) 3465–3472.

[93] G.V.D. Tiers, Perfluoroalkylation of aromatic compounds, J. Am. Chem. Soc. 82 (1960) 5513–5513.

[94] A.B. Cowell, C. Tamborski, Fluoroalkylation of aromatic compounds, J. Fluor. Chem. 17 (1981) 345–356.

[95] H. Blancou, S. Benefice, A. Commeyras, Methode quantitative pour la preparation de

perfluoroalcoyl-ethanol RFCH2CH2OH a partir de perfluoroalcoyl-2 iodo-1 ethane RFCH2CH2I. (RF = CnF2n+1, n pair), J. Fluor. Chem. 23 (1983) 57–65.

[96] P.V. Ramachandran, M.P. Jennings, H.C. Brown, Critical Role of Catalysts and Boranes for Controlling the Regioselectivity in the Rhodium-Catalyzed Hydroboration of Fluoroolefins, Org. Lett. 1 (1999) 1399–1402.

[97] P.V. Ramachandran, M.P. Jennings, Investigation of the factors controlling the regioselectivity of the hydroboration of fluoroolefins, Chem. Commun. 11 (2002) 386–387.

[98] N.O. Brace, L.W. Marshall, C.J. Pinson, G. Van Wingerden, Effect of a perfluoroalkyl group on the elimination and substitution reactions of two homologous series of perfluoroalkyl-substituted iodoalkanes, J. Org. Chem. 49 (1984) 2361–2368.

[99] E. Kissa, Fluorinated surfactants and repellents, CRC Press, 2001.

[100] C. Selve, B. Castro, P. Leempoel, G. Mathis, T. Gartiser, J.-J. Delpuech, Synthesis of homogeneous polyoxyethylene perfluorcalkyl surfactants, Tetrahedron. 39 (1983) 1313–1316.

[101] V.I. Furdui, N.L. Stock, D.A. Ellis, C.M. Butt, D.M. Whittle, P.W. Crozier, E.J. Reiner, D.C.G. Muir, S.A. Mabury, Spatial Distribution of Perfluoroalkyl Contaminants in Lake Trout from the Great Lakes, Environ. Sci. Technol. 41 (2007) 1554–1559.

[102] M.J.A. Dinglasan-Panlilio, S.A. Mabury, Significant residual fluorinated alcohols present in various fluorinated materials, Environ. Sci. Technol. 40 (2006) 1447–1453.

[103] J. Verreault, M. Houde, G.W. Gabrielsen, U. Berger, M. Haukås, R.J. Letcher, D.C.G. Muir, Perfluorinated Alkyl Substances in Plasma, Liver, Brain, and Eggs of Glaucous Gulls (Larus hyperboreus) from the Norwegian Arctic, Environ. Sci. Technol. 39 (2005) 7439–7445.

[104] D. Trudel, L. Horowitz, M. Wormuth, M. Scheringer, I.T. Cousins, K. Hungerbühler, Estimating Consumer Exposure to PFOS and PFOA, Risk Anal. 28 (2008) 251–269.

[105] K. Prevedouros, I.T. Cousins, R.C. Buck, S.H. Korzeniowski, Sources, Fate and Transport of Perfluorocarboxylates, Environ. Sci. Technol. 40 (2006) 32–44.

[106] J. Liu, L.S. Lee, Solubility and Sorption by Soils of 8:2 Fluorotelomer Alcohol in Water and

Cosolvent Systems, Environ. Sci. Technol. 39 (2005) 7535–7540.

[107] W.J. Fasano, Absorption, Distribution, Metabolism, and Elimination of 8-2 Fluorotelomer Alcohol in the Rat, Toxicol. Sci. 91 (2006) 341–355.

[108] H. Ishibashi, R. Yamauchi, M. Matsuoka, J.-W. Kim, M. Hirano, A. Yamaguchi, N. Tominaga, K. Arizono, Fluorotelomer alcohols induce hepatic vitellogenin through activation of the estrogen receptor in male medaka (*Oryzias latipes*), Chemosphere. 71 (2008) 1853–1859.

[109] W.J. Fasano, L.M. Sweeney, M.P. Mawn, D.L. Nabb, B. Szostek, R.C. Buck, M.L. Gargas, Kinetics of 8-2 fluorotelomer alcohol and its metabolites, and liver glutathione status following daily oral dosing for 45 days in male and female rats, Chem. Biol. Interact. 180 (2009) 281–295.

[110] C.M. Butt, U. Berger, R. Bossi, G.T. Tomy, Levels and trends of poly- and perfluorinated compounds in the arctic environment, Sci. Total Environ. 408 (2010) 2936–2965.

[111] K. Dasu, L.A. Royer, J. Liu, L.S. Lee, Hydrolysis of fluorotelomer compounds leading to fluorotelomer alcohol production during solvent extractions of soils, Chemosphere. 81 (2010) 911–917.

[112] K. Dasu, L.S. Lee, R.F. Turco, L.F. Nies, Aerobic biodegradation of 8:2 fluorotelomer stearate monoester and 8:2 fluorotelomer citrate triester in forest soil, Chemosphere. 91 (2013) 399–405.

[113] G.B. Post, P.D. Cohn, K.R. Cooper, Perfluorooctanoic acid (PFOA), an emerging drinking water contaminant: A critical review of recent literature, Environ. Res. 116 (2012) 93–117.

[114] Z.-M. Li, L.-H. Guo, X.-M. Ren, Biotransformation of 8:2 fluorotelomer alcohol by recombinant human cytochrome P450s, human liver microsomes and human liver cytosol, Environ. Sci. Process. Impacts. 18 (2016) 538–546.

[115] A.M. Calafat, L.-Y. Wong, Z. Kuklenyik, J.A. Reidy, L.L. Needham, Polyfluoroalkyl Chemicals in the U.S. Population: Data from the National Health and Nutrition Examination Survey (NHANES) 2003–2004 and Comparisons with NHANES 1999–2000, Environ. Health Perspect. 115 (2007) 1596–1602.

[116] B.J. Apelberg, F.R. Witter, J.B. Herbstman, A.M. Calafat, R.U. Halden, L.L. Needham, L.R. Goldman, Cord Serum Concentrations of Perfluorooctane Sulfonate (PFOS) and Perfluorooctanoate (PFOA) in Relation to Weight and Size at Birth, Environ. Health Perspect. 115 (2007) 1670–1676.

[117] C. Fei, J.K. McLaughlin, R.E. Tarone, J. Olsen, Fetal Growth Indicators and Perfluorinated Chemicals: A Study in the Danish National Birth Cohort, Am. J. Epidemiol. 168 (2008) 66–72.

[118] J. Liu, L.S. Lee, L.F. Nies, C.H. Nakatsu, R.F. Turco, Biotransformation of 8:2 Fluorotelomer Alcohol in Soil and by Soil Bacteria Isolates, Environ. Sci. Technol. 41 (2007) 8024–8030.

[119] M.A. Kaiser, D.P. Cobranchi, C.-P. Chai Kao, P.J. Krusic, A.A. Marchione, R.C. Buck, Physicochemical Properties of 8-2 Fluorinated Telomer B Alcohol, J. Chem. Eng. Data. 49 (2004) 912–916.

[120] C.-H. Yang, K.P. Glover, X. Han, Characterization of Cellular Uptake of Perfluorooctanoate via Organic Anion-Transporting Polypeptide 1A2, Organic Anion Transporter 4, and Urate Transporter 1 for Their Potential Roles in Mediating Human Renal Reabsorption of Perfluorocarboxylates, Toxicol. Sci. 117 (2010) 294–302.

[121] S.-C. Chang, K. Das, D.J. Ehresman, M.E. Ellefson, G.S. Gorman, J. a Hart, P.E. Noker, Y.-M. Tan, P.H. Lieder, C. Lau, G.W. Olsen, J.L. Butenhoff, Comparative Pharmacokinetics of Perfluorobutyrate in Rats, Mice, Monkeys, and Humans and Relevance to Human Exposure via Drinking Water, Toxicol. Sci. 104 (2008) 40–53.

[122] J.M. Conder, R. a Hoke, W. De Wolf, M.H. Russell, R.C. Buck, Are PFCAs Bioaccumulative? A Critical Review and Comparison with Regulatory Criteria and Persistent Lipophilic Compounds, Environ. Sci. Technol. 42 (2008) 995–1003.

[123] J.W. Martin, S. a Mabury, K.R. Solomon, D.C.G. Muir, Dietary accumulation of perfluorinated acids in juvenile rainbow trout (*Oncorhynchus Mykiss*), Environ. Toxicol. Chem. 22 (2003) 189–195.

[124] J.W. Martin, S. a Mabury, K.R. Solomon, D.C.G. Muir, Bioconcentration and tissue distribution of perfluorinated acids in rainbow trout (*Oncorhynchus Mykiss*), Environ.

Toxicol. Chem. 22 (2003) 196–204.

[125] C.P. Chengelis, J.B. Kirkpatrick, N.R. Myers, M. Shinohara, P.L. Stetson, D.W. Sved, Comparison of the toxicokinetic behavior of perfluorohexanoic acid (PFHxA) and nonafluorobutane-1-sulfonic acid (PFBS) in cynomolgus monkeys and rats, Reprod. Toxicol. 27 (2009) 400–406.

[126] S.A. Gannon, T. Johnson, D.L. Nabb, T.L. Serex, R.C. Buck, S.E. Loveless, Absorption, distribution, metabolism, and excretion of [1-14C]-perfluorohexanoate ([14C]-PFHx) in rats and mice, Toxicology. 283 (2011) 55–62.

[127] T. Serex, S. Anand, S. Munley, E.M. Donner, S.R. Frame, R.C. Buck, S.E. Loveless, Toxicological evaluation of 6:2 fluorotelomer alcohol, Toxicology. 319 (2014) 1–9.

[128] J.C. O'Connor, S.M. Munley, T.L. Serex, R.C. Buck, Evaluation of the reproductive and developmental toxicity of 6:2 fluorotelomer alcohol in rats, Toxicology. 317 (2014) 6–16.

[129] M.H. Russell, M.W. Himmelstein, R.C. Buck, Inhalation and oral toxicokinetics of 6:2 FTOH and its metabolites in mammals, Chemosphere. 120 (2015) 328–335.

[130] J.E. Klaunig, M. Shinohara, H. Iwai, C.P. Chengelis, J.B. Kirkpatrick, Z. Wang, R.H. Bruner, Evaluation of the Chronic Toxicity and Carcinogenicity of Perfluorohexanoic Acid (PFHxA) in Sprague-Dawley Rats, Toxicol. Pathol. 43 (2015) 209–220.

[131] P. Mukerji, J.C. Rae, R.C. Buck, J.C. O'Connor, Oral repeated-dose systemic and reproductive toxicity of 6:2 fluorotelomer alcohol in mice, Toxicol. Reports. 2 (2015) 130–143.

[132] M.H. Kim, N. Wang, K.H. Chu, 6:2 Fluorotelomer alcohol (6:2 FTOH) biodegradation by multiple microbial species under different physiological conditions, Appl. Microbiol. Biotechnol. 98 (2014) 1831–1840.

[133] H. Harms, D. Schlosser, L.Y. Wick, Untapped potential: exploiting fungi in bioremediation of hazardous chemicals, Nat. Rev. Microbiol. 9 (2011) 177–192.

[134] N. Tseng, N. Wang, B. Szostek, S. Mahendra, Biotransformation of 6:2 Fluorotelomer Alcohol (6:2 FTOH) by a Wood-Rotting Fungus, Environ. Sci. Technol. 48 (2014) 4012–4020.

[135] I.T. Horváth, J. Rábai, Facile Catalyst Separation Without Water: Fluorous Biphase Hydroformylation of Olefins, Science. 266 (1994) 72–75.

[136] J. Gladysz, D. Curran, I. Horváth, Handbook of Fluorous Chemistry, Wiley-VCH, Weinheim, 2004.

[137] J.J.J. Juliette, J.A. Gladysz, I.T. Horváth, Transition Metal Catalysis in Fluorous Media: Practical Application of a New Immobilization Principle to Rhodium-Catalyzed Hydroboration, Angew. Chemie Int. Ed. English. 36 (1997) 1610–1612.

[138] W. Zhang, Fluorous synthesis of heterocyclic systems., Chem. Rev. 104 (2004) 2531–56.

[139] W. Zhang, D.P. Curran, Synthetic applications of fluorous solid-phase extraction (F-SPE), Tetrahedron. 62 (2006) 11837–11865.

[140] D.P. Curran, Z. Luo, Fluorous Synthesis with Fewer Fluorines (Light Fluorous Synthesis): Separation of Tagged from Untagged Products by Solid-Phase Extraction with Fluorous Reverse-Phase Silica Gel, J. Am. Chem. Soc. 121 (1999) 9069–9072.

[141] M. Matsugi, K. Yamanaka, I. Inomata, N. Takekoshi, M. Hasegawa, D.P. Curran, Synthesis of Fluorous-FMOC Reagents and Purification of Protected Dipeptides with Fluorous Solid Phase Extraction, QSAR Comb. Sci. 25 (2006) 713–715.

[142] W. Zhang, C. Cai, New chemical and biological applications of fluorous technologies., Chem. Commun. (Camb). (2008) 5686–94.

[143] W. Zhang, Fluorocarbon stationary phases for liquid chromatography applications, J. Fluor. Chem. 129 (2008) 910–919.

[144] H.-J. Lehmler, S. Telu, S.M. Vyas, N.S. Shaikh, S.E. Rankin, B.L. Knutson, S. Parkin, Synthesis and Solid State Structure of Fluorous Probe Molecules for Fluorous Separation Applications., Tetrahedron. 66 (2010) 2561–2569.

[145] D.K. Kölmel, B. Rudat, D.M. Braun, C. Bednarek, U. Schepers, S. Bräse, Rhodamine F: a novel class of fluorous ponytailed dyes for bioconjugation, Org. Biomol. Chem. 11 (2013) 3954.

[146] L.E. Kiss, I. Kövesdi, J. Rábai, An improved design of fluorophilic molecules: Prediction of

the ln P fluorous partition coefficient, fluorophilicity, using 3D QSAR descriptors and neural networks, J. Fluor. Chem. 108 (2001) 95–109.

[147] F.T.T. Huque, K. Jones, R.A. Saunders, J.A. Platts, Statistical and theoretical studies of fluorophilicity, J. Fluor. Chem. 115 (2002) 119–128.

[148] S.M. Daniels, R. a. Saunders, J. a. Platts, Prediction of fluorophilicity of organic and transition metal compounds using molecular surface areas, J. Fluor. Chem. 125 (2004) 1291–1298.

[149] G.-X. Hu, J.-W. Zou, M. Zeng, S.-F. Pan, Q.-S. Yu, 2D and 3D-QSPR Models for the Fluorophilicity of Organic Compounds in Consideration of Chirality, QSAR Comb. Sci. 28 (2009) 1112–1122.

[150] J. Wang, M. Sánchez-Roselló, J.L. Aceña, C. del Pozo, A.E. Sorochinsky, S. Fustero, V.A. Soloshonok, H. Liu, Fluorine in Pharmaceutical Industry: Fluorine-Containing Drugs Introduced to the Market in the Last Decade (2001–2011), Chem. Rev. 114 (2014) 2432–2506.

[151] M. Salwiczek, E.K. Nyakatura, U.I.M. Gerling, S. Ye, B. Koksch, Fluorinated amino acids: compatibility with native protein structures and effects on protein–protein interactions, Chem. Soc. Rev. 41 (2012) 2135–2171.

[152] J. Sangster, Octanol-Water Partition Coefficients of Simple Organic Compounds, J. Phys. Chem. Ref. Data. 18 (1989) 1111–1229.

[153] M.H. Abraham, H.S. Chadha, G.S. Whiting, R.C. Mitchell, Hydrogen Bonding. 32. An Analysis of Water-Octanol and Water-Alkane Partitioning and the Δlog P Parameter of Seiler, J. Pharm. Sci. 83 (1994) 1085–1100.

[154] N. Bodor, P. Buchwald, Recent advances in the brain targeting of neuropharmaceuticals by chemical delivery systems, Adv. Drug Deliv. Rev. 36 (1999) 229–254.

[155] P. Jing, P.J. Rodgers, S. Amemiya, High Lipophilicity of Perfluoroalkyl Carboxylate and Sulfonate: Implications for Their Membrane Permeability, J. Am. Chem. Soc. 131 (2009) 2290–2296.

[156] B.E. Smart, Fluorine substituent effects (on bioactivity), J. Fluor. Chem. 109 (2001) 3–11.

[157] M. Sauer, J. Hofkens, J. Enderlein, Handbook of Fluorescence Spectroscopy and Imaging, Wiley-VCH, Weinheim, 2011, pp 1–30.

[158] A. Jabłoński, Über den Mechanismus der Photolumineszenz von Farbstoffphosphoren, Zeitschrift Für Phys. 94 (1935) 38–46.

[159] http://www.olympusmicro.com/primer/techniques/confocal/images/fluorescenceintrofigure1.jpg.

[160] J. Franck, E.G. Dymond, Elementary processes of photochemical reactions, Trans. Faraday Soc. 21 (1926) 536–542.

[161] E. Condon, A Theory of Intensity Distribution in Band Systems, Phys. Rev. 28 (1926) 1182–1201.

[162] E.U. Condon, Nuclear Motions Associated with Electron Transitions in Diatomic Molecules, Phys. Rev. 32 (1928) 858–872.

[163] Franck–Condon principle, IUPAC Compend. Chem. Terminol., (2014) 2510. doi: 10.1351/goldbook.F02510.

[164] J. Lakowicz, Principles of Fluorescence Spectroscopy, Boston, 2006.

[165] É. V Shpol'skiǐ, Problems of the origin and structure of the quasilinear spectra of organic compounds at low temperatures, Sov. Phys. Uspekhi. 5 (1962) 522–531.

[166] A. V. Naumov, Low-temperature spectroscopy of organic molecules in solid matrices: from the Shpol'skii effect to laser luminescent spectromicroscopy for all effectively emitting single molecules, Physics-Uspekhi. 56 (2013) 605–622.

[167] M. Maroncelli, G.R. Fleming, Picosecond solvation dynamics of coumarin 153: The importance of molecular aspects of solvation, J. Chem. Phys. 86 (1987) 6221–6239.

[168] W. Jarzeba, G.C. Walker, A.E. Johnson, M.A. Kahlow, P.F. Barbara, Femtosecond microscopic solvation dynamics of aqueous solutions, J. Phys. Chem. 92 (1988) 7039–7041.

[169] M. Maroncelli, J. Macinnis, G.R. Fleming, Polar Solvent Dynamics and Electron-Transfer Reactions, Science. 243 (1989) 1674–1681.

[170] W. Jarzeba, G.C. Walker, A.E. Johnson, P.F. Barbara, Nonexponential solvation dynamics

of simple liquids and mixtures, Chem. Phys. 152 (1991) 57–68.

[171] E. Åkesson, G.C. Walker, P.F. Barbara, Dynamic solvent effects on electron transfer rates in the inverted regime: Ultrafast studies on the betaines, J. Chem. Phys. 95 (1991) 4188–4194.

[172] Y. Jiang, P.K. McCarthy, G.J. Blanchard, The role of multiple electronic states in the dissipative energy dynamics of coumarin 153, Chem. Phys. 183 (1994) 249–267.

[173] P. Suppan, Invited review solvatochromic shifts: The influence of the medium on the energy of electronic states, J. Photochem. Photobiol. A Chem. 50 (1990) 293–330.

[174] C. Reichardt, Solvents and Solvent Effects in Organic Chemistry, Wiley-VCH, Weinheim, 2003.

[175] N. Mataga, Y. Kaifu, M. Koizumi, Solvent Effects upon Fluorescence Spectra and the Dipolemoments of Excited Molecules, Bull. Chem. Soc. Jpn. 29 (1956) 465–470.

[176] G.A. Crosby, J.N. Demas, Measurement of photoluminescence quantum yields. Review, J. Phys. Chem. 75 (1971) 991–1024.

[177] M. Long, R. Swofford, A. Albrecht, Thermal lens technique: a new method of absorption spectroscopy, Science. 191 (1976) 183–185.

[178] A.J. Twarowski, D.S. Kliger, Multiphoton absorption spectra using thermal blooming, Chem. Phys. 20 (1977) 259–264.

[179] J.H. Brannon, D. Magde, Absolute quantum yield determination by thermal blooming. Fluorescein, J. Phys. Chem. 82 (1978) 705–709.

[180] C. Würth, M. Grabolle, J. Pauli, M. Spieles, U. Resch-Genger, Comparison of methods and achievable uncertainties for the relative and absolute measurement of photoluminescence quantum yields., Anal. Chem. 83 (2011) 3431–9.

[181] C. Würth, M. Grabolle, J. Pauli, M. Spieles, U. Resch-Genger, Relative and absolute determination of fluorescence quantum yields of transparent samples, Nat. Protoc. 8 (2013) 1535–1550.

[182] R. Price, W. Jerome, Basic Confocal Microscopy, Springer, New York, 2011.

[183] J.G. White, An evaluation of confocal versus conventional imaging of biological structures by fluorescence light microscopy, J. Cell Biol. 105 (1987) 41–48.

[184] M.D. Egger, M. Petran, New Reflected-Light Microscope for Viewing Unstained Brain and Ganglion Cells, Science. 157 (1967) 305–307.

[185] M. Petráň, M. Hadravský, M.D. Egger, R. Galambos, Tandem-Scanning Reflected-Light Microscope, J. Opt. Soc. Am. 58 (1968) 661.

[186] Lord Rayleigh, Measurements of the Amount of Oil Necessary in Order to Check the Motions of Camphor upon Water, Proc. R. Soc. London. 47 (1889) 364–367.

[187] A. Pockels, Untersuchung von Grenzflächenspannungen mit der Cohäsionswaage, Ann. Der Phys. Und Chemie. 303 (1899) 668–681.

[188] A. Pockels, Ueber das spontane Sinken der Oberflächenspannung von Wasser, wässerigen Lösungen und Emulsionen, Ann. Phys. 313 (1902) 854–871.

[189] I. Langmuir, The constitution and fundamental properties of solids and liquids. II. Liquids, J. Am. Chem. Soc. 39 (1917) 1848–1906.

[190] I. Langmuir, The mechanism of the surface phenomena of flotation, Trans. Faraday Soc. 15 (1920) 62–74.

[191] K.B. Blodgett, Films Built by Depositing Successive Monomolecular Layers on a Solid Surface, J. Am. Chem. Soc. 57 (1935) 1007–1022.

[192] P. Dynarowicz-Łątka, A. Dhanabalan, O.N. Oliveira, Modern physicochemical research on Langmuir monolayers, Adv. Colloid Interface Sci. 91 (2001) 221–293.

[193] V. Kaganer, H. Möhwald, P. Dutta, Structure and phase transitions in Langmuir monolayers, Rev. Mod. Phys. 71 (1999) 779–819.

[194] C. Knobler, Phase Transitions in Monolayers, Annu. Rev. Phys. Chem. 43 (1992) 207–236.

[195] H. Mohwald, Phospholipid and Phospholipid-Protein Monolayers at the Air/Water Interface, Annu. Rev. Phys. Chem. 41 (1990) 441–476.

[196] R.M. Weis, Fluorescence microscopy of phospholipid monolayer phase transitions, Chem. Phys. Lipids. 57 (1991) 227–239.

[197] M. Gudmand, M. Fidorra, T. Bjørnholm, T. Heimburg, Diffusion and Partitioning of Fluorescent Lipid Probes in Phospholipid Monolayers, Biophys. J. 96 (2009) 4598–4609.

[198] A.F. Eftaiha, S.M.K. Brunet, M.F. Paige, Influence of Film Composition on the Morphology, Mechanical Properties, and Surfactant Recovery of Phase-Separated Phospholipid-Perfluorinated Fatty Acid Mixed Monolayers, Langmuir. 28 (2012) 15150–15159.

[199] P. Scholtysek, Z. Li, J. Kressler, A. Blume, Interactions of DPPC with semitelechelic poly(glycerol methacrylate)s with perfluoroalkyl end groups., Langmuir. 28 (2012) 15651–62.

[200] P. Scholtysek, S.W.H. Shah, S.S. Müller, R. Schöps, H. Frey, A. Blume, J. Kressler, Unusual triskelion patterns and dye-labelled GUVs: consequences of the interaction of cholesterol-containing linear-hyperbranched block copolymers with phospholipids, Soft Matter. 11 (2015) 6106–6117.

[201] J.W. Lichtman, J.-A. Conchello, Fluorescence microscopy, Nat. Methods. 2 (2005) 910–919.

[202] G.Y. Mitronova, V.N. Belov, M.L. Bossi, C.A. Wurm, L. Meyer, R. Medda, G. Moneron, S. Bretschneider, C. Eggeling, S. Jakobs, S.W. Hell, New Fluorinated Rhodamines for Optical Microscopy and Nanoscopy, Chem. Eur. J. 16 (2010) 4477–4488.

[203] O. Shibata, S.K. Yamamoto, S. Lee, G. Sugihara, Mixed Monolayer Properties of Tetradecanoic Acid with *n*-Perfluorocarboxylic Acids with 10, 12, 14, 16, and 18 Carbon Atoms, J. Colloid Interface Sci. 184 (1996) 201–208.

[204] http://www.oecd.org/env/ehs/risk-assessment/2382880.pdf.

[205] H.P.H. Arp, C. Niederer, K.-U. Goss, Predicting the Partitioning Behavior of Various Highly Fluorinated Compounds, Environ. Sci. Technol. 40 (2006) 7298–7304.

[206] C. a Ng, K. Hungerbühler, Bioaccumulation of Perfluorinated Alkyl Acids: Observations and Models, Environ. Sci. Technol. 48 (2014) 4637–4648.

[207] B. Linclau, Z. Wang, G. Compain, V. Paumelle, C.Q. Fontenelle, N. Wells, A. Weymouth-Wilson, Investigating the Influence of (Deoxy)fluorination on the Lipophilicity of Non-UV-

Active Fluorinated Alkanols and Carbohydrates by a New log P Determination Method, Angew. Chemie Int. Ed. 55 (2016) 674-678.

[208] M.P. Krafft, J.G. Riess, Chemistry, physical chemistry, and uses of molecular fluorocarbon-hydrocarbon diblocks, triblocks, and related compounds-unique "apolar" components for self-assembled colloid and interface engineering, Chem. Rev. 109 (2009) 1714–1792.

[209] K. Ha, J. Kim, J.F. Rabolt, Monolayer studies of perfluorostearic acid at air/water interface, Thin Solid Films. 347 (1999) 272–277.

[210] K. Ha, W. Ahn, S. Rho, S. Suh, D. Synn, M. Stelzle, J. F. Rabolt, Characterization of orientation of perfluorostearic acid Langmuir–Blodgett multilayers by infrared spectroscopic methods, Thin Solid Films. 372 (2000) 223–229.

[211] S.E. Qaqish, S.G. Urquhart, U. Lanke, S.M.K. Brunet, M.F. Paige, Phase Separation of Palmitic Acid and Perfluorooctadecanoic Acid in Mixed Langmuir−Blodgett Monolayer Films, Langmuir. 25 (2009) 7401–7409.

[212] M. Puggelli, G. Gabrielli, G. Caminati, Langmuir-Blodgett monolayers and multilayers of stearic acid and stearyl amine, Thin Solid Films. 244 (1994) 1050–1054.

[213] N. Rontu, V. Vaida, Surface Partitioning and Stability of Pure and Mixed Films of 8-2 Fluorotelomer Alcohol at the Air-Water Interface, J. Phys. Chem. C. 111 (2007) 11612–11618.

[214] H. Meyer, Zur Theorie der Alkoholnarkose, Arch. Für Exp. Pathol. Und Pharmakologie. 42 (1899) 109–118.

[215] https://paulingblog.wordpress.com/2009/06/04/the-meyer-overton-theory-of-anesthesia/.

[216] L.J. Mullins, Some Physical Mechanisms in Narcosis., Chem. Rev. 54 (1954) 289–323.

[217] S.L. Miller, A Theory of Gaseous Anesthetics, Proc. Natl. Acad. Sci. U.S.A. 47 (1961) 1515–1524.

[218] C. Hansch, W.J. Dunn, Linear Relationships between Lipophilic Character and Biological Activity of Drugs, J. Pharm. Sci. 61 (1972) 1–19.

[219] C. Hansch, A. Vittoria, C. Silipo, P.Y. Jow, Partition coefficients and the structure-activity

relation of the anesthetic gases, J. Med. Chem. 18 (1975) 546–548.

[220] J.K. Seydel, K.J. Schaper, Quantitative structure-pharmacokinetic relationships and drug design, Pharmacol. Ther. 15 (1981) 131–182.

[221] J. Sangster, Octanol-Water Partition Coefficients of Simple Organic Compounds, J. Phys. Chem. Ref. Data. 18 (1989) 1111–1229.

[222] W. Zygmunt, J.J. Potoff, The effect of fluorination on the physical properties and the free energies of hydration of 1-alcohols, Fluid Phase Equilib. 407 (2016) 314–321.

[223] A. Hidalgo, N. Mora-Diez, Novel approach for predicting partition coefficients of linear perfluorinated compounds, Theor. Chem. Acc. 135 (2016) 18.

[224] H. Matsuda, A. Kitabatake, M. Kosuge, K. Kurihara, K. Tochigi, K. Ochi, Liquid–liquid equilibrium data for binary perfluoroalkane (C6 and C8)+n-alkane systems, Fluid Phase Equilib. 297 (2010) 187–191.

8 List of publications

[1]   M. Jbeily, T. Naolou, M. Bilal, E. Amado, J. Kressler, Enzymatically synthesized polyesters with pendent OH groups as macroinitiators for the preparation of well-defined graft copolymers by atom transfer radical polymerization, Polym. Int. 63 (2014) 894–901.

[2]   M. Jbeily, R. Schöps, J. Kressler, Synthesis of fluorinated rhodamines and application for confocal laser scanning microscopy, J. Fluor. Chem. 189 (2016) 70–78.

[3]   M. Jbeily, J. Kressler, Fluorophilicity and lipophilicity of fluorinated rhodamines determined by their partition coefficients in biphasic solvent systems, J. Fluor. Chem. 193 (2017) 67–72.

9 Acknowledgements

10 Appendix

Fig. 10.1. CLSM z-stacking images of GUVs made from the DOPC/F6H2OH 90:10 (mol %) binary mixtures. F-rhodamine dyes (0.5 mol %) are observed through the green (left) channel, the ATTO-633-DOPE dye (0.5 mol %) is observed through the red (middle) channel and the right images show the overlay of both channels.
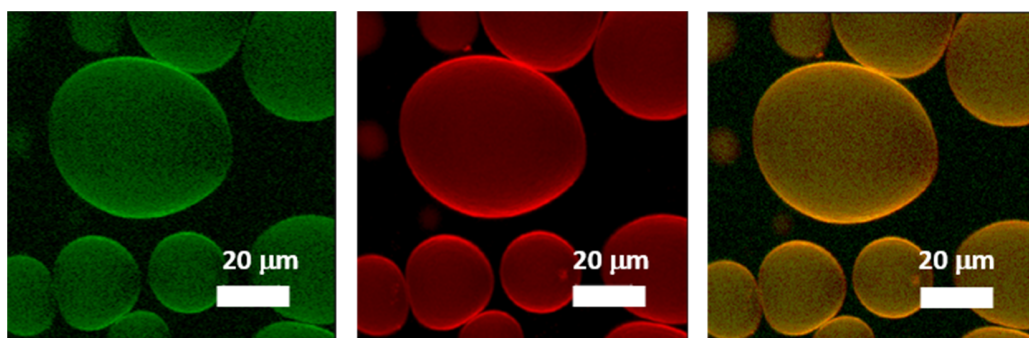
Fig. 10.2. Magnification of the DOPC/F6H2OH 80:20 (mol %) mixture of Fig. 4.1.

Abschließende Erklärung

Ich erkläre an Eides statt, dass ich die vorliegende Arbeit selbständig und ohne fremde Hilfe verfasst, andere als die von mir angegebenen Quellen und Hilfsmittel nicht benutzt und die den zitierten Werken wörtlich oder inhaltlich entnommenen Stellen als solche gekennzeichnet habe. Weiterhin versichere ich, dass die vorliegende Arbeit noch keinem anderen Promotionsausschuss vorgelegt wurde.

Mark Jbeily

Halle (Saale), 2017

CURRICULUM VITAE

Mark Jbeily

Von-Danckelmann-Platz 4
06120 Halle (Saale), Germany

E-mail: mark.jbeily@chemie.uni-halle.de

Born on 24 August 1986

Vocational and academic career

06/2012 – present	Doctoral researcher in Polymer, organic and physical chemistry at the Martin-Luther-University, Halle-Wittenberg, Germany Doctoral thesis submitted on the 15th November 2016 Defense date 21st April 2017
10/2009 – 06/2012	Master's degree in Polymer Materials Science at the Martin-Luther-University Halle-Wittenberg, Germany
09/2008 – 09/2009	Bosch service garage employee at Zalka, Lebanon
08/2008 – 09/2008	Quality assurance, Internship at Algorithm Pharmaceutical Manufacturers, Zouk Mosbeh, Lebanon
10/2004 – 09/2008	Bachelor in Chemistry at the Lebanese University, Faculty of Natural Sciences I, Beirut, Lebanon
05/2004 – 09/2009	Paramedic at the Lebanese Red Cross, emergency medical services
10/2001 – 09/2004	Baccalaureate degree in Life Sciences at Saint Joseph School, Cornet Chahwane, Lebanon

Awards

14/10/2010   DAAD-Prize for outstanding achievements during the Master's degree

Further education

27 – 31/07/2015   **GMP – course** at the Martin Luther University, Halle – Wittenberg, Germany

25 - 26/07/2013   Advanced Training Moldule in **"NMR spectroscopy for biomolecular and materials characterization"**

28 - 29/11/2012   Advanced Training Module in **"Calorimetry"**

29/09/2008   **German language course**, **A2** at the Goethe Institute, Beirut, Lebanon

Experience and knowledge

Experience/Knowledge Controlled radical polymerization (ATRP / RAFT) and Fluorescence dyes syntheses.
Chromatography (GPC and HPLC).
NMR, UV-Vis und Fluorescence spectroscopy.
CLSM und Epifluorescence microscopy.
Langmuir monolayer isotherms.
Mass spectrometry (ESI-ToF).
MS Office and Origin.

Driving license   Class B (German system)

Languages

Arabic   mother tongue
German   fluent verbally and very good in written
English   fluent verbally and in written
French   basic knowledge

Halle (Saale), 2017